

# High Precision readout of superconducting resonators

For analysis of slow noise processes

By

Jonathan Burnett



Department of Physics  
Royal Holloway, University of London

*Submitted to the University of London  
in Partial Fulfilment of the Requirements  
for the Degree of Doctor of Philosophy*

August 2013



# Declaration

I confirm that the work presented in this thesis is my own. Where information has been derived from other sources, I confirm this has been indicated in the thesis.

Jonathan Burnett

*To Kara,  
without whom, this would never have been possible*

# Acknowledgements

The success of this project would not have been possible without the assistance and understanding of many people. Initial recognition should be given to Phil for his encouragement and belief in me to undertake a PhD. The joint project between the National Physical Laboratory and The Royal Holloway University was only made possible because of the discussions between Phil and Sasha. As the project evolved a majority of my time was spent at NPL, and I am thankful of the unselfish attitude displayed by Phil. It has been an absolute pleasure to be Tobias' first PhD student. His enthusiasm to entertain, discuss and guide all scientific discussions, whilst calmly pointing out potential flaws was invaluable and definitely made my labour easier. Sasha provided any and all additional knowledge along with concise explanations when those with Tobias did not suffice. These are inestimable and his story telling was a memorable extra. Finally, I had the privilege to work with and share an office with Mark. I am sure he does not fully appreciate how useful, well informed and entertaining he was. Certainly, without his input the many elements of this thesis would not be so thoroughly understood.

Additionally I am thankful for all input, both great and small, from; Ling, John, Jon, Vladimir, Rais, Olga and especially Steve. I must also mention Sergey for providing me with the excellent opportunity for a secondment at Chalmers. It enabled me the pleasure to work with Sebastian who made my time there significantly more productive and enjoyable.

Otherwise there have been some excellent fellow students; Cat, Joseph, Ravish, Hume, Connor, Viktoria, Tom, Ilana and Vishal, who always provided much needed laughter throughout the last 3 years. A large quantity of this thesis has been greatly improved upon due to Ilanas enthusiasm and questioning. It ensured I understood all the content.

Outside of work, I consider myself fortunate to have a supportive and patient network of friends and family. Regardless of frequently putting work first, they remained understanding throughout. Special thanks go out to James, Rik, Sam, Chris and my sister, Kayleigh. This thesis would not be what it is without tremendous support from Pauline and Kara. Finally, I am fortunate to have had a lifetime of love, support, belief and encouragement from my mum.

# Abstract

10 years ago superconducting resonators emerged with two potential applications, firstly kinetic inductance detectors were proposed [1] and secondly the strong coupling of a resonator to a qubit was realised [2]. As such, the field of superconducting quantum circuits is beginning to enter maturity and has become competitive with alternative approaches to quantum information processing [3] and photon detection [4]. However, there remains much room for further improvement and some problems persist still. Prevalent among these problems is a high level of environmental noise interfering with the device. This environment can be parametrised as a bath of two level fluctuators (TLFs): an uncontrolled intrinsic two level system which couples to the superconducting quantum circuit. These can produce the ubiquitous  $1/f$  noise and are a dominant source of decoherence.

In this thesis, microwave resonators are interrogated using a novel high-precision frequency readout technique. This technique is based upon Pound locking and is implemented to examine the effects of two level fluctuators. The Method uses feedback to track deviations in the centre frequency of a microwave resonator. Sensitivity to Hz-level fluctuations allows the technique to trace ultra low dielectric loss tangents. Hence the approach is suitable for accessing even the samples with a very low density of two level fluctuators. Additionally a feedback mechanism allows for slow noise processes to be studied with exceptional statistical confidence.

This thesis outlines the theory and development of the Pound loop. This is characterized and improved until capable of resolving Hz-level deviations and operating towards single photon energies within the resonator. This allows the  $1/f$  noise of a resonator to be studied under varying microwave drive and temperature. Ultimately we show that a new design of epitaxially grown superconductor is able to realize an ultra low dielectric loss tangent, and a low noise level, probably significantly below that measured by any other system. Which allows the temperature dependence of  $1/f$  noise in superconducting resonators to be examined. This result provides important new guidance to methods that might eradicate the TLF problem from superconducting quantum circuits.

# Contents

1	Introduction . . . . .	15
1.1	State of the field . . . . .	18
1.2	The dielectric loss problem . . . . .	19
1.3	Project aims . . . . .	20
2	Solid state theory . . . . .	21
2.1	Phenomena of Superconductivity . . . . .	21
2.2	Two fluid model . . . . .	23
2.3	Two level fluctuators . . . . .	24
3	The theory of superconducting resonators . . . . .	29
3.1	Derivation of the quality factor and Mattis-Bardeen effects . . . . .	29
3.2	Derivation of scattering parameters . . . . .	31
4	Measurement theory . . . . .	37
4.1	Phase sensitive detection . . . . .	37
4.2	Frequency sensitive detection . . . . .	40
4.3	Pound theory . . . . .	43
4.4	The effects of asymmetric resonances . . . . .	47
4.5	Fluctuations . . . . .	49
4.6	Barkhausen relation . . . . .	56
4.7	The Leeson frequency and its effects . . . . .	58
5	Literature review . . . . .	62
5.1	Studies of noise in other systems . . . . .	65
5.2	Studies of noise in Superconducting resonators . . . . .	66
5.3	Studies of noise in hybrid systems . . . . .	68
5.4	Summary . . . . .	70
6	Measurement setup . . . . .	74
6.1	Microwave setup . . . . .	75
6.2	Cryogenic setup . . . . .	79

7	Characterizing the loop . . . . .	81
7.1	The resonator . . . . .	81
7.2	Jitter studies and determining the system noise floor . . . . .	81
7.3	Optimizing the loop . . . . .	84
8	Identifying noise processes in superconducting resonators . . . . .	88
8.1	Description of the samples . . . . .	88
8.2	Loss and Noise analysis of superconducting resonators . . . . .	92
8.3	Discussion . . . . .	98
9	Noise measurements of Superconducting resonators in varying temperature	100
9.1	Description of the samples . . . . .	100
9.2	Loss and Noise analysis of superconducting fractal resonators . . . . .	101
9.3	Discussion . . . . .	105
10	Examining the $1/T$ dependence of $1/f$ noise in superconducting resonators .	108
10.1	Description of the samples . . . . .	108
10.2	Extracting loss tangents from epitaxially grown resonators with ultra low dielectric loss . . . . .	109
10.3	Mapping the temperature dependence of $1/f$ noise in epitaxial super- conducting resonators . . . . .	111
10.4	Discussion . . . . .	115
11	Conclusions . . . . .	118
11.1	The Pound loop . . . . .	118
11.2	Noise studies in superconducting resonators . . . . .	119
11.3	Loose ends . . . . .	120
11.4	Outlook . . . . .	124
	Appendix A: Fabrication . . . . .	126
	Appendix B: Research output . . . . .	129
	Bibliography . . . . .	131

# List of Figures

2.1	Circuit model of a superconductor . . . . .	25
2.2	Simulation of general frequency shift due to TLFs . . . . .	27
2.3	Simulation of the general change in $Q_i$ due to TLFs . . . . .	28
3.1	Schematic of a parallel LC circuit . . . . .	30
3.2	Simulation of how quality factor scales with normalised temperature using Mattis-Bardeen theory. . . . .	32
3.3	Simulation of the magnitude and phase response of a resonator . . . . .	36
4.1	Schematic of a Simple homodyne setup . . . . .	38
4.2	Simulation of general phase noise shape . . . . .	39
4.3	Schematic of a typical homodyne setup . . . . .	41
4.4	Schematic of a simple Pound setup . . . . .	42
4.5	Plot of the Pound error signal . . . . .	46
4.6	Simulations of an increasingly asymmetric resonance . . . . .	48
4.7	Simulation of an increasingly asymmetric Pound error signal . . . . .	48
4.8	A plot showing a real time series of data . . . . .	49
4.9	A plot comparing the phase spectrum, frequency spectrum and Allan variance	51
4.10	Simulation of how the standard variance scaling with sample size for different noise types . . . . .	55
4.11	Plot of the Barkhausen relation . . . . .	57
5.1	Plot of the phase noise, fractional frequency noise and Allan deviation of a $b_0$ limited amplifier under varying microwave drive . . . . .	71
6.1	Schematic of the Real Pound setup . . . . .	74
6.2	Photo of the dilution refrigerator . . . . .	75
6.3	Photo of the dilution refrigerator tail with aluminium sample box . . . . .	76
6.4	Photo of the microwave setup . . . . .	77
6.5	Photo of dilution refrigerator tail with aluminium can . . . . .	78
6.6	Schematic of the cryogenic setup . . . . .	80

7.1	Plot of the magnitude response of the dielectric resonator at 100 mK . . . .	82
7.2	Plot of the stability analysis of the dielectric resonator . . . . .	83
7.3	Plot of the power dependence of the $h_{-1}$ flicker noise floor . . . . .	84
7.4	Plot of the diode sensitivity . . . . .	85
7.5	Plot of the YIG transmission characteristic . . . . .	86
8.1	A photo of a bonded sample . . . . .	89
8.2	A photo of a lumped element resonator . . . . .	90
8.3	Magnitude response of the 6.98 GHz Nb on Sapphire resonator . . . . .	91
8.4	Magnitude response of the 5.08 GHz ALD $Al_2O_3$ Nb on Sapphire resonator	92
8.5	Loss tangent measurement of the 6.98 GHz Nb on Sapphire resonator . . .	93
8.6	Loss tangent measurement of the 5.08 GHz ALD $Al_2O_3$ Nb on Sapphire resonator . . . . .	94
8.7	Chart of frequency dependence of $F \tan \delta$ across numerous samples . . . . .	95
8.8	Allan analysis of noise processes in a superconducting resonator . . . . .	96
8.9	Spectral analysis of noise processes in a superconducting resonator . . . . .	97
9.1	Magnitude response of the 7.06 GHz Nb on Sapphire fractal resonator . . .	101
9.2	Loss tangent measurement of the 7.06 GHz Nb on Sapphire fractal resonator	102
9.3	Allan analysis of the 7.06 GHz Nb on Sapphire fractal resonator with varying microwave drive . . . . .	103
9.4	Behaviour of spectral noise at 0.1 Hz for the 7.06 GHz Nb on Sapphire fractal resonator under varying microwave drive . . . . .	104
9.5	Behaviour of spectral noise at 0.1 Hz for the 7.06 GHz Nb on Sapphire fractal resonator at various temperatures . . . . .	105
10.1	Magnitude response of the 5.55 GHz and 6.68 GHz epi-Nb+Pt on Sapphire LE resonators . . . . .	109
10.2	Loss tangent measurement of the 5.55 GHz epi-Nb+Pt on Sapphire LE resonator . . . . .	110
10.3	Loss tangent measurement of the 6.68 GHz epi-Nb+Pt on Sapphire LE resonator . . . . .	111
10.4	Spectrum of frequency fluctuations for the 6.68 GHz epi-Nb+Pt resonator .	112

10.5 Spectrum of frequency fluctuations at 0.1 Hz in varying microwave drives for the 6.68 GHz epi-Nb+Pt resonator . . . . .	114
10.6 Spectrum of frequency fluctuations at 0.1 Hz vs. temperature for the 5.55 GHz and 6.68 GHz epi-Nb+Pt resonators . . . . .	115
11.1 Response of resonator to strong irradiation at 635 nm . . . . .	121
11.2 Response of resonator to varying irradiation at 635 nm . . . . .	122
11.3 Response of resonator coupled to a CPB . . . . .	123
0.1 Comparison of samples fabricated with and without additional bead removal steps . . . . .	127
0.2 Comparison of samples fabricated with and without additional resist strip steps . . . . .	128

# List of Tables

1	Table of important symbol definitions . . . . .	13
2	Table of abbreviations used within thesis . . . . .	14
3	Table of resonator parameters . . . . .	14
4	Table of power law noise processes . . . . .	53
5	Table summarising noise measurements on superconducting devices . . . . .	66
6	Table summarising frequency stability of various frequency standards . . . . .	69
7	Table summarising noise measurements on superconducting resonators before the start of this thesis . . . . .	73

Table 1: Table of important symbol definitions

Symbol	Definition
$\alpha$	kinetic inductance ratio, or coefficient of power law noise process
$\Delta(T)$	Superconducting gap energy at temperature $T$
$\delta_i$	Intrinsic dielectric loss tangent
$E$	Electric field
$E_c$	TLF saturation field
$\epsilon$	Permittivity
$F$	Filling factor
$f$	Fourier frequency
$f_L$	Leeson frequency
$g$	Coupling parameter
$h_{-1}$	Flicker frequency magnitude
$i$	Current
$J_i(\beta)$	Bessel function of $i$ th order with modulation index $\beta$
$P_{app}$	Applied microwave drive
$P_c$	TLF saturation microwave drive
$\nu$	Drive frequency
$\nu_0$	Centre frequency of resonator, resonant frequency
$\langle n \rangle$	Average number of photons within a resonator
$\mu$	TLF distribution parameter
$Q_c$	Quality factor due to coupling
$Q_i$	Intrinsic quality factor
$\sigma_y$	Allan deviation, usually implied to be overlapping, often fractional
$\sigma_y^2$	Allan variance, usually implied to be overlapping, often fractional
$S_y$	Spectrum of frequency fluctuations, often fractional
$S_Q$	Spectrum of charge fluctuations
$S_\theta$	Spectrum of phase fluctuations
$S_\phi$	Spectrum of flux fluctuations
$T_c$	Superconducting transition temperature
$T_1$	Longitudinal relaxation time in a TLS
$T_2$	De-phasing time in a TLS
$\theta$	Phase
$U$	Energy, usually in terms of a potential
$V$	Voltage
$y$	Normalised fractional frequency, defined as $\nu - \nu_0/\nu_0$
$\Gamma_1$	Longitudinal relaxation rate for a TLS, $T_1 = 1/\Gamma_1$
$\Gamma_2$	De-phasing rate for a TLS, $T_2 = 1/\Gamma_2$
$\Omega$	Frequency of Rabi oscillations in a TLS
$\omega$	Drive angular frequency, $\omega = 2\pi f$ , sometimes called $\omega_c$
$\omega_m$	Phase modulation frequency in Pound setup, typically 1 MHz
$W_s$	Energy stored within a resonator
$Z$	Impedance
$Z_0$	Characteristic impedance, usually 50 $\Omega$

Table 2: Table of abbreviations used within the thesis

Abbreviation	Definition
CPB	Cooper Pair Box
CPW	Coplanar Waveguide
HEMT	High Electron Mobility Transistor
HPF	High Pass Filter
KID	Kinetic inductance detector
MB	Mattis-Bardeen, usually implying an element derived from the theory
$\mu$ W	Microwave
PID	Proportional-Integral-Derivative controller
QIP	Quantum Information Processing
SET	Single Electron Transistor
SQUID	Superconducting QUantum Interference Device
TLF	Two Level Fluctuator
TLS	Two Level System
VCO	Voltage Controlled Oscillator
VNA	Vector Network Analyzer
YIG	Yttrium Iron Garnet, usually meaning a narrowband tunable filter

Table 3: Table of resonator parameters

Resonator	Geometry	Frequency (GHz)	$Q_i \times 10^4$	$g$	$F \tan \delta$ $\times 10^{-6}$
Sputtered Nb	LE	5.08	23.1	21.5 - 5.3j	26
Sputtered Nb	LE	6.98	44.3	18.5 - 3.6j	2.0
Sputtered Nb	Fractal	7.06	7.3	1.6 + 0.6j	12
Epitaxial Nb	LE	5.4	5.8	2.3 + 1.3j	1.8
Epitaxial Nb	LE	6.69	7.6	0.9 + 0.5j	1.7
Epitaxial Nb+Pt	LE	5.55	24.1	6.6 + 0.2j	1.4
Epitaxial Nb+Pt	LE	6.68	34.9	13.1 - 2.1j	1.1

# Chapter 1: Introduction

At the start of this project, the field of superconductivity was approaching its 100th birthday. However, despite this age, superconductivity is far from widespread in its uses. Outside of research, there are perhaps only two well developed applications: superconducting magnets as used in MRI scanners, and magnetometers based on Superconducting QUantum Interference Devices (SQUIDs). By comparison, the 60 year old field of semiconductors is considerably more abundant, so that it can be difficult not to be near some device based upon semiconductors. A large reason for this is simply that semiconductors have many useful properties at room temperature. This is unlike superconductivity, which is a low temperature phenomenon. Traditionally, liquid helium is required to reach these low temperatures. This is prohibitive due to the large cost and high level of knowledge required to operate cryogenic systems. In recent years, so called *dry* (meaning no liquid helium) cryogenic systems have come a long way. While still prohibitively expensive, the ability to reach low temperatures at the push of a button greatly relaxes the knowledge requirement. It is possible that easier access to cryogenic temperatures may help superconductivity realise more useful applications.

A superconductor is something that possesses zero DC resistance when at temperatures below some transition temperature  $T_c$ . The superconducting state is described by a macroscopic quantum wave-function, meaning a superconductor behaves as a bulk quantum object. Detectors are therefore an obvious application, where the superconductor is very sensitive to some perturbation of the superconducting state. Another property of superconductivity is the ability to weakly couple two superconductors via the Josephson effect. This results in a low dissipation system which is very sensitive to fluctuations in either superconductor. Coupling this with the perfect diamagnetism from magnetic flux quantisation, allows the SQUID to be realised.

At high frequencies a superconductor does not exhibit zero resistance. This can be understood using the two fluid model of the superconductor, where the charge carriers are modelled as two inter mixed populations consisting of Cooper pairs and quasiparticles. Any

current is forced through each of these populations and therefore even in the superconducting state some current can be carried by the quasiparticles, which can create dissipation. However, the dissipation is low enough that ultra high quality factor resonators can be realised. This high quality factor is exploited by kinetic inductance detectors to increase their sensitivity<sup>1</sup>. The low dissipation means that when a superconductor is excited by a high frequency field, the carriers are able to store the energy without loss. This stored energy can then be recovered when reversing the field, which is not usually possible in normal metals. Since the energy can be recovered in phase (like an inductor) it is termed as an inductance. This additional inductance allows superconducting microwave circuits to be made smaller than their non superconducting counterparts and is the mechanism for kinetic inductance detectors. Here circuits can be made sensitive to excitations in the superconducting state. These excitations cause dissipation in the device, changing the kinetic inductance and therefore producing a frequency shift in the circuit.

Another microwave device, is the solid state qubit. Here a quantum state is realised by creating an asymmetric potential well from a Josephson junction<sup>2</sup>. Operations can be performed on this state to realise a quantum bit (qubit). Microwave devices are therefore an attractive application of superconductors. However, despite high expectations, both of these applications suffer from degraded performance. A higher than expected level of noise exists, resulting in reduced sensitivity and high levels of decoherence<sup>3</sup>.

It is proposed that the noise can be parametrised by the presence of a bath of two level fluctuators (TLFs) [5]. In the context of superconducting circuits, a two level fluctuator (TLF) is described by an asymmetric potential well. Transitions between the states can occur by absorption of a microwave photon or by thermally excited tunnelling, which saturates by 1 K. The TLFs exhibit a broad energy spectrum for the asymmetry in the potential, resulting in a distribution that is nearly uniform in frequency. Experiments with

---

<sup>1</sup>The kinetic inductance is associated with the kinetic energy absorbed by a charge carrier from a high frequency field. It is very high for a few excess quasiparticles (electrons) within the sea of Cooper pairs. Therefore kinetic inductance detectors operate by observing the frequency shift associated with the breaking of Cooper pairs.

<sup>2</sup>A Josephson junction is a weak link between two superconductors. Generally this is realized as an oxide barrier separating the superconductors.

<sup>3</sup>Decoherence relates to the lifetime of the quantum state. A high level of decoherence means that the state is short lived. The parasitic interference of TLFs is proposed as the cause of this short lifetime.

small Josephson junctions can view avoided crossings due to interactions with individual TLFs [6], in contrast superconducting resonators usually couple to a large ensemble due to their much larger size.

A microwave photon can interact with the TLFs as well as the qubit or resonator. For qubits, this means that a quantum state can be influenced by a photon released by a TLF relaxing. It also means the qubit sees a different environment depending on whether the TLF is excited or not. This results in the qubit Larmor frequency being dependent on the environment. In superconducting resonators a TLF produces two effects. At low microwave drive a photon interacts with the TLF creating a path for energy loss, lowering the resonators internal quality factor ( $Q_i$ ). Additionally each state of the TLF corresponds to a different relative permittivity, resulting in a frequency shift as the ratio of thermally excited TLFs varies with temperature between 50 mK–1 K. This means that like the qubit, the resonator is sensitive to the environment and whether TLFs are excited or not.

This thesis will give an overview of a measurement technique new to this field, based upon a Pound based frequency locked loop, to study the frequency jitter in superconducting resonators. Chapter 2 follows conventional solid state theory before introducing TLFs. Then Chapter 3 describes the models for superconducting resonators and their transmission parameters, showing the effects of TLFs and the Mattis-Bardeen theory. Chapter 4 covers details of oscillator stability, the Barkhausen condition, the Leeson effect and the theory for a Pound frequency locked loop. It also details the statistical methods for analysing frequency jitter, focusing on the use of Allan based statistics which feature heavily in later measurements. Chapter 5 contains the Literature review before Chapter 6 covers the measurement setup. Lastly, experimental sections begin with measurements of the systematic noise contributions in Chapter 7. Following this are three further chapters on measurements of superconducting resonators. The first of these examines the ability of the Pound method to study noise in superconducting resonators. It finds that not only do superconducting resonators exhibit flicker noise, but crucially this is in excess to the measured system noise floor. The flicker noise is shown to be temperature and power dependent, an effect which is studied further in Chapter 9. Here another resonator geometry is measured, finding the flicker noise increases with both decreasing temperature and power. Although

consistent with previous results, the large dielectric loss tangent makes temperature instability problematic to the measurements. To solve this an epitaxially grown sample with a novel conducting capping layer is measured in Chapter 10. This sample exhibits such low dielectric loss that the temperature dependence of the flicker noise is fully mapped out. The final measurement finds strong evidence that the TLF picture is incomplete and needs to consider interactions. Finally, the thesis ends with Chapter 11 which covers the conclusions and suggestions for future measurements.

## 1.1 State of the field

Research into superconducting resonators has become increasingly popular over the past decade. Initial applications relied on using the kinetic inductance to produce millimetre wave detectors [1], the next generation of which are likely to surpass the performance of bolometers currently in use [7]. Kinetic inductance detectors consist of a resonator coupled to the absorber, which is usually another superconductor. Photons incident on the absorber create quasiparticles, leading to a change in the kinetic inductance and therefore the resonator's centre frequency. These detectors are interrogated in the many photon regime with circulating powers in excess of  $\approx -40$  dBm [8]; where, high power in the resonator can allow for very large quality factors, typically  $10^6$  but recently in excess of  $10^7$  [9].

The second major use of superconducting resonators is in quantum information processing (QIP). Here, resonators are coupled to qubits for readout of the qubit state [2], to act as a memory bus coupling multiple qubits [10] or create quantum limited amplifiers [11], [12]. For QIP applications, the resonator power approaches energies where only one photon is circulating in the resonator [13](a low power is required to correctly manipulate the qubit). At low powers, the  $Q_i$  of the resonator is found to decrease [14], and the mechanism behind this is also a possible cause of decoherence in the qubit.

Changes to the  $Q_i$  with decreasing power cannot be explained by Mattis-Bardeen theory<sup>4</sup>; instead, a description of the resonator coupling to a bath of two level fluctuators

---

<sup>4</sup>Mattis-Bardeen theory takes the two fluid model of superconductivity and extends the discussion of how the conductivity fractions vary with temperature. Importantly this produces a temperature dependent quality factor and frequency shift in superconducting resonators.

(TLFs) is required [15]. Additional measurements have also shown the centre frequency to be temperature dependent after Mattis-Bardeen mechanisms have saturated [16–19], this effect can also be described by the resonator coupling to a bath of two level fluctuators. These TLFs absorb and emit resonant photons. This produces both a source of loss and a potential source of decoherence.

The microscopic origin of TLFs is not currently known. Additionally measurements are yet to agree with theory for the noise processes produced by a bath of two level fluctuators [7]. Furthermore measurements are yet to agree on the exact nature of these TLFs, such as whether they act independently of each other or are in fact interacting.

## 1.2 The dielectric loss problem

Dielectric loss is a measure of the dissipation of electromagnetic energy within a dielectric material. It is modelled by a phasor in the complex plane which represents the resistive and reactive components. The level of loss is described by either the loss angle  $\delta$  or the loss tangent  $\tan \delta$ . Dielectric loss is usually considered arising from a bath of TLFs [20–23]. Such TLFs are a candidate for producing the ubiquitous  $1/f$  noise [24] and are expected to produce de-phasing in Josephson qubits [25] [26]. Furthermore, superconducting circuits are also affected by dielectric loss. The dielectric loss tangent,  $\tan \delta$ , directly relates to two parameters. Firstly the intrinsic loss tangent provides a limitation on the qubit  $T_1$  [27], this is due to the common approach of using a Josephson junction shunted by a thin capacitor [28]. Where dielectric loss within the Josephson junction leads to

$$T_1 < \frac{1}{\omega_{10} \tan \delta} \quad (1.1)$$

where  $\omega_{10}$  is the qubit transition frequency,  $\tan \delta$  is the dielectric loss tangent and  $T_1$  is the energy decay time of the qubit. Hence a high dielectric loss tangent leads to a limitation of the maximum possible  $T_1$ . Furthermore the loss tangent limits the maximum possible intrinsic quality factor by  $1/Q_{max} = \tan \delta$ .

A superconducting resonator’s sensitivity to temperature fluctuations is determined by the dielectric loss tangent. Where a modest temperature instability of  $\sim 100$  mK  $\pm 5$  mK

leads to a  $\Delta\nu$  in the kHz for a GHz resonator with typical loss tangent values in the mid- $10^{-5}$  level (where typical resonators have  $F \tan \delta \approx 10^{-4} - 10^{-6}$ ). Such frequency shifts give the appearance of low frequency noise.

### 1.3 Project aims

The aim of this project is to investigate the effects of TLFs - a dominant decoherence mechanism in superconducting circuits. These TLFs are studied using superconducting resonators, which are sensitive probes to fluctuations in their electromagnetic environment. The project aimed to:

1. Develop novel measurement techniques to enable the characterisation of ultra low dielectric loss,
2. Develop a novel measurement technique to study jitter and noise of superconducting resonators,
3. Examine the role of TLFs in the noise mechanisms by investigating noise while tuning TLF parameters.

The measurement technique is based upon an adapted Pound frequency locked loop and is novel to this field. This technique which was first used for NMR, but has been adapted for the stabilisation of lasers [29]. This thesis examines the Pound method theoretically and explores its suitability to measure properties of superconducting resonators. These include the measurement of ultra-low dielectric loss and the study of intrinsic jitter within the resonator.

# Chapter 2: Solid state theory

The theoretical part of this thesis is split into several chapters. The first of which is this chapter, which provides an overview of the relevant solid state theory. After this, the circuit models for superconducting resonators are covered in Chapter 3. Finally Chapter 4 details the measurement and analysis details which are used later in the thesis.

## 2.1 Phenomena of Superconductivity

A normal metal consists of many electrons, often in excess of  $10^{28}\text{m}^{-3}$ . In the simplest picture the electrons are non interacting and only constrained by the Pauli exclusion principle [30]. This gas of fermions produces conduction properties described by the Drude-Sommerfeld model. Under closer examination, the electron density is high enough to produce interactions between the electrons, where electrons are pushing each other away due to the Coulomb force. The high electron density also leads to screening of these interactions, effectively reducing them to distances comparable to the inter-atomic spacing. Any motion of an electron will also cause the screened Coulomb interaction to move, leading to other electrons being perturbed by this screened Coulomb interaction. As such, the electrons can no longer be considered independent within a Fermi gas, instead they must be considered as electron-like quasiparticles within a Fermi liquid.

These quasiparticles forming a Fermi liquid are interdependent and also have a finite lifetime. All conduction properties can now be understood in terms of these quasiparticles acting as charge carriers. Within a normal metal, these charge carriers are called Landau quasiparticles. Furthermore elastic and inelastic interactions leads to interesting effects within metallic solids with strong electron lattice coupling, which combined with the Coulomb interaction can lead to an attractive interaction between quasiparticles (known as BCS theory). The lattice can be distorted by the motion of a quasiparticle. The now distorted lattice appears as a positively charged region, capable of attracting a second quasiparticle. Therefore, producing an effective attraction between two quasiparticles that is mediated by a phonon. This attraction has already been shown to form a bound state with a binding energy  $\Delta$  by Cooper [31]. It was further shown that the quasiparticle pairs

must exist at opposite sides of the Fermi surface. Then, below a sufficiently low temperature, these quasiparticles form a Cooper pair and condense into a macroscopic quantum state. That is, all Cooper pairs can be described by one superconducting wave function. The length scale over which this wavefunction decays, or equivalently, the maximum separation of the Cooper pair is given by the coherence length,  $\xi(0) = \hbar v_F / \pi \Delta(0)$  where  $v_F$  is the Fermi velocity and  $\Delta(0)$  is the binding energy at zero temperature.

Excitations from this macroscopic quantum state are called Bogoliubov quasiparticles [32]. These excitations are described by an energy,  $U = \sqrt{\eta^2 + \Delta^2}$  with  $\eta$  being the energy of a single particle in the normal state (a Landau quasiparticle) relative to the Fermi energy. For  $\eta > 0$  the Bogoliubov particle is electron-like and for  $\eta < 0$  it is hole-like. Both are equally favourable unless there exists a charge imbalance.

From BCS theory, the critical temperature in weakly coupled superconductors is described by  $T_c = \frac{1.14 \hbar \omega_D}{k_B} e^{-1/N(0)U_{ep}}$ . Where  $U_{ep}$  is the electron phonon coupling potential and  $\omega_D$  is the Debye frequency. BCS theory also predicts that the superconducting energy gap is related to the critical temperature by  $\Delta = 3.52 k_B T_c \sqrt{1 - (T/T_c)}$ . This highlights that at temperatures above  $T_c$  the energy gap drops to zero, destroying the superconducting state. From the temperature dependence of the energy gap, it follows that the density of quasiparticle excitations is also temperature dependent, this is described by

$$N_{qp} = 2N(0) \int_{\Delta}^{\infty} N(U) f(U) dU \sim 2N(0) \sqrt{2\pi k_B T} \Delta e^{-\Delta/k_B T} \quad (2.1)$$

The final term is true for  $k_B T \ll \Delta$ , which allows the Fermi-Dirac distribution to be replaced by a Maxwell-Boltzmann distribution.

This BCS picture of superconductivity produced both the qualitative and quantitative description of superconductivity that had been missing in the near half century since its discovery. The theory explained the pairing mechanism, its temperature dependence, and described its charge carriers. It provided a framework to describe the vanishing DC resistance, expulsion of magnetic fields, exponentially decreasing heat capacity and infrared properties of superconductivity. Interestingly, the theory makes only a few changes to the Drude-Sommerfeld model; including an effective attractive potential and describing the

screened Coulomb repulsion by just the quantity  $\mu^*$ . From this, the superconducting state of any s-wave superconductor can be described by one wavefunction with a macroscopic phase and energy gap  $\Delta$ .

## 2.2 Two fluid model

When the temperature of a superconductor is reduced through the superconducting transition temperature, the population of charge carriers can be modelled as consisting of two parts. One part consists of normal electrons (quasiparticles) described by the density  $n_n$ . The other part consists of Cooper pairs with a density  $n_s$ . These two densities allow the conductivity of the superconductor to be described by a two-fluid model. This model takes into account that the current within a superconductor can travel by one of two paths, either by  $n_s$  or  $n_n$ . Within this two fluid model, the conduction densities are described by the following laws.

$$n_t = n_s + n_n \quad (2.2)$$

$$n_s = n_t \left( 1 - \left( \frac{T}{T_c} \right)^4 \right) \quad (2.3)$$

This shows the two densities sum to the total electron density of the metal at all temperatures. As the temperature is decreased below  $T_c$  the Cooper pair density increases, eventually becoming equal to the total electron density at  $T = 0$  K. From these densities, the quasiparticle contribution to the conductivity can be denoted as  $\sigma_n$ , while the conductivity due to  $n_s$  is given by  $\sigma_s$ , considering the complex conductivity expressed using the Drude model.

$$\sigma = \frac{n_t e^2 \tau_s}{m(1 + i\omega\tau_s)} = \frac{n_t e^2 \tau_s}{m(1 + \omega^2 \tau_s^2)} - i \frac{n_t e^2 \omega \tau_s^2}{m(1 + \omega^2 \tau_s^2)} \quad (2.4)$$

This is now of the form  $\sigma = \sigma^1 + i\sigma^2$  and a circuit model of a superconductor can be constructed using this equation to demonstrate the routes available for a current when flowing through a superconductor, as shown in figure 2.1. The complex Drude model considers a scattering time  $\tau_s$  which in a normal metal is approximately  $10^{-14}$ s. However, a superconductor experiences no scattering, hence  $\tau_s$  can be taken as very large. When

this happens, the complex Drude model can be rewritten to give

$$\sigma \sim \frac{n_t e^2}{m} \left( \frac{1}{\omega^2 \tau_s} - j \frac{1}{\omega} \right) \quad (2.5)$$

it follows that at low frequencies the real term will dominate the conductivity, this leads to the characteristic zero resistance which gives superconductivity its name. At higher frequencies, the imaginary term dominates. This change in behaviour typically occurs at microwave frequencies, where  $\omega^2 \tau_s \gg 1$ . Phenomenologically the process can be understood by considering charged particles in a high frequency field. A Cooper pair can absorb the energy from a high frequency field, but since they cannot scatter, this energy is stored within the condensate and can be extracted again, so the effect being likened to an inductance. A normal quasiparticle can scatter, which creates a dissipative path at high frequencies. The effect is termed the kinetic inductance and allows superconducting circuits to exhibit a larger inductance than is possible from their geometry alone (this can also be realised in normal metals but at much higher frequencies). The kinetic inductance at zero temperature can be estimated using Mattis-Bardeen theory to give  $L_K = 0.18 \frac{\hbar R_n}{k_B T_c}$ , where  $R_n$  is the normal state resistance. Additionally, these effects are temperature dependent due to the carrier density terms  $n_s$  and  $n_n$ . Therefore, it follows that as the temperature is increased towards  $T_c$  a larger proportion of the current is shunted into the resistive normal path. This produces increasing losses when the temperature or frequency is increased.

### 2.3 Two level fluctuators

This section overviews the theory relating to two level fluctuators. In other work, these are often called two level systems, but here the word fluctuator is used to express that the system is not readily controlled, by comparison a qubit is considered as two level system since the probability of either state being occupied can be directly controlled.

The study of two level fluctuators began with measurements of amorphous solids at low temperatures [20] [21], where the thermal, acoustic, and dielectric properties were found to be very different to that of crystalline solids. A model which successfully describes

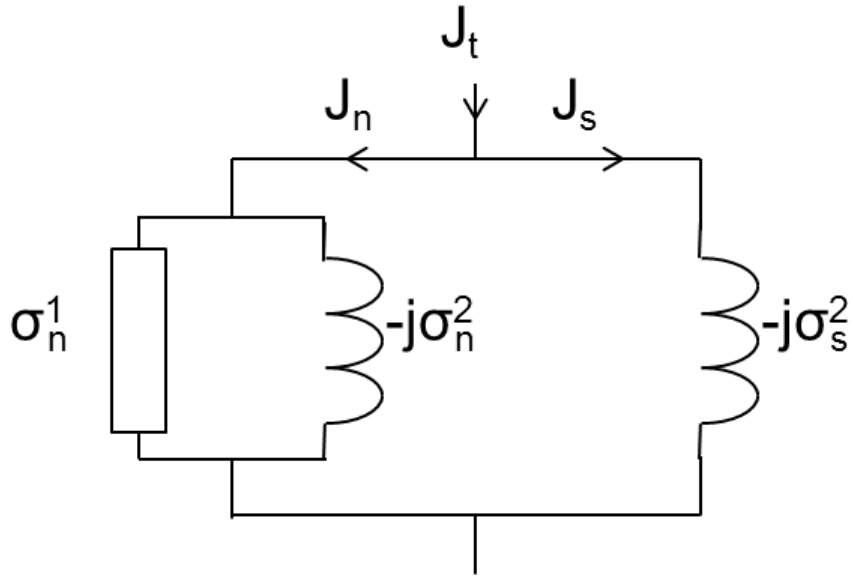


Figure 2.1: Circuit model of a superconductor showing the different routes current can take. The impedance of each route changes with frequency; a superconductor has different DC and AC properties, which vary with the relative carrier densities  $n_s$  and  $n_n$ .

all the key behaviour was independently introduced by Phillips [22] and Anderson [33]. This model explains the temperature dependent behaviour by the existence of a broad spectrum of tunnelling states. For this thesis, changes to the dielectric constant are most important, and the model suggests a change to the dielectric constant based upon the population of the tunnelling states. A rigorous derivation of the model can be found in the thesis by Gao [18], the review by Phillips [23] or the book “Low Temperature Physics” by Enss and Hunklinger [34]. Here, I will only draw attention to the specific details of the model required for either conceptual understanding or explaining results shown later in this thesis.

The two level fluctuator is modelled as a particle in an asymmetric double well potential, where thermally excited tunnelling allows for transitions between the states of either well. Alternatively the model allows for transitions to occur by resonant absorption of microwave photons. Each state corresponds to a different dielectric constant. As such transitions between states produce a change in the dielectric constant, this is despite the expectation that the dielectric constant would be unchanging at such low temperature [35] [36]. Experimentally superconducting resonators are found to exhibit a temperature dependent

centre frequency and a microwave drive dependent  $Q_i$ . Where the frequency decreases with decreasing temperature and the quality factor decreases with decreasing microwave drive. Both effects can be parametrised by the presence of a bath of two level fluctuators coupling to the resonator.

TLF effects have been found in a variety of substrates including r-cut sapphire [37], c-cut sapphire [38], MgO [14], SiN [39], hydrogen passivated Si [40], wet and dry SiO<sub>2</sub>/Si [41] and bare Si [42]. Additionally comparisons between surface oxides and deposited dielectrics have been made using SiO<sub>x</sub> [43] and AlO<sub>x</sub> [40] [44]. The abundance of systems exhibiting TLF like behaviour has led to suggested microscopic origins; paramagnetic impurities such as chromium in sapphire, and dangling bonds which have been found in oxidised silicon surfaces [19]. Changes in dielectric constant ( $(\epsilon(T) - \epsilon(T_0))/\epsilon(T)$ ) are parametrised as [23]

$$\frac{\epsilon(T) - \epsilon(T_0)}{\epsilon(T)} = -\frac{2nd^2}{3\epsilon} \left( \ln \frac{T}{T_0} - [g(T, \omega) - g(T_0, \omega)] \right) \quad (2.6)$$

Where  $g(T, \omega) = \text{Re}\Psi(1/2 + \hbar\omega/2\pi ik_B T)$ ,  $T_0$  is a reference temperature,  $\Psi$  is the complex digamma function and is only significant when  $k_B T \leq \hbar\omega/2$  and  $nd^2$  relates to the density of fluctuators and their dipole moment squared. As such the model does not distinguish between a few fluctuators with a large dipole moment and many fluctuators with a small dipole moment. The frequency shift  $\Delta\nu_0/\nu_0$  is related to equation 2.6 by introducing a filling factor  $F$ , which depends on the device geometry, and the electric field distribution [45].

$$\frac{\Delta\nu_0}{\nu_0} = -\frac{F}{2} \frac{\Delta\epsilon}{\epsilon} \quad (2.7)$$

Where the loss tangent is then described by  $Fnd^2/3\epsilon = F\tan\delta_i$ . As shown in figure 2.2, TLFs coupled to a resonator lead to a non-monotonic decrease in centre frequency with decreasing temperature. This continues until the minimum at the value  $T = \hbar\nu_0/2k_B$  after which, the complex digamma function dominates creating an increase in centre frequency with further decreases in temperature. The Kramers Kronig relation can be applied to equation 2.6, producing a model describing the behaviour of the Q under varying microwave drive. This derivation is comprehensively covered in references [18] [40] so only the relevant

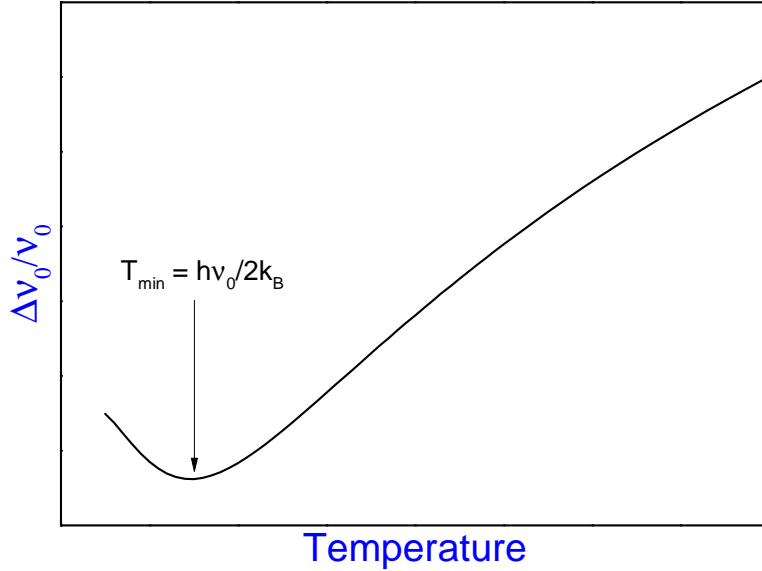


Figure 2.2: A plot simulating the general behaviour of a resonator's centre frequency as temperature is varied. The shift is due to TLFs and is described by equation 2.6. The minimum occurs at  $T = h\nu_0/2k_B$  while the magnitude of the total frequency shift scales with  $F\tan\delta$ .

parts are included here. In the weak field limit, the TLFs introduce a loss, resulting in

$$\frac{1}{Q_i} = F\delta_{TLS}^0 \tanh\left(\frac{\hbar\omega}{2k_B T}\right) \quad (2.8)$$

where  $Q_i$  is the resonator's internal quality factor and  $\delta_{TLS}^0$  is the intrinsic loss tangent at zero temperature (note this is not the same as the  $\delta_{TLS}$  determined from equation 2.6, although in practice, the two agree to within 20% [40]). Equation 2.8 implies a weak scaling of  $Q_i$  with temperature yet does not describe any dependence on the microwave drive. For this, we need to consider the strong field limit, which introduces a saturation factor to equation 2.8.

$$\frac{1}{Q_i} = \frac{F\delta_{TLS}^0 \tanh\left(\frac{\hbar\omega}{2k_B T}\right)}{\sqrt{1 + \left(\frac{E}{E_C}\right)^2}} \quad (2.9)$$

where  $E_C$  is the TLF saturation field and  $E$  the electric field (although these can equiv-

alently be replaced by the microwave drive  $P$  and saturation drive  $P_c$ ). The existence of this saturation relates to TLFs precessing much faster than any relaxation rates, resulting in the TLF being found 50% of the time in the ground state [40]. Figure 2.3 highlights the general behaviour of the quality factor due to equation 2.9. In this plot it is assumed that the only limiting losses are due to conductor losses and TLF losses, that is  $1/Q_i = 1/Q_{MB} + 1/Q_{TLF}$ , in reality more loss mechanisms exist complicating the analysis. The strength of this method is that it can be used on superconductors with a low  $T_c$ , where conductor losses due to Mattis-Bardeen theory would occur in parallel with the TLF losses in equation 2.8, an example of this is aluminium [14].

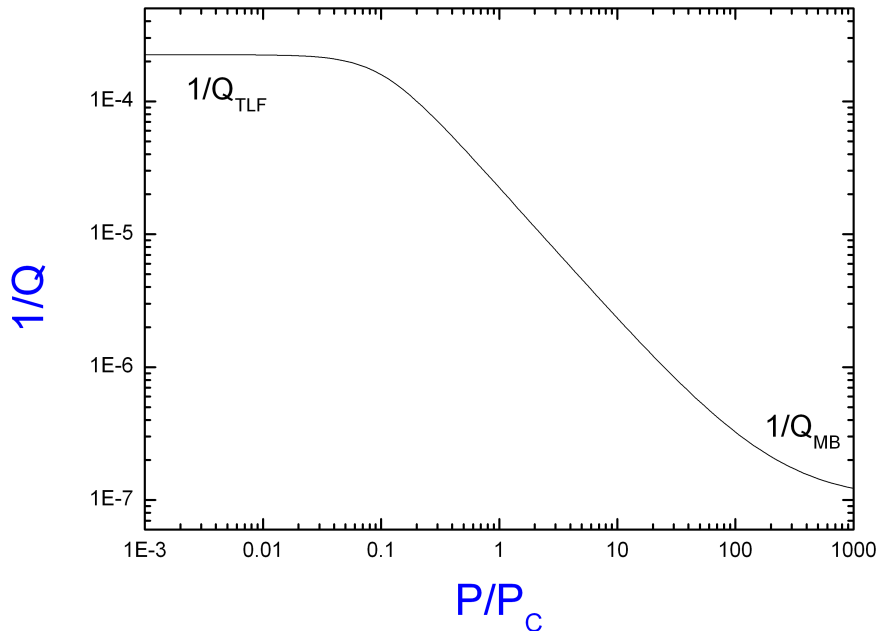


Figure 2.3: A plot showing the non-monotonic increase in  $1/Q_i$  with decreasing microwave drive. At microwave powers below a critical drive, the  $Q_i$  saturates at some lower value  $Q_{TLF}$ , in the ideal case the high power saturation occurs due to the Mattis-Bardeen limited energy loss  $Q_{MB}$ . The effect is exaggerated to more clearly show the behaviour.

# Chapter 3: The theory of superconducting resonators

## 3.1 Derivation of the quality factor and Mattis-Bardeen effects

One of the many reasons that interest exists in superconducting resonators is the low dissipation of the superconducting state. This should allow for very large intrinsic quality factors ( $Q_i$ ) in resonators constructed from such materials. The devices featured in this thesis are based upon LC “tank” circuits such as that shown in figure 3.1. For such an LC circuit, the centre frequency is given by  $\omega_0 = 2\pi\nu_0 = (LC)^{-1/2}$ , where  $L$  is the inductance, and  $C$  the capacitance. The quality factor is then defined as the energy in the resonator divided by the energy lost per period. Energy in the resonator is stored in the inductor  $E_m = Li^2/4$  and capacitor  $E_e = CV^2/4$  where  $i$  is the current and  $V$  the voltage, on average the energy is equal to twice either of these quantities. Power lost is described by  $P_{lost} = i^2R/2$  for a series LC circuit or  $P_{lost} = V^2/2R_{||}$  for a parallel LC circuit it follows that<sup>5</sup>

$$\begin{aligned}
 Q_i &= \omega_0 \frac{E_m + E_e}{P_{lost}} = 2\omega_0 \frac{E_m}{P_{lost}} \\
 &= 2\omega_0 \frac{\frac{CV^2}{4}}{\frac{V^2}{2R_{||}}} \\
 &= \omega_0 R_{||} C
 \end{aligned} \tag{3.1}$$

and for the series circuit

$$\begin{aligned}
 Q_i &= \omega_0 \frac{E_m + E_e}{P_{lost}} = 2\omega_0 \frac{E_m}{P_{lost}} \\
 &= 2\omega_0 \frac{\frac{Li^2}{4}}{\frac{i^2 R}{2}} \\
 &= \frac{\omega_0 L}{R}
 \end{aligned} \tag{3.2}$$

---

<sup>5</sup>Note these relations consider an oscillating voltage of amplitude  $V$ , or oscillating current of amplitude  $i$ . In terms of the RMS voltage the power lost would instead be given by  $P_{lost} = \langle V \rangle^2 / R = \langle i \rangle^2 R$ .

For a fixed centre frequency,  $Q_i$  scales inversely with any series resistance for a series LC circuit, or linearly with the parallel resistance in a parallel LC circuit. The inherent low dissipation of superconductors should make them suitable for producing high  $Q_i$  devices. Zero resistance is a property of superconductivity at DC, however, at higher frequencies (but still below the superconducting gap energy) surface resistance becomes finite, but still small enough to realise high quality factors.

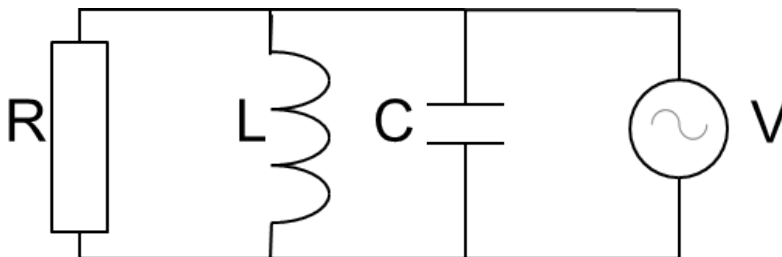


Figure 3.1: Schematic of a parallel tank circuit, consisting of a capacitor of capacitance  $C$ , inductor of inductance  $L$ , resistor of resistance  $R$  and driving voltage  $V$ .

In the presence of an electric field, Cooper pairs are accelerated. Their kinetic energy is stored due to the lack of dissipation and can be recovered by reversing the electric field. An applied magnetic field will penetrate a short distance  $\lambda_{Lon}$  and can also store energy. Together these effects create a complex surface impedance

$$Z_s = R_s + j\omega L_k \quad (3.3)$$

which describes the non zero AC surface resistance of a superconductor  $R_s$ , and the frequency dependent kinetic inductance  $L_k$ .  $R_s$  replaces  $R$  in equation 3.1 to become the important factor determining the  $Q_i$  of a superconducting resonator. The surface resistance varies with the quasiparticle density, which follows an exponential temperature dependence.

$$\rho_{qp}(T) = 2N(0)\sqrt{2\pi k_B T \Delta(0)} e^{-\Delta(0)/k_B T} \quad (3.4)$$

where  $T$  is the temperature,  $N(0)$  is the single spin density of electron states at the metal's Fermi energy and  $\Delta(0) \approx 3.5k_B T_c$  is the superconducting energy gap. Understanding

how the quasiparticle density relates to the surface impedance requires Mattis Bardeen theory [46] to describe the temperature dependence of the complex conductivity, which is given by  $\sigma_t = \sigma_1 + j\sigma_2$ . Here the conductivity is split into its real and imaginary components, the Mattis-Bardeen theory is used to describe how these components behave while the density of quasiparticles is varied. According to Mattis-Bardeen theory the imaginary part of the complex conductivity is described by

$$\frac{\sigma_2}{\sigma_n} = \frac{1}{\hbar\omega} \int_{\Delta-\hbar\omega}^{\Delta} \frac{[1 - 2f(u + \hbar\omega)](u^2 + \Delta^2 + \hbar\omega u)}{\sqrt{\Delta^2 - u^2} \sqrt{(u + \hbar\omega)^2 - \Delta^2}} du \quad (3.5)$$

where  $\Delta$  is the superconducting gap function,  $u$  the energy,  $f(u)$  the Fermi function and  $\sigma_n$  is the normal state conductivity just above  $T_c$ . A similar integral describes the real part of the complex conductivity.

$$\frac{\sigma_1}{\sigma_n} = \frac{2}{\hbar\omega} \int_{\Delta}^{\infty} \frac{[f(u) - f(u + \hbar\omega)](u^2 + \Delta^2 + \hbar\omega u)}{\sqrt{\Delta^2 - u^2} \sqrt{(u + \hbar\omega)^2 - \Delta^2}} du \quad (3.6)$$

The ratio of each of the integrals is used to determine the Mattis-Bardeen limited quality factor  $Q_{MB} = \frac{2\sigma_1}{\alpha\sigma_2}$  [15]. Where  $\alpha$  is the kinetic inductance fraction  $\alpha = \frac{L_k}{L_g + L_k}$  with  $L_g$  being the geometric inductance.  $\alpha$  is temperature dependent due to the kinetic inductance depending on the quasiparticle density. The behaviour of  $Q_{MB}$  with temperature is shown in figure 3.2. It should be noted that this describes the hard limit for the intrinsic quality factor of a superconducting resonator. Although figure 3.2 shows that in the low T limit  $Q_{MB}$  rapidly diverges, as such it rarely limits  $Q_i$  when below  $T_c/10$ .

## 3.2 Derivation of scattering parameters

Next the coupling to the resonator must be considered. We begin by first deriving the impedance of the tank circuit shown in figure 3.1. However, we are only interested in the behaviour around the resonant frequency. Therefore writing  $\omega = \omega_0 + d\omega$  allows the impedance of a parallel LC circuit  $Z_{LC||}$  to be calculated.

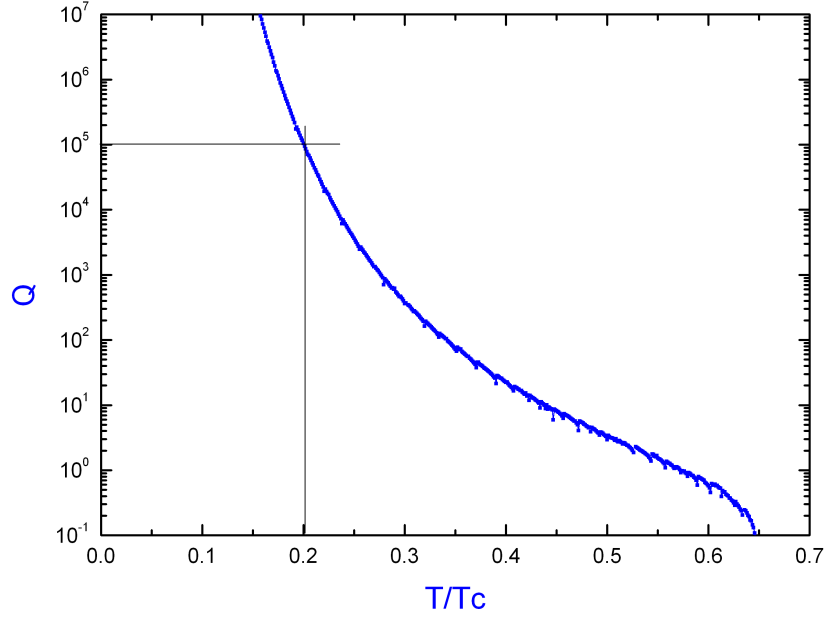


Figure 3.2: Plot showing how quality factor scales with normalised temperature. Plot generated using Mattis-Bardeen theory with niobium  $T_c = 9$  K and  $\alpha = 0.001$  at  $T = 0$  K, here  $\alpha$  acts as a scaling factor. The Mattis-Bardeen theory provides the hard limit on the quality factor for all superconducting resonators. In practice, superconducting resonators follow the curve at the high temperature end, but at low temperature other mechanisms prevent the quality factor from reaching the Mattis-Bardeen limit.

$$\begin{aligned}
Z_{LC\parallel} &= \left( \frac{1}{R} + \frac{1}{j\omega_0 L(1 + d\omega/\omega_0)} + j\omega_0 C(1 + d\omega/\omega_0) \right)^{-1} \\
&\simeq \left( \frac{1}{R} + j\frac{d\omega}{\omega_0^2 L} + jC d\omega \right)^{-1} \\
&\simeq \left( \frac{1}{R} + j2C d\omega \right)^{-1} \\
&\simeq \frac{R}{1 + j2CRd\omega} \\
&= \frac{R}{1 + j2Q_i d\omega/\omega_0} \\
&= \frac{R - 2jRQ_i(d\omega/\omega_0)}{1 + 4Q_i^2(d\omega/\omega_0)^2}
\end{aligned} \tag{3.7}$$

A coupling element will be added to this impedance to describe the total impedance of the resonator, where the resonator is considered as the LC tank circuit plus some coupling element. In general the coupling is modelled as being capacitive and achieved by including

an additional coupling capacitor to the circuit, however the coupling can be generalised to inductive coupling. Introducing an additional coupling capacitor will allow energy to be added to the resonator, but at the cost of allowing additional energy to leak from the resonator. This can be modelled with another quality factor,  $Q_c$ , associated with the coupling capacitance. The coupling capacitor is considered as connecting one plate to the tank circuit and the other to a feedline of impedance  $Z_l$ . The average energy stored within the feedline side of coupling capacitor is given by  $E_{cl} = \frac{1}{4}C_l V^2$ . Following the calculation by Mazin [15] the power lost through the coupling capacitor is given by  $P_{cc} = 2i^2 Z_0 = 2(\omega C_c V)^2 Z_0$  and the capacitance of the feedline is given by  $C_l = \frac{n\pi}{\omega_n Z_l}$ . Where  $Z_l$  is usually engineered to be close to  $Z_0$ , the characteristic impedance (defined as  $50 \Omega$  for the circuits in this thesis). For a lumped element resonator the  $n$  represents only the fundamental mode so that  $C_l = \frac{\pi}{\omega_0 Z_l}$ . Making use of this leads to a coupling quality factor given by

$$\begin{aligned}
Q_c &= 2\omega_0 \frac{E_{cl}}{P_{cc}} \\
&= \frac{1}{2}\omega_0 \frac{C_l V^2}{(2\omega C_c V)^2 Z_0} \\
&= \frac{1}{4} \frac{\pi}{(\omega C Z_0)^2}
\end{aligned} \tag{3.8}$$

There are now multiple quality factors describing a resonator. These combine by a sum of reciprocals, such that the observed loaded quality factor consists of  $\frac{1}{Q_L} = \frac{1}{Q_c} + \frac{1}{Q_i}$  where the internal quality factor,  $Q_i$ , covers loss due to Mattis-Bardeen and two level fluctuator effects. Loading the resonator with a coupling capacitor also changes the resonator impedance and hence its centre frequency. Therefore the new centre frequency needs to be calculated, this is achieved by considering the impedance of an additional coupling capacitor in series with the previously derived LC circuit impedance. These terms combine to give

$$Z_{res} = \frac{-j}{\omega C_c} + \frac{R - 2jRQ_i\left(\frac{\omega - \omega_0}{\omega_0}\right)}{1 + 4Q_i^2\left(\frac{\omega - \omega_0}{\omega_0}\right)^2} \tag{3.9}$$

the resonance condition is met by setting the imaginary part of the impedance to zero.

$$\text{Im}(Z_{res}) = \frac{-1}{\omega C_c} - \frac{2RQ_i\left(\frac{\omega-\omega_0}{\omega_0}\right)}{1 + 4Q_i^2\left(\frac{\omega-\omega_0}{\omega_0}\right)^2} = 0 \quad (3.10)$$

Defining  $R = \frac{4Q_i Z_0}{\pi}$  leads to a quadratic equation

$$4Q_i^2 \left(\frac{\omega - \omega_0}{\omega_0}\right)^2 + \frac{8Q_i^2 \omega C_c Z_0}{\pi} \left(\frac{\omega - \omega_0}{\omega_0}\right) + 1 = 0 \quad (3.11)$$

solving for  $\frac{\omega-\omega_0}{\omega_0}$  leads to

$$\begin{aligned} \frac{\omega - \omega_0}{\omega_0} &= -\frac{\omega C_c Z_0}{\pi} \pm \frac{\omega C_c Z_0}{\pi} \sqrt{1 - \left(\frac{\pi}{2Q_i \omega C_c Z_0}\right)^2} \\ &= -\frac{\omega C_c Z_0}{\pi} \pm \frac{\omega C_c Z_0}{\pi} \sqrt{1 - \left(\frac{Q_c}{2Q_i}\right)^2} \end{aligned} \quad (3.12)$$

In practice the resonator is designed such that  $Q_i \geq Q_c$ , this makes the square root term approximately 1. The positive solution then leads to  $\omega = \omega_0$  satisfying the resonance, this is the initial unloaded LC centre frequency. However, this frequency leads to a high impedance of the loaded resonator and hence reflection at the coupling capacitor. The negative solution is then more interesting, and leads to a new centre frequency which will be defined as  $\omega_n$ . To determine what this new centre frequency will be we need to define  $\delta\omega = \omega - \omega_0$  and  $\delta\omega' = \omega - \omega_n$  these combine to give

$$\frac{\omega_0 + \delta\omega - \omega_n}{\omega_n} = \frac{\delta\omega'}{\omega_n} \quad (3.13)$$

using this definition for the negative impedance solution, leads to

$$\frac{\delta\omega}{\omega_0} = \frac{\delta\omega'}{\omega_n} - \frac{2Z_0\omega_n C_c}{\pi} \quad (3.14)$$

which can be substituted into the expression for the impedance of the loaded resonator

$$\begin{aligned}
Z_{tot} &= \frac{1}{j\omega C_c} + \frac{Z_0 \frac{4Q_i}{\pi}}{1 + 2jQ_i \left(\frac{\delta\omega}{\omega_n}\right)} \\
&= \frac{1 + 2jQ_i \left(\frac{\delta\omega'}{\omega_n}\right) + j\omega C_c Z_0 \frac{4Q_i}{\pi}}{j\omega C_c - 2Q_i C_c \omega \left(\frac{\delta\omega'}{\omega_n}\right)} \\
&= \frac{1 + 2jQ_i \left(\frac{\delta\omega'}{\omega_n}\right)}{j\omega C_c - 2Q_i C_c \omega \left(\frac{\delta\omega'}{\omega_n}\right) + \frac{4Q_i C_c^2 \omega^2 Z_0}{\pi}} \\
&\approx \frac{\pi}{4Q_i C_c^2 \omega^2 Z_0} \left(1 + 2jQ_i \frac{\delta\omega'}{\omega_n}\right) \\
&= \frac{Z_0}{g} \left(1 + 2jQ_i \frac{\delta\omega'}{\omega_n}\right)
\end{aligned} \tag{3.15}$$

here  $g = \frac{4Q_i(Z_0 C_c \omega_n)^2}{\pi} = Q_i/Q_c$  is the coupling parameter. Therefore when  $g = 1$  then  $Q_i = Q_c$  so the resonator is critically coupled. It follows that  $g > 1$  results in over coupling the resonator and  $g < 1$  results in under coupling the resonator. This expression for a loaded LC resonator can describe both a lumped element resonator with a specified inductance and capacitance, or a distributed (geometric) resonator with an inductance and capacitance per unit length.

The loaded resonator appears as an abrupt change to the impedance. An applied signal will change due to the resonator's impedance, resulting in a transmission response and a reflection response. In a two port circuit these are called scattering parameters and are denoted by  $S_{ij}$  where the signal is applied from port  $j$  and received through port  $i$ . These relate to the ratio of voltages such that  $S_{ij} = V_j/V_i$ , therefore the transmission response is denoted  $S_{21}$ . The transmission response is therefore the ratio of the transmitted voltage to the input voltage and indicates the signal was applied from port 1 and measured in port 2. For completeness the reflection response is denoted by  $S_{11}$ , here the scattering parameter describe the ratio of the reflected voltage to the input voltage.

The scattering parameters can be obtained by use of the appropriate ABCD parameters for two-port circuits [47]. In general this thesis focuses on the use of lumped element

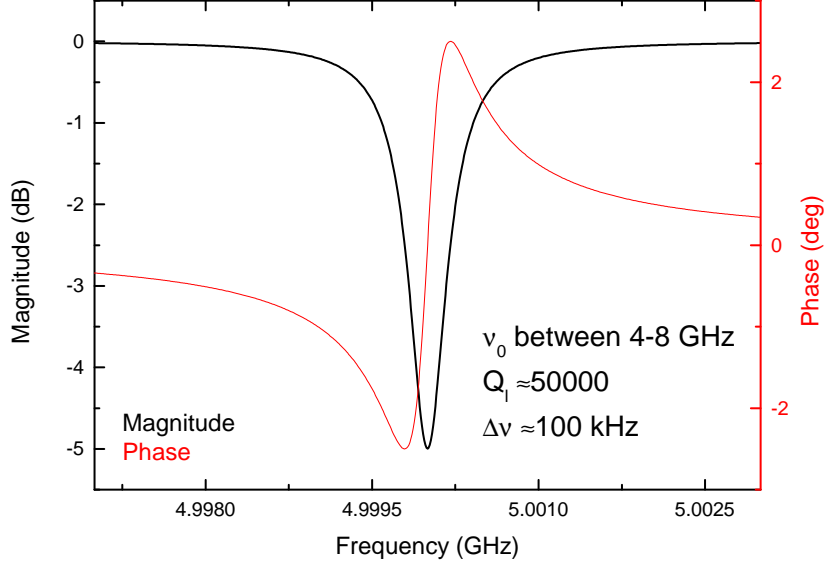


Figure 3.3: A plot showing the magnitude (in black) and phase (in red) response of a superconducting resonator described by equation 3.16 with  $\nu_0 = 5$  GHz,  $Q_i = 50000$  and  $g = 2$ . These values are representative of a typical resonator used within this thesis.

resonators. These resonators produce a notch response because the resonance provides high impedance to the transmission line, this is described by

$$S_{21}^{LE} = \frac{2(1 + 2jQ_i y)}{g + 2(1 + 2jQ_i y)} \quad (3.16)$$

where a normalised centre frequency of  $y = \frac{\delta\omega'}{\omega_n}$  has been used also it is common that equation 3.16 is rewritten in the form  $S_{21} = 2[2 + g/(1 + 2jQ_i y)]^{-1}$ . The magnitude and phase response of a resonator are found from equation 3.16 and are plotted in figure 3.3. For completeness, a quarter wavelength is also described by equation 3.16, but a half wavelength would produce a peak response, and is therefore described by

$$S_{21}^{\lambda/2} = \frac{2}{g + 2(1 + 2jQ_i y)} \quad (3.17)$$

Alternative derivations of similar resonators can be found in other literature [48] [49] [15], although the derivation in the thesis by Calvo [50] is particularly clear.

# Chapter 4: Measurement theory

This chapter outlines the important elements of oscillator theory required for performing noise measurements. The initial details cover phase sensitive homodyne detection and frequency sensitive Pound based detection. Then a section covers how noise processes can be understood. Next the Barkhausen relation for changing between the phase and frequency of a resonator near its centre frequency is introduced. Finally the Leeson frequency is covered to discuss its implications on noise measurements and the validity of when the Barkhausen relation can be applied.

## 4.1 Phase sensitive detection

In the previous chapter the circuit model describing a resonator was derived. Now we want to interrogate the resonator and to examine its dynamics. This could be to use the resonator as a detector by subjecting it to some external stimulus. However, in this thesis we are concerned with the dynamics of the unperturbed resonator. This is known as the intrinsic jitter to either the resonator's frequency or phase. This section will cover two methods of measuring the resonator to examine its intrinsic jitter.

Firstly the most common and well understood method of homodyne detection is covered. Some example schematics are presented and the mathematics of the detection is introduced. Then the problems of the method are evaluated. This is to justify the use of a different measurement technique known as Pound locking.

Homodyne detection is a phase sensitive method for measuring the phase difference between two different signal paths. The phase sensitive element in this method is known as a mixer, these have the effect of multiplying their two inputs to provide an output, which in this implementation is down-mixed. Figure 4.1 gives the basic schematic for a homodyne detection scheme. In essence, the signal is split into two paths, one which serves as a reference while the other features some device that produces a phase jitter. These paths recombine at the mixer, which produces a down-mixed DC signal with an amplitude dependent on the phase difference between the two signal paths. It is assumed that the dominant source of phase jitter should be the device under test. However at microwave

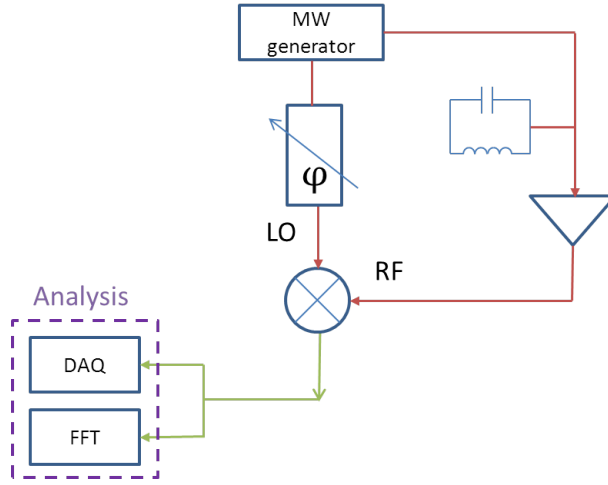


Figure 4.1: Schematic of a simple homodyne detection setup. Shown are signals at RF (red) and DC (green). The microwave generator output is split into two signal paths. One passes through the resonator, while the other acts as a reference path. A mixer is then used to recombine the signals and measures the phase difference between the resonator path and the reference path.

frequencies where the wavelengths concerned are of order  $\sim 10$  mm, an appreciable phase shift can occur due to vibrations of cables. As such the use of semi-rigid coaxial lines and vibration isolation is required for moderate phase stability. In practice, a phase shifter is used in the reference arm to put the two arms into quadrature. The mixer output consists of sum and difference terms as shown by

$$A\cos(\omega t + \theta_a) * B\cos(\omega t + \theta_b) = \frac{AB}{2} [\cos(\theta_a - \theta_b) + \cos(2\omega t + \theta_a + \theta_b)] \quad (4.1)$$

where a low pass filter is used to remove the sum term, resulting in only the DC term which is dependent on the phase difference.

$$\frac{AB}{2}\cos(\theta_a - \theta_b) = \frac{AB}{2}\cos(\Delta\theta_{ab}) \quad (4.2)$$

By using the phase shifter in the reference path to keep the two arms in quadrature, the output DC voltage will then be zero. Since the gradient of the cosine is steepest around 0 this is the point of highest sensitivity.

$$V_{phase} = \frac{AB}{2}\cos(\Delta\theta_{ab}) \quad (4.3)$$

Phase jitter in either path will produce a non-zero phase voltage. The strength of the homodyne technique is that it operates at a constant frequency (where the output stability of a synthesizer is optimally low), and the phase resolution at the mixer is very good. To an initial approximation the method has no amplitude sensitivity due to changes in amplitude being unable to produce a non-zero phase voltage. However, if both a phase jitter and amplitude jitter are present, then the now non-zero phase voltage is sensitive to amplitude fluctuations. In practice this can be prevented by the use of an IQ mixer to allow separate measurement of the amplitude and phase variations, such setups are common and conclude the amplitude fluctuations to be much smaller than those of the phase [51]. Even with the improvement of an IQ mixer, the homodyne technique is still susceptible to phase variations from either signal path and crucially it cannot isolate the variations from just the device path.

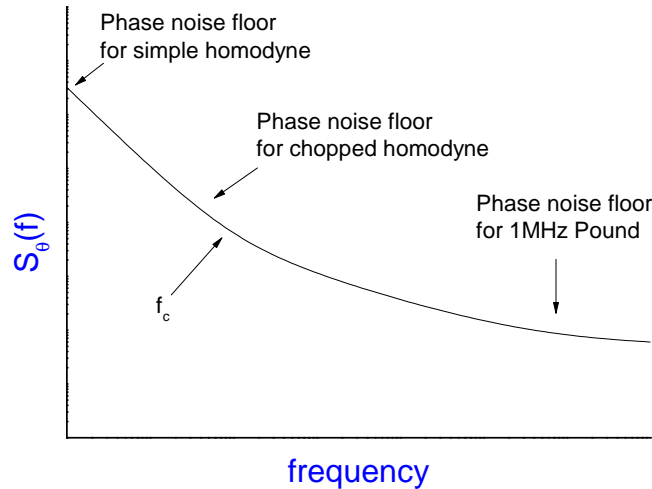


Figure 4.2: A plot showing the general phase noise shape, highlighting the system noise floor as a function of operating frequency. Simple homodyne setups suffer from *close-in* noise, this is somewhat mitigated by chopping the down-mixed signal. Higher operating frequencies (well above the flicker corner  $f_c$ ) can be obtained from phase modulation as used in the Pound technique.

Homodyne detection suffers from *close in* noise, this is high levels of low frequency noise which occur within the electronics required in the setup (the mixers and amplifiers).

This can be measured by removing the resonator from figure 4.1 and measuring the jitter of the amplifier chain. This is a measurement of the systematic phase noise, an example of this type of measurement is shown in figure 4.2. The reason that homodyne detection suffers is that the detection is performed at the same frequency as the carrier. Resulting in an offset frequency of 0 Hz, so the relevant noise floor is shown at 0 Hz in figure 4.2. If the detection can be performed at a different frequency then a better position against the noise floor can be obtained. Figure 4.3 shows the use of an additional mixer at the input which is driven by a square wave signal. The result is to chop the input signal, which can later be synchronously detected. This is an example of a “chopped” homodyne setup, where the use of an offset frequency (equal to the square wave repetition rate) has led to better positioning on the system noise floor. Typically this allows for offset frequencies of a few kHz, but this may not be above the systematic flicker corner frequency  $f_c$ . Room temperature electronics are not the only cause of the *close in* noise. High low frequency noise will also occur due to slow drifts in the resonator itself as well as slow phase fluctuations from vibrations in the measurement cables. These reasons prompted this project to look at alternative method, that could deal with these problems.

## 4.2 Frequency sensitive detection

An ideal detection method would not have any ambiguity as to which path created the jitter. This can be achieved by only using only one path, a method capable of this is Pound locking, a technique which is over 50 years old [52]. This approach is well known within NMR [53], was used to test general relativity in the Pound-Rebka experiment [54], and has been adapted for use in precision frequency metrology as the Pound-Drever-Hall setup [29] [55]. Here, the carrier is phase modulated sufficiently fast that side bands separated from the carrier by the frequency of the phase modulation are created. The carrier signal is tuned to be on resonance and sent to the resonator. To prevent the phase sidebands from interacting with the resonator the modulation frequency must be set to larger than the resonator bandwidth.

A diode is then used to rectify this signal (both the carrier and sidebands), having the effect of squaring all terms and so the resultant signal is an envelope at the phase modula-

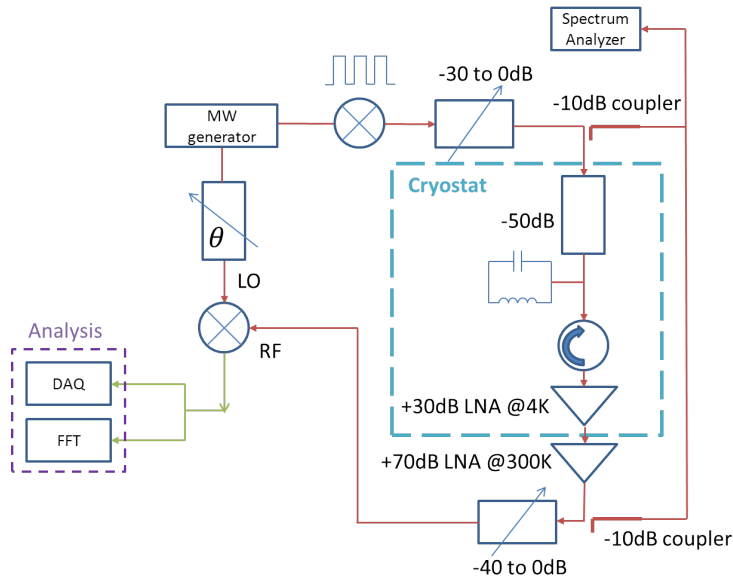


Figure 4.3: A schematic of a real homodyne detection scheme. Shown are signals at RF (red) and DC (green). A square wave drives the input mixer to chop the signal, this is synchronously detected to help alleviate susceptibility to low frequency noise. The power input to the sample can be varied, this power is detected using a spectrum analyser.

tion frequency containing the now phase shifted carrier. The importance of this envelope is that in operating at the phase modulation frequency (which is much smaller than the carrier frequency), the resulting wavelength is much larger leading to a huge suppression of vibration based phase jitter. A lock-in amplifier can then be used to extract the phase shifted carrier, sampling of this voltage can be used to perform noise measurements.

Feedback can be readily implemented into a Pound circuit by feeding the lock-in signal into a PID controller which attempts to null the input signal. The PID controller calculates a voltage expected to null its input, and sends this out to a VCO (which acts as the source synthesizer in figure 4.4). The VCO then varies its frequency output based on the input voltage it receives. In the next subsection, the mathematics of the Pound circuit is derived to show that it produces an error signal where the zero-crossings correspond to the resonance condition being met. This means that the PID is actively locking to the resonance. Additionally within the vicinity of the zero-crossing the error signal obeys a linear dependence, which greatly simplifies the feedback requirements.

The major advantage of the Pound based method is the use of only one signal path, that

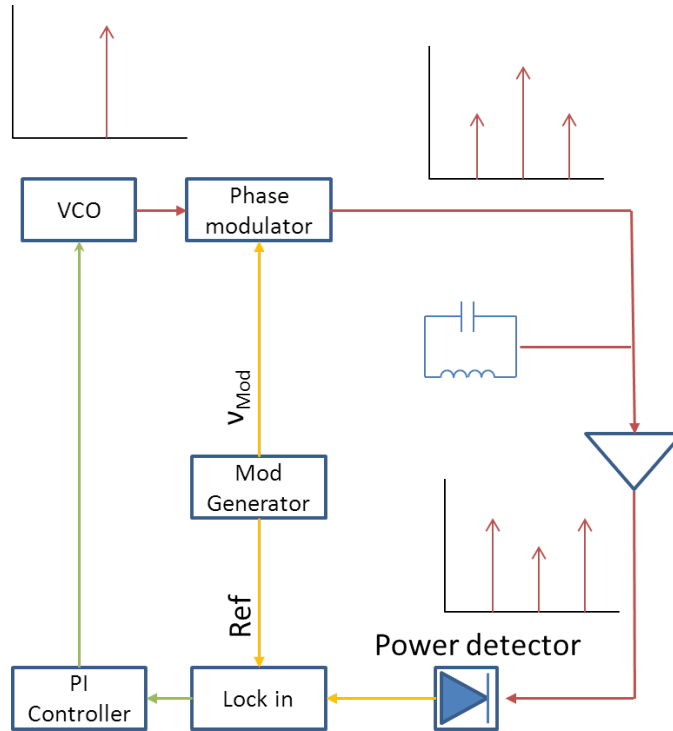


Figure 4.4: A schematic of a simple Pound detection setup. Shown are signals at RF (red), 1 MHz (yellow) and DC (green). The VCO outputs an RF carrier signal, while a second generator drives a phase modulator at 1 MHz. The carrier is phase modulated resulting in the creation of phase sidebands. A diode acts as a power detector to rectify the signal for narrow band detection using a lock-in amplifier.

is shared by the carrier and the sidebands. The sidebands are sufficiently separated to not interact with the resonator, but are close enough to allow for a large common mode rejection of any phase jitter experienced by both the carrier and its sidebands. This, along with the high offset frequency (due to phase modulation at 1 MHz) lead to the much improved positioning on the system noise floor, as shown in figure 4.2. Furthermore the feedback allows for knowledge of when the resonator drifts, allowing for any detrimental divergence to be accounted for. This means that while the timespan of a homodyne measurement is limited by the time taken for the resonator to drift outside of the homodynes optimal position, there is no such limitation on the measurement time for the Pound setup. It also follows that the diode will later be shown to be insensitive to amplitude fluctuations resulting in an unchanging slope of the error signal, reducing sensitivity to an amplitude jitter.

### 4.3 Pound theory

To understand the Pound method, we consider an incident voltage  $V_{inc}$ , of amplitude  $V_0$  and at frequency  $\omega_c$ . This frequency is near the resonant frequency of our resonator,  $\omega_0$ . The carrier is phase modulated at a frequency  $\omega_m$  which is several times larger than the resonator bandwidth  $\Delta\omega$ .

$$V_{inc} = V_0 e^{j(\omega_c t + \beta \sin \omega_m t)} = \begin{pmatrix} J_0(\beta) e^{j\omega_c t} \\ + J_1(\beta) e^{j(\omega_c + \omega_m)t} - J_1(\beta) e^{j(\omega_c - \omega_m)t} \\ + J_2(\beta) e^{j(\omega_c + 2\omega_m)t} - J_2(\beta) e^{j(\omega_c - 2\omega_m)t} + \dots \end{pmatrix} V_0 \quad (4.4)$$

Where  $\beta$  is the modulation index, which relates to the ratio of microwave power within the carrier relative to the sidebands. The Pound setup uses a modulation index such that almost all the power is within the carrier and the first two phase sidebands ( $J_0$ ,  $J_1$  and  $J_2$ ). The Pound technique requires transmission off resonance to ensure transmission of the phase sidebands, this means that a notch type resonance is required. Where, full transmission occurs off resonance and reduced transmission occurs within the resonance. This allows the phase sidebands to transmit without interacting with the resonator, while the carrier undergoes some amplitude and phase change within the resonance. For a resonator with a peak response it is common that a circulator is used to recreate a notch response from the measurement of the reflected signal. However, in our implementation the chip already produces the desired notch response. Considering the  $S_{21}(\omega)$  (where  $\omega$  is the frequency to evaluate  $S_{21}$  at, for example  $S_{21}(\omega_c + \omega_m)$  means evaluating  $S_{21}$  at the upper phase sideband which has a frequency of  $\omega_c + \omega_m$ ) leads to

$$V_{inc} = \begin{pmatrix} J_0(\beta) S_{21}(\omega_c) e^{j\omega_c t} \\ + J_1(\beta) S_{21}(\omega_c + \omega_m) e^{j(\omega_c + \omega_m)t} - J_1(\beta) S_{21}(\omega_c - \omega_m) e^{j(\omega_c - \omega_m)t} \\ + J_2(\beta) S_{21}(\omega_c + 2\omega_m) e^{j(\omega_c + 2\omega_m)t} - J_2(\beta) S_{21}(\omega_c - 2\omega_m) e^{j(\omega_c - 2\omega_m)t} + \dots \end{pmatrix} V_0 \quad (4.5)$$

where the conjugate of the this voltage is given by

$$V_{inc}^* = \left( \begin{array}{l} J_0(\beta)S_{21}^*(\omega_c)e^{-j\omega_c t} \\ + J_1(\beta)S_{21}^*(\omega_c + \omega_m)e^{-j(\omega_c + \omega_m)t} - J_1(\beta)S_{21}^*(\omega_c - \omega_m)e^{-j(\omega_c - \omega_m)t} \\ + J_2(\beta)S_{21}^*(\omega_c + 2\omega_m)e^{-j(\omega_c + 2\omega_m)t} - J_2(\beta)S_{21}^*(\omega_c - 2\omega_m)e^{-j(\omega_c - 2\omega_m)t} + \dots \end{array} \right) V_0 \quad (4.6)$$

the power ( $P \propto V_{inc}V_{inc}^*$ ) can be detected using a diode and is given by

$$\left[ \begin{array}{l} \left( \begin{array}{l} J_0(\beta)S_{21}(\omega_c)e^{j\omega_c t} \\ + J_1(\beta)S_{21}(\omega_c + \omega_m)e^{j(\omega_c + \omega_m)t} - J_1(\beta)S_{21}(\omega_c - \omega_m)e^{j(\omega_c - \omega_m)t} \\ + J_2(\beta)S_{21}(\omega_c + 2\omega_m)e^{j(\omega_c + 2\omega_m)t} - J_2(\beta)S_{21}(\omega_c - 2\omega_m)e^{j(\omega_c - 2\omega_m)t} \end{array} \right) \\ \left( \begin{array}{l} J_0(\beta)S_{21}^*(\omega_c)e^{-j\omega_c t} \\ + J_1(\beta)S_{21}^*(\omega_c + \omega_m)e^{-j(\omega_c + \omega_m)t} - J_1(\beta)S_{21}^*(\omega_c - \omega_m)e^{-j(\omega_c - \omega_m)t} \\ + J_2(\beta)S_{21}^*(\omega_c + 2\omega_m)e^{-j(\omega_c + 2\omega_m)t} - J_2(\beta)S_{21}^*(\omega_c - 2\omega_m)e^{-j(\omega_c - 2\omega_m)t} \end{array} \right) \end{array} \right] V_0^2 \quad (4.7)$$

This simplifies to DC components, terms at  $\omega_m$  (with both in phase and quadrature components), and also higher harmonics  $2\omega_m$ ,  $3\omega_m$  and  $4\omega_m$ . The higher order terms are neglected since the lock-in will extract only terms at modulation frequency, leaving the in phase component

$$\left( \begin{array}{l} J_0(\beta)J_1(\beta)S_{21}(\omega_c)S_{21}(\omega_c + \omega_m)^*e^{-j\omega_m t} - J_0(\beta)J_1(\beta)S_{21}(\omega_c)S_{21}(\omega_c - \omega_m)^*e^{j\omega_m t} \\ + J_0(\beta)J_1(\beta)S_{21}(\omega_c)^*S_{21}(\omega_c + \omega_m)e^{j\omega_m t} - J_0(\beta)J_1(\beta)S_{21}(\omega_c)^*S_{21}(\omega_c - \omega_m)e^{-j\omega_m t} \end{array} \right) V_0^2 \quad (4.8)$$

where the exponentials can be expanded into sin and cos terms.

$$\left( \begin{array}{l} S_{21}(\omega_c)S_{21}(\omega_c + \omega_m)^*\cos(\omega_m t) - jS_{21}(\omega_c)S_{21}(\omega_c + \omega_m)^*\sin(\omega_m t) \\ - S_{21}(\omega_c)S_{21}(\omega_c - \omega_m)^*\cos(\omega_m t) - jS_{21}(\omega_c)S_{21}(\omega_c - \omega_m)^*\sin(\omega_m t) \\ S_{21}(\omega_c)^*S_{21}(\omega_c + \omega_m)\cos(\omega_m t) + jS_{21}(\omega_c)^*S_{21}(\omega_c + \omega_m)\sin(\omega_m t) \\ - S_{21}(\omega_c)^*S_{21}(\omega_c - \omega_m)\cos(\omega_m t) - jS_{21}(\omega_c)^*S_{21}(\omega_c - \omega_m)\sin(\omega_m t) \end{array} \right) V_0^2 J_0(\beta)J_1(\beta) \quad (4.9)$$

Since this is now a function within an envelope at  $\omega_m$  the phase of the lock-in can be adjusted to extract only the real terms, so we only consider the real part of the  $S_{21}$

parameter for the cosine terms. However, we need to consider  $\text{Re}S_{21}\text{Im}S_{21}$  combinations for the Sine terms. We now make use of the  $S_{21}$  parameter derived earlier.

$$S_{21} = \frac{2(1 + 2jQ_i y)}{g + 2(1 + 2jQ_i y)} \quad (4.10)$$

Where  $g$  is a coupling parameter and  $y$  is the normalised centre frequency  $\frac{(\nu - \nu_0)}{\nu_0}$ , considering  $S_{21}$  at  $\omega_c + \omega_m$  means taking  $2\pi\nu = \omega_c + \omega_m$ . Evaluating the real and imaginary parts of the  $S_{21}$  parameter leads to  $\text{Re}S_{21}^* = \text{Re}S_{21}$  and  $\text{Im}S_{21}^* = -\text{Im}S_{21}$ . Applying this leads to all cosine terms cancelling and produces the following combinations for the Sine terms.

$$\left( \begin{array}{l} +\text{Re}S_{21}(\omega_c)\text{Im}S_{21}(\omega_c + \omega_m) - \text{Im}S_{21}(\omega_c)\text{Re}S_{21}(\omega_c + \omega_m) \\ +\text{Re}S_{21}(\omega_c)\text{Im}S_{21}(\omega_c - \omega_m) - \text{Im}S_{21}(\omega_c)\text{Re}S_{21}(\omega_c - \omega_m) \\ +\text{Re}S_{21}(\omega_c)\text{Im}S_{21}(\omega_c + \omega_m) - \text{Im}S_{21}(\omega_c)\text{Re}S_{21}(\omega_c + \omega_m) \\ +\text{Re}S_{21}(\omega_c)\text{Im}S_{21}(\omega_c - \omega_m) - \text{Im}S_{21}(\omega_c)\text{Re}S_{21}(\omega_c - \omega_m) \end{array} \right) V_0^2 J_0(\beta) J_1(\beta) \sin(\omega_m t) \quad (4.11)$$

Which simplifies to

$$2J_0(\beta)J_1(\beta)V_0^2 \sin(\omega_m t) \left( \begin{array}{l} \text{Re}S_{21}(\omega_c)[\text{Im}S_{21}(\omega_c + \omega_m) + \text{Im}S_{21}(\omega_c - \omega_m)] \\ -\text{Im}S_{21}(\omega_c)[\text{Re}S_{21}(\omega_c + \omega_m) + \text{Re}S_{21}(\omega_c - \omega_m)] \end{array} \right) \quad (4.12)$$

where the lock-in amplifier is referenced to the modulation frequency. This means it extracts the coefficient in front of the  $\sin(\omega_m t)$  term, leading to the error signal

$$V_{error} \propto 2J_0(\beta)J_1(\beta)V_0^2 \left\{ \begin{array}{l} \text{Re}S_{21}(\omega_c)[\text{Im}S_{21}(\omega_c + \omega_m) + \text{Im}S_{21}(\omega_c - \omega_m)] \\ -\text{Im}S_{21}(\omega_c)[\text{Re}S_{21}(\omega_c + \omega_m) + \text{Re}S_{21}(\omega_c - \omega_m)] \end{array} \right\} \quad (4.13)$$

This agrees with the expression of Black [55] and is depicted in figure 4.5. Here the error signal crosses zero three times, corresponding to the carrier being at resonance and each phase side band being at resonance. The amplitude of the central crossing (the carrier) is twice that of the phase side bands (assuming the modulation index is appropriately chosen). The carrier zero-crossing can always be determined by checking the direction of the crossings, since the sidebands both cross from one direction, whereas the carrier

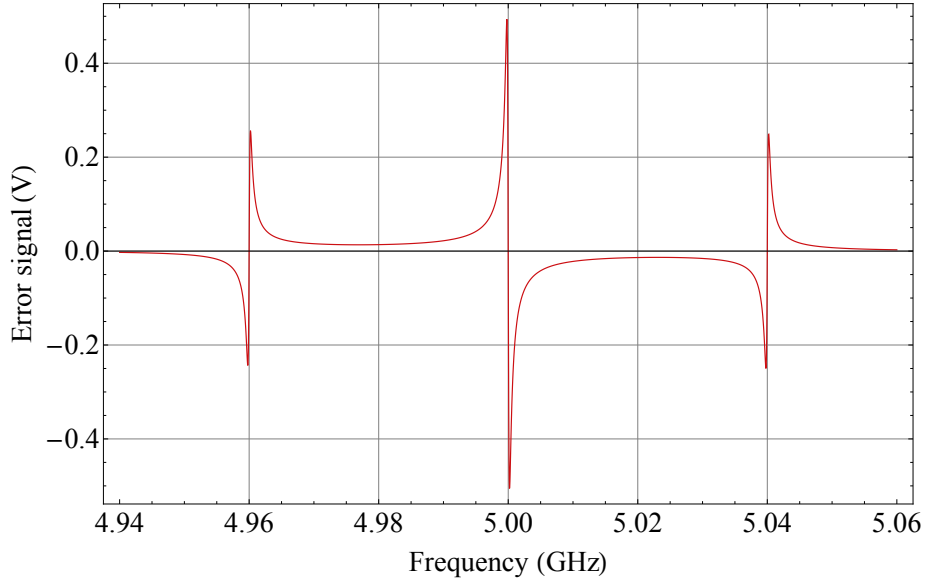


Figure 4.5: A plot of the Pound error signal as a function of carrier frequency using equation 4.13, where zero crossings correspond to the resonance condition being met. The loop is operated in the vicinity of the central zero crossing.

crosses from the other direction. The feedback loop is completed by a PID controller which attempts to null the error signal. This means care must be taken to ensure the correct zero crossing is chosen for the lock.

So far we have neglected the DC terms which appear as

$$V_{error} \propto V_0^2 \left\{ \begin{array}{l} J_0^2(\beta) S_{21}^2(\omega_c)^2 \\ + J_1^2(\beta) [S_{21}(\omega_c + \omega_m)^2 + S_{21}(\omega_c - \omega_m)^2] \\ + J_2^2(\beta) [S_{21}(\omega_c + 2\omega_m)^2 + S_{21}(\omega_c - 2\omega_m)^2] \end{array} \right\} \quad (4.14)$$

these can be further simplified by realising that far outside of resonance the  $S_{21}$  response is 1. When the carrier is resonant (i.e. when the loop is locked on resonance) the  $S_{21}$  parameters for the  $J_1(\beta)$  and  $J_2(\beta)$  terms are 1. This is due to the modulation frequency being much larger than the resonator bandwidth, thus we get

$$V_{error} \propto V_0^2 \{ J_0^2(\beta) S_{21}^2(\omega_c)^2 + 2J_1^2(\beta) + 2J_2^2(\beta) \} \quad (4.15)$$

where the DC terms do not contribute to the error signal, but can affect detector efficiency

by saturating the diode. The remaining  $S_{21}$  parameter also acts to suppress the carrier (which would otherwise be at the highest power and could saturate the diode). A further simplification can be applied to the error signal. Within the vicinity of a zero-crossing, the error signal can be linearised with respect to carrier frequency as

$$V_{error} \propto V_0^2 \frac{4gQ_i}{(g+2)^2} y \quad (4.16)$$

hence the error signal scales linearly with the normalised carrier frequency  $y$ . Then the gradient of the error signal is dependent on the unloaded quality factor and the coupling strength (which combine to form a non-linear function of the uncoupled quality factor). It also scales linearly with the power detected by the diode. Low powers reaching the diode lead to the gradient decreasing. This results in small frequency deviations (frequency in figure 4.5) corresponding to very small correction voltages (error signal voltage in figure 4.5). However, if the power is too low then the gradient can become essentially flat, making the zero crossing appear broad to the PID controller. This corresponds to the PID not being able to lock – resulting in a continual linear drift of the VCO modulation voltage. These effects can be slightly compensated for by increasing the voltage-to-frequency conversion factor, which indirectly increases the gain. This highlights the need to maximise the power seen at the diode. Therefore, all amplification and filtering must be performed before the detection diode.

#### 4.4 The effects of asymmetric resonances

It is important to know whether the resonance is symmetric before locking to the zero crossing (resonance) with the Pound loop. This is since a symmetric resonance has a phase zero-crossing at the same point as its maximal amplitude response, this is not true for an asymmetric resonance. Resonator asymmetry occurs because of conduction paths existing in parallel with the resonator [56]. They can be modelled simply by allowing the coupling parameter  $g$  to be complex [57]. The effect of increasing resonance asymmetry is shown in figure 4.6, the minimum of the real response stops occurring at the same frequency as the phase zero-crossing.

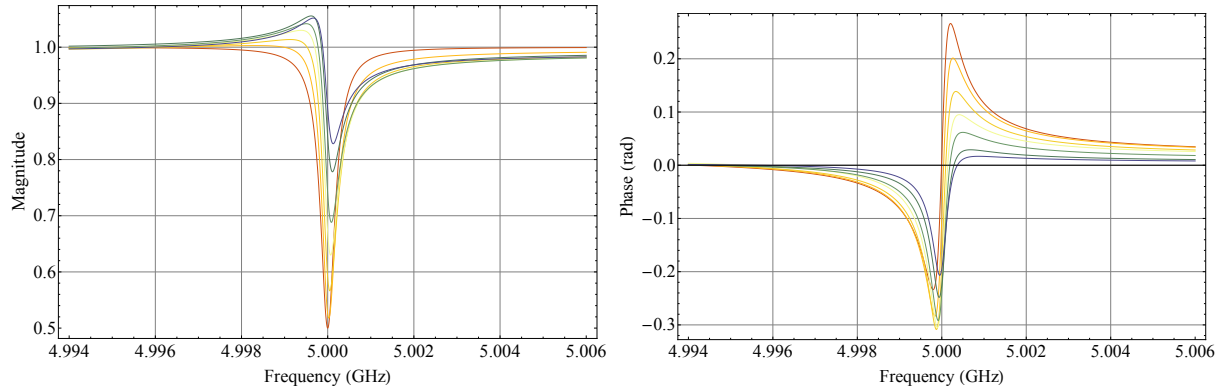


Figure 4.6: Two plots showing the magnitude and phase response of an increasingly asymmetric resonance. The red curve shows a real coupling parameter  $g$ . Then the magnitude of the imaginary component of  $g$  is increased through the colour transition orange to blue. As asymmetry is increased the minimum of the magnitude response shifts, so that the phase zero-crossing stops representing the resonant frequency.

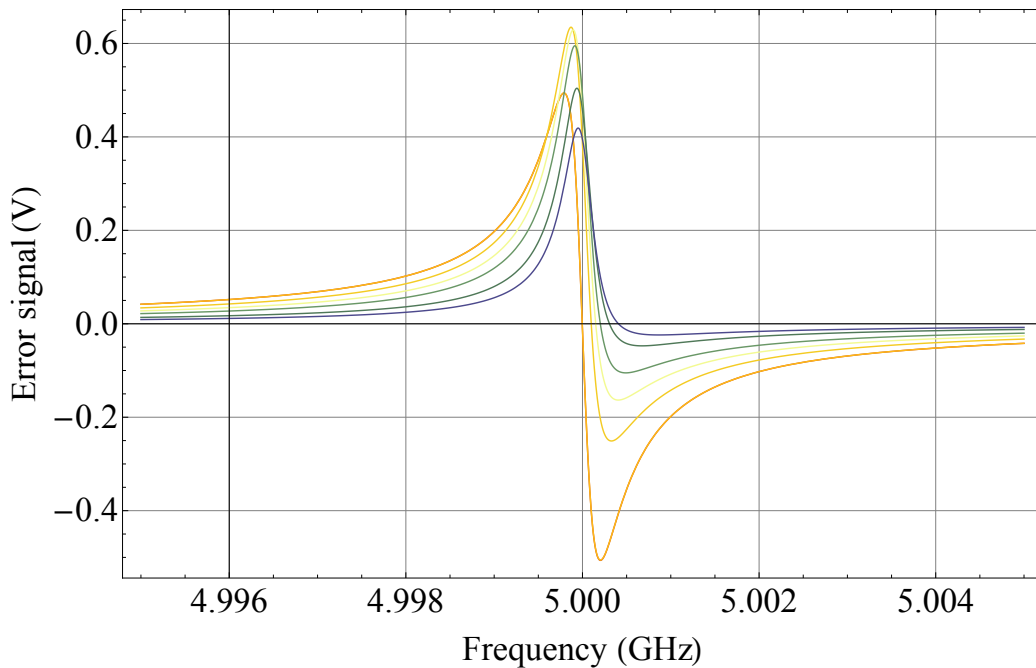


Figure 4.7: A plot showing the Pound error signal for an increasingly asymmetric resonance. The red curve shows a real coupling parameter  $g$ . Then the magnitude of the imaginary component of  $g$  is increased through the colour transition orange to blue. Note as with figure 4.6 the position of the zero-crossing no longer represents the resonant frequency.

Two problems arise with an asymmetric resonance, firstly the error signal zero crossing stops representing the resonant frequency and secondly the magnitude of the error signal

becomes smaller (leading to a reduced sensitivity). The first problem can be overcome by using a non-zero set point on the PID controller, effectively compensating for the “false” resonant frequency. However, the second problem causes a reduced sensitivity to frequency fluctuations and inhibits operation at ultra low powers. In the ultra low power limit, these problems become compounded as the error signal becomes flatter, which in turn prevents the use of a non-zero set-point, ultimately forcing the resonator to be tracked at a frequency that is not the resonant frequency, this is shown in figure 4.7.

## 4.5 Fluctuations

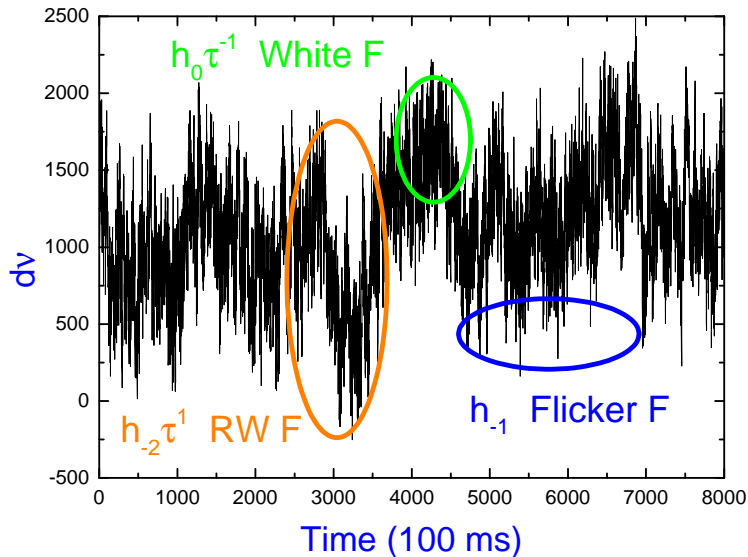


Figure 4.8: A plot showing the centre frequency of a resonator as a function of time. The centre frequency is readout at a rate of 100 Hz using the Pound method described previously. Circled are three commonly observed noise processes, white frequency (green), random walk of the frequency (orange) and flicker frequency noise (blue).

Having investigated the resonance model and the theory for two different measurement setups, the next step is to cover the analysis of fluctuations and how to relate them to noise processes. This follows other related works which also looked into this problem (although with different methods) these are covered in the theses of Mazin [15], Gao [18],

Barends [17], and featured later in the literature review. Fluctuations warrant study since they are an undesired, and problematic effect. In fact, the study of electronic noise has spanned decades. In the general case, the properties of some quantity are measured as a time series using a convenient electronic instrument. The fluctuations are understood by generating some statistics relating the quantity at several instances in time and thus measuring the deviation that occurred within the time span. Commonly, the time series of data is studied using spectral analysis.

Within this thesis the quantity that is measured as a time series is the centre frequency of a resonator. This is shown in figure 4.8, which demonstrates the appearance of some noise processes within the raw time series. The next section will outline how the common noise processes within resonators appear under various analysis techniques. It will also introduce time based statistics which are not common to this field.

### **Noise understood by power laws**

From either spectral or time based analysis, a noise process can be quantified by its slope in the power spectrum. By fitting the slope the noise behaviour is approximated, i.e. is the noise diverging with time, and if so how strongly. From this analysis, several common power laws appeared and have corresponding names. These are outlined in figure 4.9 which highlights the common noise processes and how they behave in the different analysis environments. This figure exists to aid in the understanding of noise processes and the plots that appear later in the thesis. The colours used in figure 4.9 match those used in figure 4.8. This is to highlight how noise processes appear in the raw data and allow comparison to the appearance after analysis. These plots demonstrate that white frequency noise is a fast process (dominates over short timescales) which appears as a rapid oscillation in the raw data. At longer timescales the flicker frequency process dominates, appearing as a series of almost equally spaced sharp spikes in the raw time series. Finally the slow switching behaviour represents the random frequency walk, which acts as a background for the other two processes to act on top of.

The use of a common notation in terms of  $h_i$  and  $b_i$  parameters is introduced in figure 4.9 and is described in table 4. This plot demonstrates that the fundamental spectrum is that

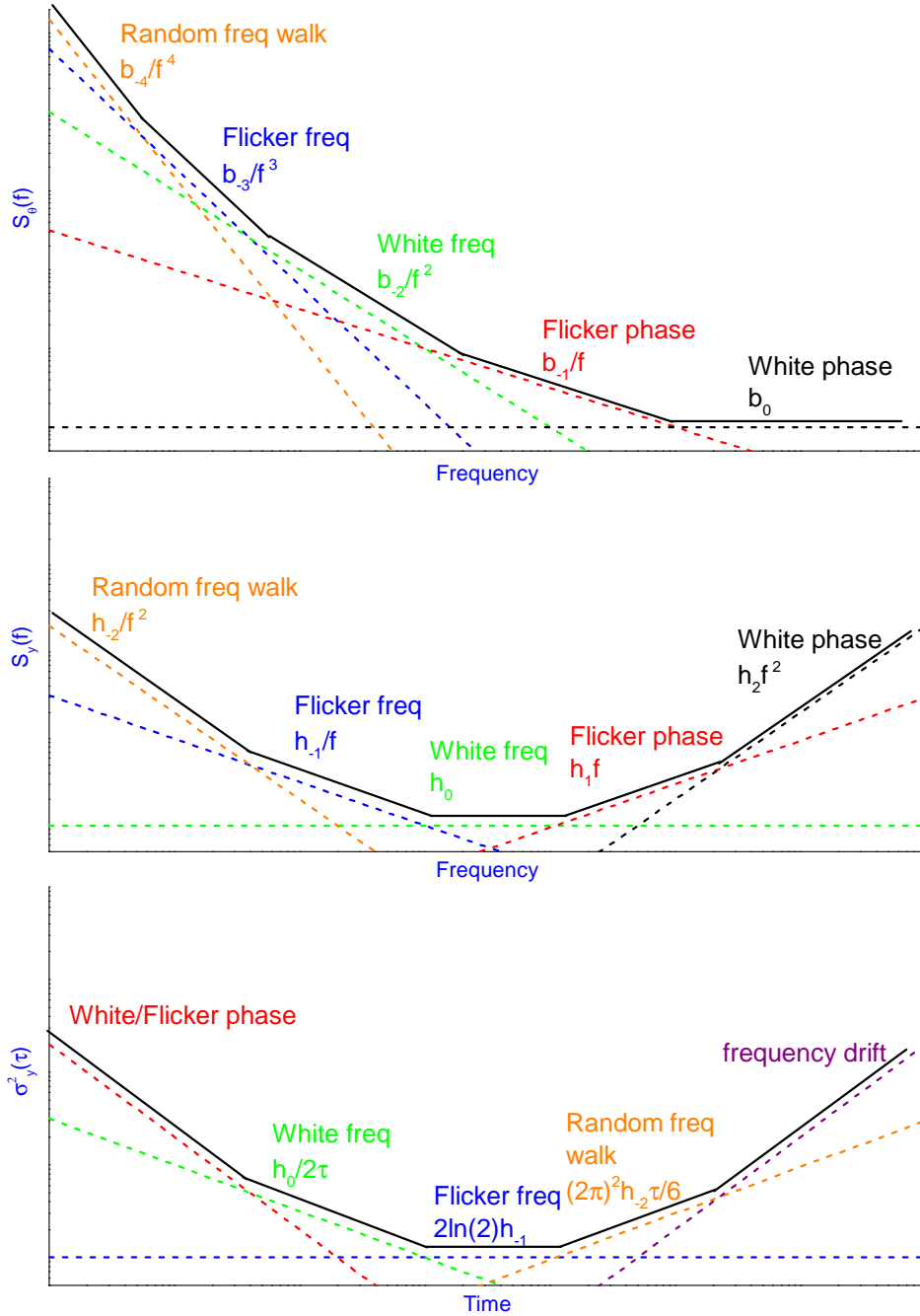


Figure 4.9: A plot comparing the phase spectrum  $S_\theta$ , frequency spectrum  $S_y$  and Allan variance  $\sigma_y^2$  (all in log-log scale). The plot exists to aid in understanding the later noise measurements. Plot details how a noise process can be understood by power laws and how each process scales for the chosen analysis method. Table 4 can be used to switch between analysis methods. Plot is adapted from Rubiola [58]

of phase fluctuations  $S_\theta$ , a homodyne measurement on an amplifier would measure its spectrum of phase fluctuations. In this case the noise floor is described by the white phase process  $b_0$ . The final section of this chapter examines the Leeson frequency, this is a timescale of a resonator which determines whether one is probing the spectrum of phase fluctuations or the spectrum of frequency fluctuations  $S_y$ <sup>6</sup>. It follows that typically one actually measures the spectrum of frequency fluctuations when studying a resonator. In the spectrum of frequency fluctuations the noise floor is shown to be the white frequency process ( $h_0$ ) and the  $b_0$  process is instead drift like at high frequencies. All measurements in this thesis will be sensitive to only the spectrum of frequency fluctuations, so only the middle or bottom plots of figure 4.9 will be used. The top plot is included for the discussion of the Leeson frequency (covered in section 4.7) and to highlight differences between measurements in this thesis and those covered in the literature review.

For example flicker frequency noise is described by  $S_y = h_{-1}/f$ , while white frequency noise obeys  $S_y = h_0$  where  $h_{-1}$  and  $h_0$  are usually constants. However these are only true within the spectrum of frequency fluctuations. Within the spectrum of phase fluctuations  $S_\theta$  the flicker frequency noise is instead described by  $S_\theta(f) \propto b_{-3}/f^{-3}$ . Finally figure 4.9 shows that if the analysis is performed in the time domain then the flicker frequency noise is described by a  $\sigma_y \propto \tau^0$  slope. Table 4 demonstrates how one can extract the  $h_i$  (or  $b_i$ ) parameter to interchange between the frequency spectrum  $S_y$ , the phase spectrum  $S_\theta$  or Allan variance  $\sigma_y^2$ . Analysis using Allan statistics is preferred in this thesis in part because of the ability to identify frequency drifts (the  $\tau^2$  slope in the bottom plot of figure 4.9). These drifts obscure the existence of other processes when using spectral analysis.

This thesis focuses on the study of the  $h_{-1}$  parameter which describes the level of flicker frequency noise within a resonator ( $S_y(f) \propto h_{-1}/f$ ). The behaviour of the  $h_{-1}$  will be measured in later chapters, which will make heavy use of table 4. The next subsection covers spectral analysis and the Allan deviation. Although the last section on the Leeson

---

<sup>6</sup>The fractional frequency spectra ( $S_y$  in units of 1/Hz) is defined as the Fourier transform of the autocorrelation of frequency deviations and is given by  $S_y = \frac{S_{d\nu}}{\nu_0^2} = \lim_{T \rightarrow \infty} \int_0^T \int_0^T \frac{\langle \delta f(t_1) \delta f(t_2) \rangle}{\nu_0^2} e^{jf(t_1 - t_2)} dt_1 dt_2$ , where  $S_{d\nu}$  is the frequency spectra (in units of Hz/Hz<sup>2</sup>),  $\nu_0$  is the nominal centre frequency of the resonator, and  $f(t_i)$  the Fourier frequency

frequency is needed to distinguish between the spectrum of phase fluctuations and the spectrum of frequency fluctuations.

Table 4: Noise types by power law, adapted from Rubiola [58]

Noise type	$S_\theta(f)$	$S_y(f)$	$S_\theta \leftrightarrow S_y$	$\sigma_y^2(\tau)$
White PM	$b_0$	$h_2 f^2$	$h_2 = \frac{b_0}{\nu_0^2}$	$\frac{3f_H h_2}{(2\pi)^2} \tau^{-2}$ <sup>a</sup>
Flicker PM	$b_{-1} f^{-1}$	$h_1 f$	$h_1 = \frac{b_{-1}}{\nu_0^2}$	$A \times \frac{h_1}{(2\pi)^2} \tau^{-2}$ <sup>b</sup>
White FM	$b_{-2} f^{-2}$	$h_0$	$h_0 = \frac{b_{-2}}{\nu_0^2}$	$\frac{1}{2} h_0 \tau^{-1}$
Flicker FM	$b_{-3} f^{-3}$	$h_{-1} f^{-1}$	$h_{-1} = \frac{b_{-3}}{\nu_0^2}$	$2 \ln(2) h_{-1}$
Random walk FM	$b_{-4} f^{-4}$	$h_{-2} f^{-2}$	$h_{-2} = \frac{b_{-4}}{\nu_0^2}$	$\frac{(2\pi)^2}{6} h_{-2} \tau$
Linear frequency drift				$\frac{1}{2} (y)^2 \tau^2$ <sup>c</sup>

<sup>a</sup>Valid only when  $2\pi f_H \tau \gg 1$

<sup>b</sup>Where  $A = [1.038 + 3 \ln(2\pi f_H \tau)]$

<sup>c</sup>Highlights that linear frequency drifts are not identifiable by spectral analysis

## Analysis in the frequency domain

Spectral analysis begins by describing the correlation of a noisy signal  $z(t)$  at different points in time, this is called auto-correlation. If the noisy signal has a known mean  $\kappa_i$  and variance  $\sigma_i^2$ , then its autocorrelation between times  $t_1$  and  $t_2$  is given by

$$R(t_1, t_2) = \frac{X[(z(t_1) - \kappa)(z(t_2) - \kappa)]}{\sigma_{t_1} \sigma_{t_2}} \quad (4.17)$$

Where  $X$  is the expectation operator (this is the first moment of a random variable, in the case of a Gaussian process it is also the mean). It is assumed the process is bounded (has a non zero and non-infinite variance). This assumption can be problematic for the study of ultra stable processes; where one may need to average for very long times to observe a non-stationary variance. The autocorrelation function will have a value between -1 and 1, where perfect correlation is indicated by 1 and anti-correlation is indicated by -1.

If the noisy signal has a time independent mean and variance, then the autocorrelation can be rewritten in its more familiar form.

$$R(\tau) = \frac{X[(z(t) - \kappa)(z(t + \tau) - \kappa)]}{\sigma^2} = \langle z(t)z(t + \tau) \rangle \quad (4.18)$$

Here, it has been assumed that the autocorrelation only depends on the separation in time of the noisy function. For analysis of fluctuations, the Wiener-Khinchin theorem is used to translate the autocorrelation function to the power spectral density by a Fourier transform.

$$S_y(\omega) = \int_{-\infty}^{\infty} \langle z(t)z(t + \tau) \rangle e^{-i\omega\tau} d\tau = 2 \int_0^{\infty} \langle z(t)z(t + \tau) \rangle e^{-i\omega\tau} d\tau \quad (4.19)$$

The relevant examples for this case are the noisy signals with a Gaussian distribution. This applies for any resistor at finite temperatures, which exhibits Johnson noise. The autocorrelation of such a function is sharp around  $\tau = 0$ , producing a flat power spectrum. As a second example a single time-scale exponential decay leads to a Lorentzian-like power spectrum, producing a roll off at the inverse of the single characteristic time-scale.

Two problems arise from the spectral analysis method when studying noise processes. Firstly, the noise often results in a time dependent variance, which results in an ill-defined autocorrelation and hence power spectrum. To get around this, a measurement must span a long time to reach domains when the noise has a variance that is nearly time independent (such as flicker limited). In this case, care is needed when looking at the power spectrum as it is only valid at low Fourier frequencies which correspond to the large time limit. Although at such time scales the the autocorrelation does not perform much averaging to be statistically confident. Consequently this leads to low confidence in the region where the autocorrelation is well defined. Most importantly, the non-standardised use of both windowing, and the handling of the numerical pole at zero, make it very difficult to make accurate and valid comparisons to other spectra. This is especially true when studying low frequency noise, where the numerical pole at zero ensures spectral analysis will always diverge in the low frequency limit. It is for these reasons that in this thesis we prefer to perform analysis in the time domain.

## Analysis in the time domain

If a noisy signal has a time varying variance, or if one wants to perform valid comparisons to other measurements, then another method is needed to measure the nature of fluctuations with high confidence. One can begin by simply studying the time dependence of the mean and variance. For a white frequency noise process, this was found to be sufficient (the mean and variance both converge with increasing time). This indicates that for a frequency independent noise process averaging will improve resolution. However, it was found that for all other noise processes, the standard variance was divergent [59] [60] [61], making the standard variance an insufficient analysis method, this is shown in figure 4.10.

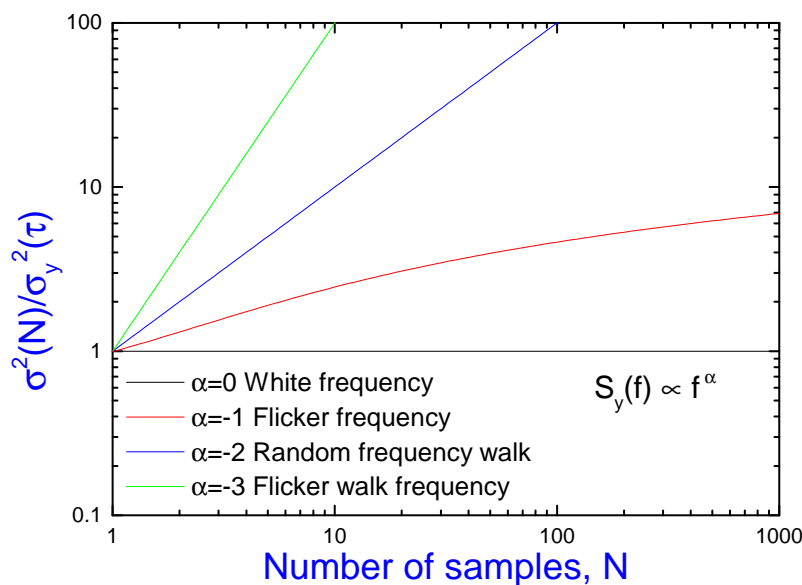


Figure 4.10: a plot showing how the ratio of the standard variance for N samples by the time average of a two sample variance varies with the number of samples, N. The plot highlights the divergent behaviour of the standard variance for various noise types, described by the value of  $\alpha$ . This plot is adapted from the NIST frequency metrology pages [62]

To understand this divergence, consider a data set characterised by a strong flicker frequency component. This results in a slow non-random (i.e. cannot be reduced by averaging) drift in a quantity. Therefore as the number of samples is increased, the portion

of samples that are sufficiently separated that they become affected by the flicker increases. Consequently the classical variance will diverge as the number of samples is increased. This happens for any slow drift-like noise process, as can be seen in Figure 4.10. To get around this the Allan (or two sample) variance was created. The Allan variance is non divergent for all noise processes and for a resonator can be determined by

$$\sigma_y^2(\tau) = \frac{1}{2(M-1)} \sum_{i=1}^{M-1} (\bar{y}_{i+1} - \bar{y}_i)^2 \quad (4.20)$$

where  $\bar{y}_i$  is the  $i$ th of  $M$  mean fractional frequency values over the measurement interval  $\tau$ , which is usually some  $n$  multiples of the base clock interval  $\tau_0$ . Additionally, the Allan variance ( $\sigma_y^2$ ) relates to an Allan deviation ( $\sigma_y$ ) as  $\sigma_y = \sqrt{\sigma_y^2}$ . Further, the Allan variance can be improved, to use all possible combinations of the data set, this is achieved by overlapping the samples and known as the overlapping Allan variance.

$$\sigma_y^2(\tau) = \frac{1}{2m^2(M-2m+1)} \sum_{j=1}^{M-2m+1} \left\{ \sum_{i=j}^{j+m-1} (\bar{y}_{i+m} - \bar{y}_i) \right\}^2 \quad (4.21)$$

Here the averaging time is now denoted by  $\tau = m\tau_0$ . Although computationally intensive, this calculation greatly improves statistical confidence at long time scales. Hence, it is especially useful for the analysis of slow processes and is the standard metric for metrology applications. After calculating the Allan variance, the Allan deviation is usually plotted in a so-called sigma-tau plot. This plot is read as the jitter magnitude (from the Allan deviation) which is found when measuring for a given period  $\tau$ . Figure 4.9 shows how to understand a sigma-tau plot compared to the phase spectrum and frequency spectrum.

## 4.6 Barkhausen relation

Having covered the various measurement and analysis methods, this section will now detail the differences between the measurement of frequency fluctuations and phase fluctuations. This begins with the Barkhausen relation, which relates the frequency and phase response of a resonator. Then the Leeson frequency is introduced to examine when the Barkhausen relation is valid. The Barkhausen relation makes use of the resonator circuit

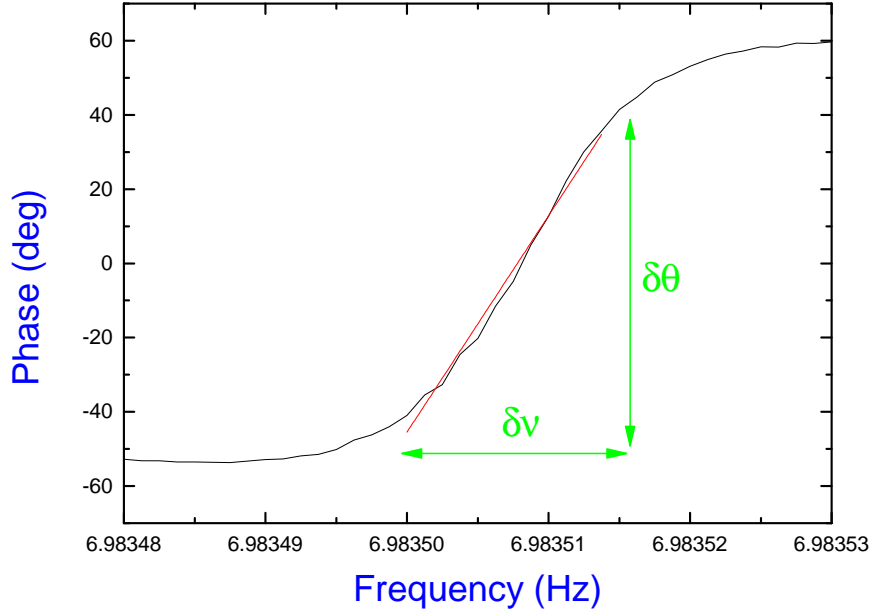


Figure 4.11: A plot showing the measured phase response of a typical resonator used in this thesis. In the vicinity of resonance the phase response is linear allowing the phase-to-frequency shift to be calculated using the Barkhausen relation. Note this plot is effectively a zoom in of the phase response shown in figure 3.3.

model, where the transmission parameter was found to be  $S_{21}^{LE} = 2[2 + \frac{g}{1+2jQ_i y}]^{-1}$ , where the  $y = (\nu_0 - \nu)/\nu$  is the normalised centre frequency. A zoom of the measured phase response of a resonator is shown in figure 4.11. The linear region of the phase response of a resonator can be described by the following statements in the Barkhausen relation [58].

$$\frac{\delta\omega}{\omega_0} = \frac{\delta\nu}{\nu_0} = \frac{\delta\theta}{2Q_L} \quad \text{for} \quad \frac{\delta\nu}{\nu_0} \ll \frac{1}{2Q_L} \quad (4.22)$$

This expression assumes a critical coupling to the resonator, which is rarely realised in real devices. Equation 3.16 can be used to produce an equivalent expression which allows for a non critically coupled resonator.

$$\frac{\delta\nu}{\nu_0} = \frac{g}{8Q_L} \quad (4.23)$$

For the resonator shown in figure 4.11, the centre frequency is 6.9 GHz and  $Q_L = 35000$ . The measured slope is found to have a gradient given by  $5.8 \times 10^{-3}$  degrees per Hz, using

equation 4.22 the gradient is found to be  $8 \times 10^{-3}$  degrees per Hz, but the resonator is not critically coupled. In this instance using equation 4.23 leads to a gradient of  $7 \times 10^{-3}$  degrees per Hz, which is very close to the Barkhausen estimate. The strength of the Barkhausen relation is to provide a very useful relation between the frequency and phase of a resonator without making any assumptions on the resonator itself. It should be noted that the linear part of the phase transmission scales with the resonator bandwidth. This means it is only linear for approximately  $\Delta\nu/10$  which for the resonator in figure 4.11 corresponds to a frequency shift of 20 kHz. Any noise process that moves towards the extremes of this limit will require more careful analysis to understand the corresponding phase-frequency conversion<sup>7</sup>. Additionally any noise process outside of this range will result in rapidly decreasing phase sensitivity.

## 4.7 The Leeson frequency and its effects

Care must be taken when studying the noise properties of any resonator, due to the need to consider the ratio of several frequency scales. Firstly there is the resonator centre frequency and secondly there is the frequency at which the resonator is interrogated. Finally there is the frequency which is based upon the natural ringing time of the resonator. The resonator and its coupling describe the centre frequency as was shown in Chapter 3. The coupling was also shown to produce the loaded quality factor  $Q_L$ , the natural ringing time of a resonator [58] is then defined by

$$f_L = \frac{1}{\tau_{ring}} = \frac{\nu_0}{2Q_L} \quad (4.24)$$

While the measurement frequency may be chosen, the Leeson frequency and the centre frequency are direct properties of the resonator and its coupling. This means that in general they cannot be changed without either producing another resonator or changing the experimental setup to vary the coupling. Within resonators, the Leeson frequency

---

<sup>7</sup>In later measurements of the jitter in superconducting resonators this limit is approached. This can be seen in figure 8.8 where the jitter at -100 dBm is around 4 kHz for short times. This prevented the study of noise at higher frequencies, as this jitter level rapidly increases with decreasing measurement time. Additionally it made measurement at lower microwave drives difficult. This was later circumvented by improvements to the setup and by lowering the measurement frequency to 100 Hz, where the noise level is lower (even at lower microwave drives).

creates a limit for when the Barkhausen relation in the previous section can be applied. More precisely the Leeson frequency determines whether a measurement is sensitive to the instantaneous phase or not.

To explain the instantaneous phase, consider a photon within a resonator with a given  $Q_L$ . This photon will exist within the resonator for  $\tau_{ring}$  before escaping, for a lumped element resonator like that considered in the previous chapter, this means the photon travels between the inductor and the capacitor approximately  $Q_L$  times. The instantaneous phase is considered as being sensitive to the phase of the photon every time it makes the transition from the capacitor to the inductor. This is important if the photon experiences a phase jitter each time it enters the capacitor. Then within the ringing time the photon would experience approximately  $Q_L$  kicks to its phase. This would lead to much larger (“tanked up”) phase jitter. If one wishes to measure the size of the jitter then they need to be aware of whether they are measuring the single kick which requires sensitivity to the instantaneous phase. If not they are measuring a “tanked up” effect, this important difference is covered in the noise as power laws section at the end of this chapter. Here noise processes are related to various spectra, where the measurement of instantaneous phase will produce the spectrum of phase fluctuations  $S_\theta$ , known as the phase noise. However, if the phase is measured at a frequency less than the Leeson frequency then the resulting spectrum is actually that of the frequency fluctuations  $S_y$ .

The Barkhausen relation can be used on any measurement of the spectrum of frequency fluctuations. This means the relation holds when the measurement time is larger than the ringing time. If however the measurement was sensitive to the instantaneous phase, then the Barkhausen relation no longer holds. In this case the spectrum of phase and frequency fluctuations are described by the following relation [58].

$$S_y = \frac{f^2}{\nu_0^2} S_\theta \quad (4.25)$$

Here  $f$  is the Fourier frequency and  $S_y$  is the spectrum of fractional frequency fluctuations. Note that a noise process obeying a given power law,  $1/f^\alpha$  where  $\alpha$  is well defined will see the value of  $\alpha$  change by  $\pm 2$  when moving between the two types of spectra.

The second important point to consider is what happens when the sampling frequency is lower than the Leeson frequency. In this case, regardless of the detection mechanism used, the measurement is *not* sensitive to the instantaneous phase and hence cannot directly measure the spectrum of phase fluctuations. This means the measurement actually produces a spectrum of frequency fluctuations.

Here, the Barkhausen relation can be applied, and the spectrum can be re-expressed in units usually associated with the phase spectrum (dBc/Hz), however, this is still the spectrum of *frequency* fluctuations. One way to understand this when looking at a typical frequency spectrum is to realise that a roll off occurs above the Leeson frequency. The roll off is generally the steepest slope of the measurement, as this part of the spectrum has become sensitive to the instantaneous phase. Equation 4.25 must be used to keep the measurement consistent with the rest of the graph, the slope needs to be multiplied by a Fourier factor (which makes the roll off less steep). Table 4 covers the details of this conversion completely for all noise processes.

To describe this in experiments, first we consider a measurement of the centre frequency vs time, made directly with the Pound technique. A Fourier transform of this  $d\nu(t)$  data series will result in the spectrum of frequency fluctuations  $S_y$ . An analogous measurement is possible using a homodyne setup to produce a measurement of the phase shift as a function of time. The Barkhausen relation can then be used to turn the time series of phase shifts  $d\theta(t)$  into that of frequency shifts  $d\nu(t)$ . Now for frequencies below the Leeson frequency the Fourier transform of this data set will produce the spectrum of frequency fluctuations  $S_y$ . However for the frequencies above the Leeson frequency, the Barkhausen relation is no longer valid. Therefore the Fourier transform should be taken of just of the phase shifts with time  $d\theta(t)$ , which will now produce the spectrum of phase fluctuations  $S_\theta$ . Now equation 4.25 must be used to produce the spectrum of frequency fluctuations from the spectrum of phase fluctuations.

It should be noted that when phase noise is explicitly measured, it is usually done with a resonator that has a  $Q_L$  which is sufficiently high that the Leeson frequency is lowered to a few Hz. This means that only modest sampling rates are required to be sensitive to the instantaneous phase. Importantly this also allows long time scales to be examined without

increased computation due to the size data set size. The advantage of a measurement sensitive to the instantaneous phase is that most noise types rapidly converge in the phase spectrum, so only modest offset frequencies are required to attain ultra high stability.

Within this thesis, the sampling frequency is always kept below the Leeson frequency. This is to remove any ambiguity that the spectrum of frequency fluctuations is always being measured. It is also because measurements focus on the behaviour of the flicker component of the noise. Being a low frequency noise processes, this requires long measurement times to gain high statistical confidence. Here the low sampling rate helps to reduce the computation required for the subsequent analysis. The Leeson frequency has been introduced because the Literature review will show that many other studies of resonator noise have occurred where the sampling frequency was above the Leeson frequency. This means that additional care is needed when performing any analysis, and some results can be simply explained by the Leeson frequency.

# Chapter 5: Literature review

The relevant background for this literature review is split into several sections. These are general measurements on resonators, then the study of noise (generally  $1/f$ ) in charge sensitive devices and finally onto noise measurements on superconducting resonators.

Superconducting electronics are attractive due to the inherent low loss and macroscopic quantum behaviour of the superconducting state. As the temperature is decreased towards zero, excitations of Cooper pairs should tend to zero. Without such excitations devices should be less “noisy” (less susceptible to unwanted dissipative mechanisms). This should allow the lifetime of a quantum state to become large. In these cases, the fundamental noise limitation should be due to Cooper pair generation-recombination (g-r noise) which can be reduced by lowering the temperature [63].

In both QIP (Quantum Information Processing) and detector applications, the g-r noise is not found to be the limiting factor [64], instead excess noise exists which limits coherence [2] or detector sensitivity [1]. To describe the excess noise behaviour, this review will follow the progress of superconducting resonators. This review will explain the basic understanding as of 2013, by which point the noise has been found to be similar to that in other superconducting or charge sensitive devices. For this reason it is useful to overview noise studies in single electron transistors and Josephson junctions and to relate these noise processes to decoherence.

The thesis of Mazin [15] details the early progress on work in kinetic inductance detectors [1]. Early work examined the temperature dependence of the superconducting resonator centre frequency [15]. This suggested that excess noise did not originate from mechanisms relating to superconductivity, a result that was verified when Al resonators on Sapphire were found to be less noisy than Al on Si [15]. This prompted a study into substrates motivated by the idea that the dielectric was responsible for the excess noise.

To verify the substrate dependence, first the superconductor had to be ruled out. Using the Mattis-Bardeen framework the effect of conductivity changes due to the population of quasi-particles can be explained [46]. It follows that when  $T$  is lower than approximately

$T_c/10$  the superconductivity mechanism saturates [42]. This meant that Al with its low  $T_c$  is a bad choice for exploring substrate dependence. Consequently higher  $T_c$  superconductors such as Nb [65], NbN [66], Ta [67], NbTiN [43] and TiN [68] were used in later work.

When measuring Ta and Nb resonators on Si a frequency shift was found to occur at temperatures below  $T_c/10$  [42]. Importantly the shift was a decrease in frequency with decreasing temperature, which is the opposite of the Mattis-Bardeen effect, therefore the shift was attributed to TLFs but not explored further. Additionally, this work demonstrated a saturation of the quality factor (instead of following the Mattis-Bardeen limit). While similar effects can be found in the Mazin thesis, the first modelling of the frequency shift with temperature was done by Gao et al. [45]. This provided a framework for comparison of the “density” (in fact  $Fnd^2$ ) of TLFs across different superconductor and substrate combinations. The examination of many substrate and superconductor combinations is crucial. This is because the  $nd^2$  term describes the number of TLFs and their dipole moment squared. Since the microscopic origin of TLFs is still not known, this framework allows measurements to quantify a reduction in the density of TLFs. There is however a complication, where the  $F$  term describes the geometric filling factor which relates to the electric field distribution of the resonator. In essence this means it is possible to create a resonator with reduced sensitivity to TLFs. Although the real goal would be to keep  $F$  constant and then observe a reduction in  $nd^2$  which would relate to the microscopic origin of TLFs.

In parallel work, it was realised that the “density” of TLFs could also be extracted by measuring the change in  $Q_i$  with microwave drive [14]. This was also the first study of many substrates with Al as the superconductor. Using this method the  $T_c$  is not important, as the microwave drive can be varied in the low temperature limit. This work highlighted SiO<sub>2</sub> to have a loss tangent approximately 10 times larger than high resistivity Si or sapphire.

Evidence that TLF loss could be an interface effect came from depositing additional dielectric layers over the resonators. While this was found to increase the frequency shift at low temperatures, the shift was found to be independent of the dielectric thickness [43]. However, this work did not quantify the magnitude of the increase in the loss tangent. Next the frequency dependence of the TLF loss was studied, finding that it was the same

for resonators of varying centre frequencies [37]. This work concluded that the “density” of TLFs is frequency independent across the 4–8 GHz range. It also determined that Nb on r-cut Sapphire exhibited very low dielectric loss and a weaker power dependence than Nb on SiO<sub>2</sub>, and that this weaker dependence can be explained by some newer TLF models [69]. Further evidence of TLF loss being an interface effect came from experiments removing parts of the dielectric. Specifically, removing the dielectric beneath the superconductor (where the electric fields were highest), was found to produce a decrease in the frequency shift compared to the basic design [8].

In measurements of quality factor vs microwave drive in varying temperatures, Macha et al. found evidence for the loss rate to be temperature dependent [70]. Such behaviour fits well within the TLF picture. It also verified that TLF effects only become apparent at temperatures below 800 mK. Attempts to minimise the loss tangent while maintaining a large kinetic inductance ratio led to numerous papers involving superconducting nitrides. These led to measurements approaching single photon energies which showed that NbTiN maintained intrinsic quality factors of  $\approx 5 \times 10^5$  [71] and TiN of  $\approx 1 \times 10^6$  [39] [9]. Modelling of TLF contributions from various locations found the metal-substrate and metal-air surfaces to be dominant [72]. While this agrees with observed behaviour, it also helps describe the observed geometry dependence [38] for films that underwent identical fabrication processes. Further measurements have verified the agreement of loss tangent measurements obtained by both quality factor vs power and frequency vs temperature [40]. Final evidence for the TLF model can be found in the observation that pumping of harmonics leads to a decreased loss rate and improved quality factors at low powers [41]. Many of these experiments involving TLF behaviour can be found in the review by Zmuidzinas [7].

The properties of superconducting resonators in applied magnetic fields has also been extensively studied. Approaches to tunable resonators were demonstrated in both independent resonators [19] and resonators containing SQUIDs [73]. Tunability of resonators is needed for fine coupling to various quantum systems [74]. While attractive, applied magnetic fields have been shown to be detrimental to the quality factor of superconducting resonators [75]. Attempts to mitigate these problems have been studied using various dotted ground-plane structures [76] [77]. The importance of these effects was recently

emphasised when measurements highlighted the hysteretic effects relating to the magnetic memory of the resonators [78]. Advanced work on fractal resonators with fractal ground planes has led to extremely resilient resonators even in applied fields of  $\sim 200$  mT [79]. In addition to studies in static magnetic fields, the effects of rapid field changes demonstrated that it is possible to vary the centre frequency of a resonator quicker than the photon lifetime [80]. The ability to vary the centre frequency quickly allows for transfer of microwave states between storage elements [81], where rapidly moving the centre frequency of the resonator away from the storage element, a long lifetime can be realised. In fact tuning of the centre frequency can be so rapid as to allow amplification of vacuum states and has led to the observation of the dynamical Casimir effect [82]<sup>8</sup>.

## 5.1 Studies of noise in other systems

Interest in the low frequency noise properties of superconducting devices has existed for decades [83]. It is common to find flicker ( $1/f$ ) noise which scales as  $S = a/f^\alpha$  where  $\alpha=1$ . This process has been extensively studied in a variety of superconducting devices, including SQUIDs [84] [85] [86] [87], single electron transistors (SETs) [88] and superconducting qubits [89] [90] [91]. Several reviews cover the results and models which can give rise to flicker noise [92] [93] [94] [95], and more recently [24]. However, work in understanding and eliminating this noise process is still ongoing. For this section, the focus is to overview studies of the flicker noise dependence with another parameter, such as temperature or magnetic field. In early work it is hinted that flicker noise decreases with decreasing temperature [86], although it could have also been a material effect. Later work confirmed this temperature dependence [85]. A more systematic study of charge noise  $S_Q$ , found linear scaling with temperature in both SETs [96] and Josephson junctions [97]. Other measurements on qubits found noise scaling as temperature squared [98], though later results from the same group on SETs instead suggested a linear dependence which saturates at low temperatures [99]. Further measurements on flux qubits [100] and SETs [101] agreed on the linear dependence which saturates at low temperatures. Due to the links between

---

<sup>8</sup>The Dynamical Casimir effect is the creation of energy from the rapid movement of a mirror. This was realized with a SQUID which rapidly changed the electric length of a superconducting resonator.

Table 5: Overview of the flicker noise behaviour in various superconducting devices,  $S_Q$  denotes charge noise and  $S_\phi$  denotes flux noise

Device	Dominant noise type	Observed dependence
SET [96]	$S_Q$	$\propto T$
Josephson junction [97]	$S_Q$	$\propto T$
charge Qubit [98]	$S_Q$	$\propto T^2$ above 250 mK
SET [99]	$S_Q$	$\propto T$
flux Qubit [100]	$S_Q$	$\propto T$ above 200 mK
SET [101]	$S_Q$	$\propto T$ above 150 mK
Josephson junction [105]	$S_Q$	$\propto T$ above 200 mK
SQUID [103]	$S_\phi$	$\propto \frac{1}{T^\gamma}$
SQUID [104]	$S_\phi$	$\propto B$

flicker noise and decoherence [24], the observation of a low temperature saturation in charge noise has potential implications for the optimal temperature at which to operate a device. To combat the effects of charge noise, some devices use geometries with reduced sensitivity to charge noise. However, these devices still exhibit flux noise  $S_\phi$ , which shows 1/f like behaviour [102]. Interestingly recent studies of the flux noise find an inverse temperature scaling [103] in contrast to the linear scaling found for the charge noise. This inverse scaling suggests a spin-based origin, which is supported by the observation that the flux noise was found to scale linearly with applied field [104]. Table 5 overviews these studies of noise and the general behaviour found.

## 5.2 Studies of noise in Superconducting resonators

The existence of excess noise in superconducting kinetic inductance detectors was identified in the initial work of Day et al. [1] and is covered in the thesis of Mazin [15]. This work consisted of a homodyne setup using a mixer. Although details of the sampling duration and rate are not presented, this measurement showed a  $S_\theta \propto 1/f^{0.5}$  dependence. This dependence was also found in a 220 nm Al on Si,  $\nu_0=4.35$  GHz,  $Q_L=3.5 \times 10^5$  resonator at  $T=120$  mK with  $P_{circ}=-30$  dBm [65]. Again, a homodyne setup was used although the two signal quadratures were individually studied. Here the signal quadratures were digitised for 10 second windows at a rate of 250 kHz. By reconstructing the quadratures (to the amplitude and phase response) this work was able to demonstrate the amplitude noise to

be negligible. In relation to TLFs this experiment explored the dependence on microwave drive and found a scaling as  $P_{app}^{-0.5}$ .

In parallel work by Baselmans et al. a similar  $S_\theta \propto 1/f^{0.5}$  dependence was observed [67], again using a homodyne technique. This work featured several Ta resonators on intrinsic Si, with  $\nu_0$  between 3-3.3 GHz and  $Q_L$  between  $1.9\text{--}16 \times 10^4$ . The observed noise was lower than that featured in Gao et al. [65] although the difference was attributed to higher drive powers. In comparative work, the Si substrate was replaced with Sapphire and shown to reduce the noise level [42]. This work also suggested a link between the microwave absorption in dielectrics due to TLFs and properties of the resonator. The effects of TLFs were later shown to affect the quality factor [14] and resonant frequency [45] [37].

The first comprehensive study to measure the temperature dependence of noise in resonators was performed by Kumar et al. [106]. Here, the measurements shown previously by Gao et al [65] were repeated for many temperatures and microwave drives. Again a general  $S_\theta \propto 1/f^{0.5}$  was observed, and the noise of the phase channel between 200-300 Hz was extracted in varying microwave drive and temperature. A general dependence given by  $S_y = AP_{app}^{-0.46}T^{-0.14} \tanh^2(h\nu_0/2k_B T)$  was obtained, implying a  $1/\sqrt{P_{app}}$  and weak temperature dependences. The tanh term was motivated by the TLF model but measurements could not verify its validity. Additionally the results implied no relation between the temperature and power effects, i.e. the behaviour with applied power shows no temperature dependence itself. A follow up noise modelling paper by Gao et al. [107] provided justification for the observed  $1/\sqrt{P_{app}}$  dependence. The paper also found a strong dependence on the width of the CPW (Coplanar Waveguide), which suggests that if TLFs are the source of excess noise, then they should be located at the interfaces, rather than in the bulk. Further details on these measurements can be found in the thesis by Gao [18].

The next studies of noise in superconducting resonators come from a series of papers by Barends et al. [43] [108] [109] [71]. These further tested the hypothesis of noise being due to TLFs located at interfaces. It involved the comparison of noise between bare resonators and those covered by an additional  $\text{SiO}_x$  layer. The results found noise to be 7 dB ( $\sim 4$  times) higher for resonators covered by the additional dielectric. More importantly there was no observed dependence on the height of the dielectric [43]. A dependence on choice

and treatment of dielectric materials was found when hydrogen passivation of the silicon surface led to decreased noise [109]. The final paper in this series [71] examines the effect of removing dielectric from regions of high electric field, and found the noise was reduced. This effect is additive to widening the CPW producing a cumulative benefit. These results are interpreted as the presence of  $SiO_x$  dominating contributions to noise.

To summarise the existing studies of noise in superconducting resonators had all involved the use of a homodyne detection scheme. In general the observed dependence has been a  $S_y \propto f^{-0.5}$  which is not the expected noise process from TLFs. It is possible that the reason for this is the insufficient measurement time which resulted in tracing the autocorrelation function rather than the underlying noise shape<sup>9</sup>. A further possibility is the incorrect conversion from the measured phase jitter to frequency spectra. Strong evidence for this is the apparent observation of noise levels comparable with frequency standards [8], as well as the confusing use of the term phase noise [65]. More importantly these results are not in agreement with the nature of TLFs [7].

### 5.3 Studies of noise in hybrid systems

Following the overview of noise studies in superconducting resonators and other superconducting devices, the attention shifts to hybrid systems, where some quantum device is coupled to a resonator. In general this follows one of two routes, either phase noise measurements are performed on parametric amplifiers relative to the noise temperature of a HEMT amplifier, or flux noise measurements are performed on a Josephson junction type element within a resonator.

The behaviour of  $1/f$  flux noise in the single photon limit was studied by Murch et al. [110]. Here Josephson junctions were embedded in a variety of superconducting resonator geometries and homodyne noise measurements were performed. These measurements found a  $S_y \propto 1/f$  dependence attributed to the presence of Josephson junctions. A noise scaling

---

<sup>9</sup>The autocorrelation function possesses a numerical pole at zero since this term is defined as being in perfect correlation. This underlying correlation decays through the function and means a short measurement can be influenced by this underlying decay in the autocorrelation function itself. Recent measurements [110] [?] with homodyne systems that measured superconducting resonators for much longer time spans were able to observe the true  $1/f$  process in the resonator, this validates the possibility that the  $S_y \propto f^{-0.5}$  was a measurement artefact.

Table 6: Overview of frequency stability for various frequency standards.

Type	Stability	$h_0$	$S_y$	$S_\theta$	Time
SRS PRS10 [111]	$<2 \times 10^{-11}$	$8 \times 10^{-22}$	$8 \times 10^{-22}/\text{Hz}$	-71 dBc/Hz	1 s
	$<1 \times 10^{-11}$	$2 \times 10^{-23}$	$2 \times 10^{-23}/\text{Hz}$	-87 dBc/Hz	10 s
Hydrogen MASER [112]	$<2 \times 10^{-13}$	$8 \times 10^{-26}$	$8 \times 10^{-26}/\text{Hz}$	-91 dBc/Hz	1 s
	$8 \times 10^{-14}$	$1.3 \times 10^{-27}$	$1.3 \times 10^{-27}/\text{Hz}$	-109 dBc/Hz	10 s
Sapphire oscillators [113]	$7 \times 10^{-15}$	$9.8 \times 10^{-29}$	$9.8 \times 10^{-29}/\text{Hz}$	-83 dBc/Hz	1 s
	$<5 \times 10^{-15}$	$5 \times 10^{-30}$	$5 \times 10^{-30}/\text{Hz}$	-94 dBc/Hz	10 s

linear with temperature was observed, although much sample-to-sample variation existed. The paper concluded the observed noise was dominated by the resonator, however, the observed noise shape and temperature dependence did not agree with previous studies [106].

On the basis that readout is limited by the noise contribution of the cryogenic HEMT amplifiers [114] there have been numerous efforts towards ultra low noise parametric amplifiers [11, 115–119]. The base comparison for all these methods is to compare the noise temperature (or equivalently noise figure) of the parametric amplifier to the HEMT. A state of the art HEMT amplifier can obtain a noise temperature as low as 2.6 K [120] (across the band 4–8 GHz), although values reported in the literature are generally around 5 K. The noise figure relates the degradation of the signal-to-noise ratio corresponding to the thermal noise of a black body at the noise temperature  $T_N$ , at the signal chain input. While this definition is suitable for approximating the *white phase* noise of the amplifier (the  $b_0$  process in table 4) care is needed, as often this noise is not the dominating noise process over the timespan of a measurement. The noise temperature and noise figure can be used to calculate the  $b_0$  value of an amplifier by

$$b_0 = \frac{F_N k_B T_N}{P_{app}} \quad (5.1)$$

where  $F_N$  is the noise figure and  $P_{app}$  is the applied power in watts. From this value, one can then use table 4 to convert between  $S_\theta$ ,  $S_y$  and  $\sigma(\tau)$  for the white phase noise of an amplifier. This has been done for varying input powers in figure 5.1, where the value for

the noise temperature is derived from the Friis formula.<sup>10</sup> This plot shows the phase noise floor being given by  $b_0$  and highlights the  $1/P_{app}$  dependence. However, there are several things to consider here

- Firstly the overall stability appears to quickly approach the  $\sim 10^{-13}$  level at 1 s realised by an atomic fountain [112]
- The frequency spectrum reveals a divergent process, such a process is almost never seen in frequency spectra

These two points highlight the fact that often *other* noise processes dominate the noise contributions from a HEMT amplifier. In fact the noise temperature (or noise figure) do not sufficiently describe the noise as they neglect any low frequency processes. Due to this any comparison relative to the noise temperature is an insufficient comparison. Instead, the relative  $h_{-2}$ ,  $h_{-1}$  and  $h_0$  values for an amplifier chain should be extracted. Then measurements on parametric amplifiers should seek to prove that these  $h$  parameters become lower. In particular, the abundance of Josephson elements in many realisations of a parametric amplifier is likely to lead to large  $h_{-1}$  (flicker noise) contributions [102].

Table 6 contains stability measurements of various frequency standards. One should be cautious with any values in literature which report phase noise close to that obtainable by frequency standards. Not only have reports been published on resonators where this is true [8], but this also stresses the point that  $b_0$  does not sufficiently describe the noise from an amplifier. Primarily, this is because all standards are realisable with a large signal-to-noise ratio and hence do not need any amplification, unlike measurements on superconducting resonators. This lack of amplifiers and high signal-to noise-ratio results in no low frequency noise and also a minimal white noise contribution at 1 s.

## 5.4 Summary

This literature review has demonstrated the prevalence of a spectral noise  $\propto 1/f$  in charge sensitive superconducting devices. When looking at superconducting resonators a

---

<sup>10</sup>The Friis formula describes the addition of noise temperatures (or equivalently noise figures) for a chain of amplifiers. These scale as  $T_N = T_1 + \frac{T_2}{G_1} + \frac{T_3}{G_1 G_2}$ , where T is the noise temperature of the amplifier, G is the amplifiers gain and the number denotes the amplifiers position. The Friis formula highlights that the noise temperature is dominated by the first amplifier.

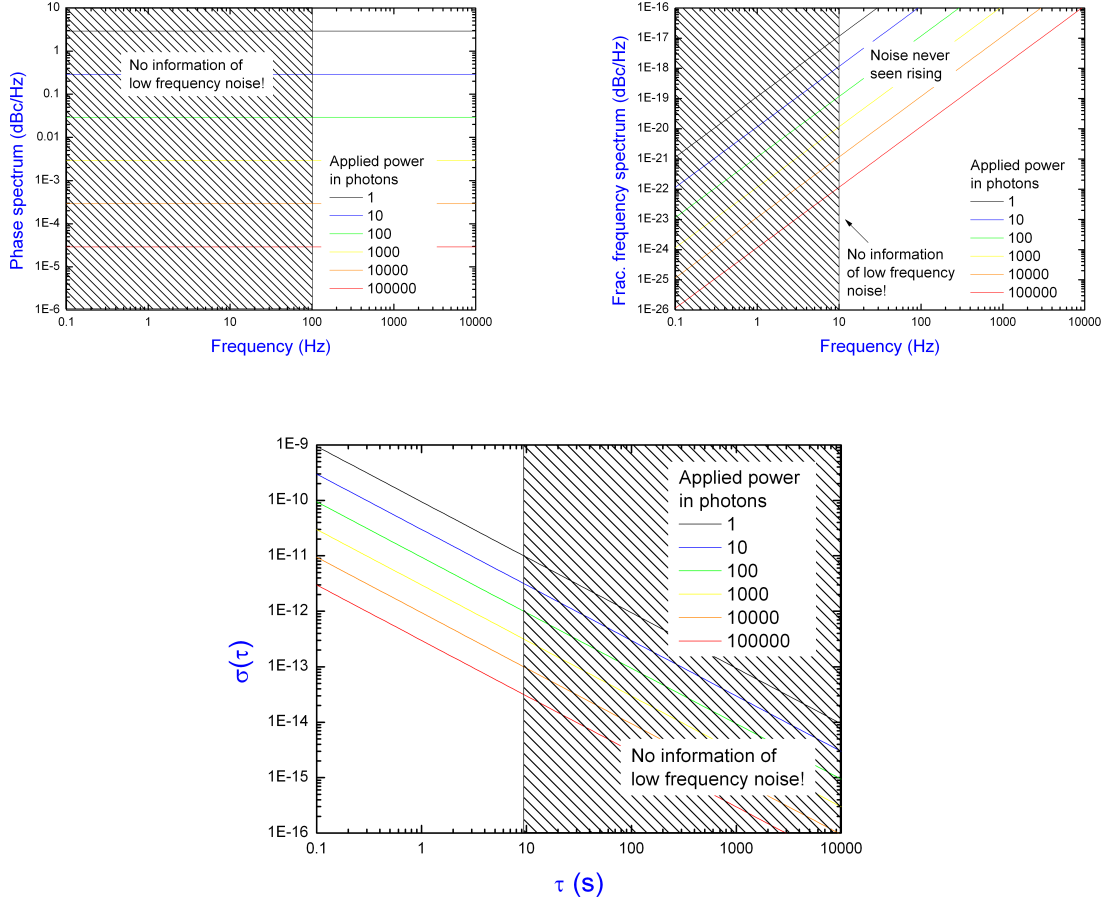


Figure 5.1: A plot showing the phase noise, fractional frequency noise and Allan deviation of a  $b_0$  limited amplifier under varying microwave drive. The microwave drive is referenced to an incoming number of 5 GHz photons, hence  $\langle 1 \rangle$  photon  $\approx$  -200 dBm. The assumed noise temperature is  $T_N=6$  K, which provides a noise figure of  $F = 0.2$ , these represent typical (rather than state of the art) values of an amplifier chain using the Friis formula Note the phase spectrum describes the noise as a flat noise floor, while the Allan deviation shows the noise to sharply reduce with time.

$1/f^{0.5}$  spectral noise has frequently been found instead. Charge sensitive devices observe the  $1/f$  spectral noise due to the existence of TLFs which exhibit telegraph noise. It follows that since there is strong evidence for TLFs within superconducting resonators, it is odd that the observed noise is not  $1/f$ . A potential reason for this, is that measurements of noise in superconducting resonators has only spanned short timescales (up to  $\sim 30$  s), which are not sufficiently long to observe  $1/f$ . An alternative possibility is that much of the analysis of resonator measurements was incorrect, or that some systematic effect has instead been

explored. Perhaps most importantly the present measurements have only explored the noise in superconducting resonators at relatively high microwave drives. This is suitable for detector based applications but not for QIP.

This thesis, focuses on a measurement technique able to observe noise processes at longer timescales. The previously observed  $S \propto 1/f^{0.5}$  dependence is interpreted as peculiar in that it is not a common noise process within any oscillator type system [58]. Further the homodyne detection scheme is heavily flawed when resolving slow noise processes, here systematic noise contributions are not neglected, and more advanced methods such as cross-correlation should be used. This measurements within this thesis begin by performing comparative noise measurements on superconducting resonators. The need to exhaustively check systematic noise contributions and correctly analyse noise processes is paramount. Table 7 compares many of these noise measurements with results obtained later in this thesis.

Table 7: Overview of noise measurements performed on superconducting resonators before the start of this thesis

Resonator materials	$\nu_0$ (GHz)	Q	T (mK)	$P_{circ}$ (dBm)	$f_L$	Sampling rate	Duration	Dominant noise <sup>a</sup>
Al on Si <sup>b</sup>	4.35	$3.5 \times 10^5$	-	-	$6.2 \times 10^3$	-	-	$S_\theta \propto 1/f^{0.5}$
Ta on Si <sup>c</sup>	3.07	$5.5 \times 10^4$	300	-33	$2.8 \times 10^4$	100 kHz	-	$S_\theta \propto 1/f^{0.5}$
Nb on Si <sup>d</sup>	4.35	$3.5 \times 10^5$	120	-41	$6.2 \times 10^3$	250 kHz	10 s	$S_\theta \propto 1/f^{0.5}$
Ta on Si <sup>e</sup>	6.0	$< 10^6$	310	-	$3 \times 10^3$	$> 100$ kHz	-	$S_\theta \propto 1/f^{0.25}$
NbTiN on Si <sup>f</sup>	4.47	$6.3 \times 10^5$	350	-30	$3.55 \times 10^3$	$> 100$ kHz	-	$S_y \propto 1/f^{0.4}$
Nb on Si <sup>g</sup>	4.35	$5^5$	120–1200	-30 to -50	$3.5 \times 10^3$	250 kHz	-	$S_y \propto 1/f^{0.5}$

<sup>a</sup>Irrespective of the subscript  $a$  in  $S_a$  the spectrum is always the *frequency* spectrum due to the sampling rate always being below the Leeson frequency.

<sup>b</sup>Data from Day et al. [1]

<sup>c</sup>Data from Baselmans et al. [67]

<sup>d</sup>Data from Gao et al. [65]

<sup>e</sup>Data from Barends et al. [43]

<sup>f</sup>Data from Barends et al. [43] [109] [71]

<sup>g</sup>Data from Kumar et al. [106]

# Chapter 6: Measurement setup

This section describes various details of the measurement setup, including the microwave setup and equipment realise the Pound measurement technique. The characterisation of this setup, and measurement of the system noise floor will be covered in the next section in measurements of the dielectric resonator.

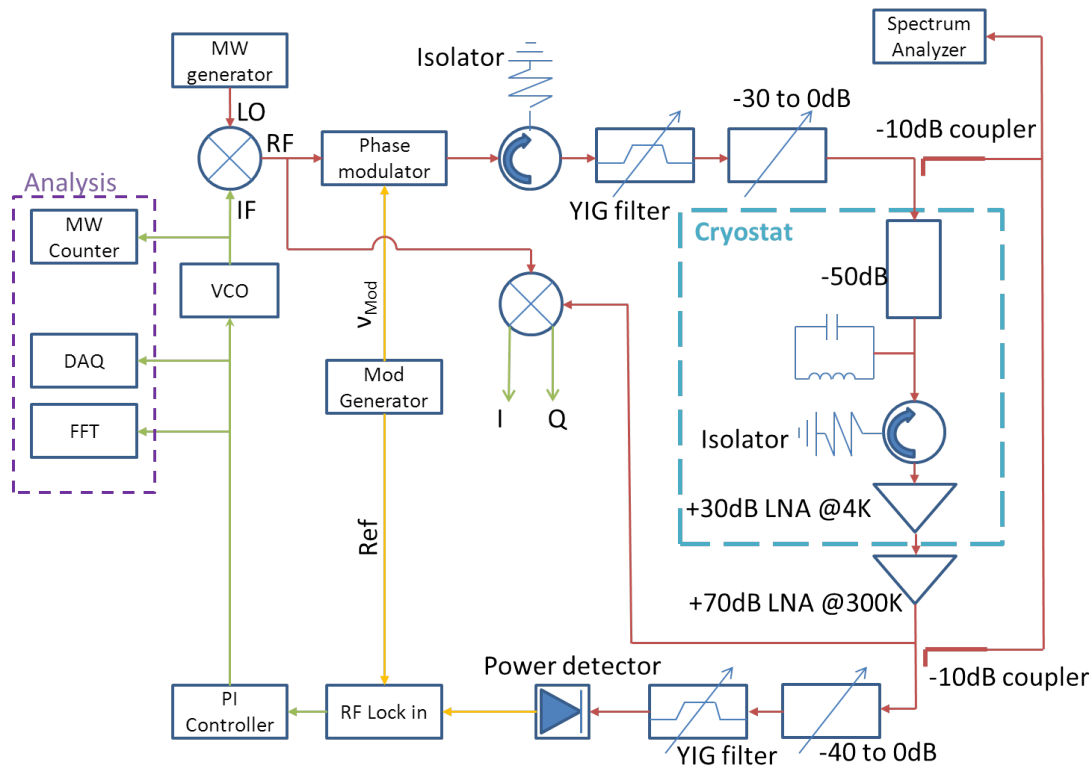


Figure 6.1: A schematic of the real Pound detection scheme used in this project. Shown are signals at RF (red), 1 MHz (yellow) and DC (green). The input and output power can be varied, allowing varying microwave drive at the resonator while maintaining constant power at the diode. An additional generator is used to create an up-mixed input signal, providing benefits of low phase noise source compared to using the microwave synthesizer as a VCO. This setup allows high frequency resolution using microwave counters however tunable YIG filters are required to control the input signal and prevent saturation of the diode. The LNA located at 4K is a low noise cryogenic HEMT amplifier. In this setup the generator, VCO and counter are all referenced to the 10 MHz source derived from a hydrogen MASER.

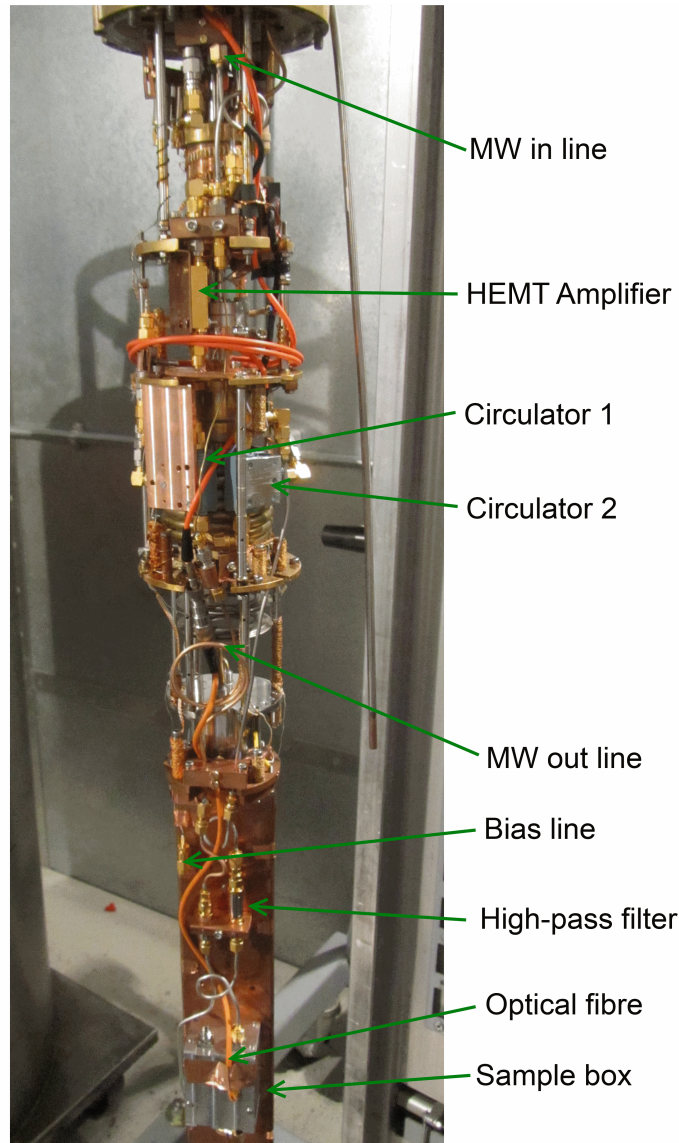


Figure 6.2: A photo of the dilution refrigerator. Labels point to the various temperature stages of the dilution refrigerator. Additionally a low noise cryogenic amplifier, circulator and optical fibre are shown.

## 6.1 Microwave setup

All measurements begin with an Anritsu 3767C vector network analyser (VNA) to diagnose the microwave lines and find any resonance curves. The microwave connection on the inside of the cryostat is photographed in figures 6.2 and 6.3, and is detailed in the schematic of figure 6.6. After the VNA has traced a resonance curve the Pound loop can

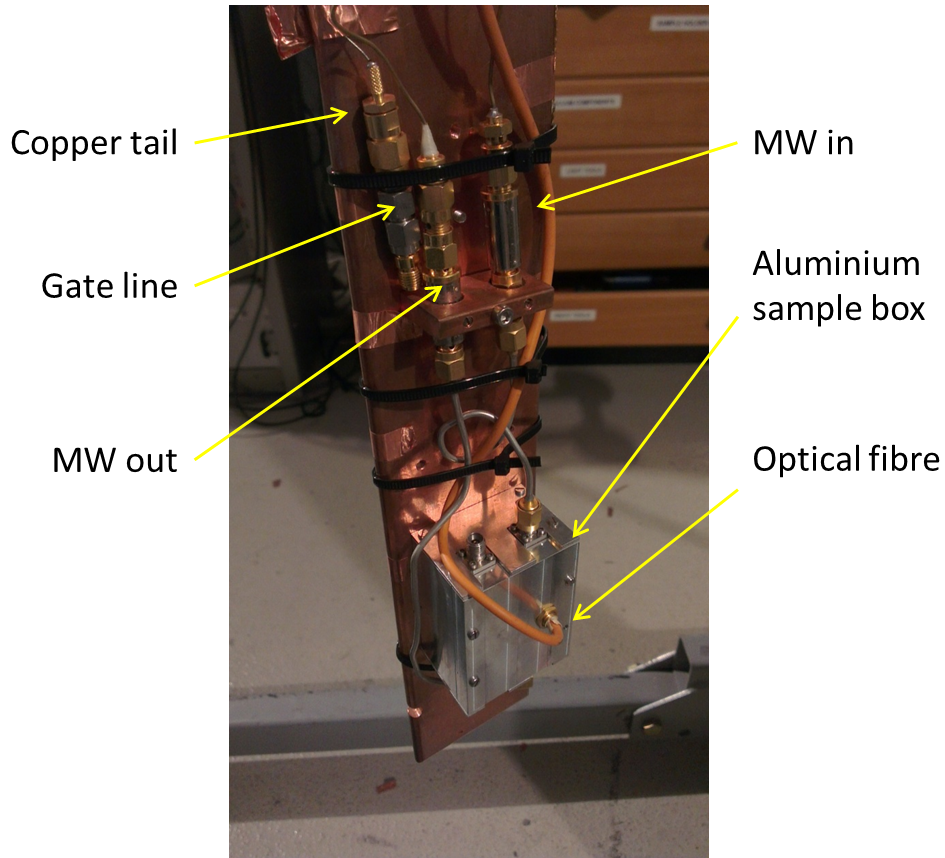


Figure 6.3: A photo of the dilution refrigerator tail with an aluminium sample box that was used for most of the measurements with superconducting resonators. The photo shows the two microwave lines, a low frequency gate line and an orange optical fibre.

then be set to track that resonance.

The components which form the Pound setup show in figure 6.1 are described as follows. The initial microwave frequency signal is formed by an Anritsu 69253A synthesizer, which drives the LO port of a single side band mixer. The IF port is driven at 15 MHz by an Agilent 33522A arbitrary waveform generator, which also acts as the voltage controlled oscillator (VCO), which changes its output frequency based on the input voltage it is driven by. The upper side-band from the RF port is the carrier signal and is nominally chosen to be at the resonant frequency as was determined using the VNA. A 1 MHz signal is generated using a Novatech 409B signal generator to drive a Hittite HMC538LP4 phase shifter to provide phase modulation of the carrier. A YIG bandpass filter is used to reject the lower side-band from the input mixer and a tunable attenuator is used to

allow the input power to be varied. Measurement of the input power is performed by a HP 8593E spectrum analyser. Figure 6.4 shows an optical-breadboard that is clamped to the cryostat frame for mechanical support. Housing the RF setup in this way damps any vibration induced phase fluctuations.

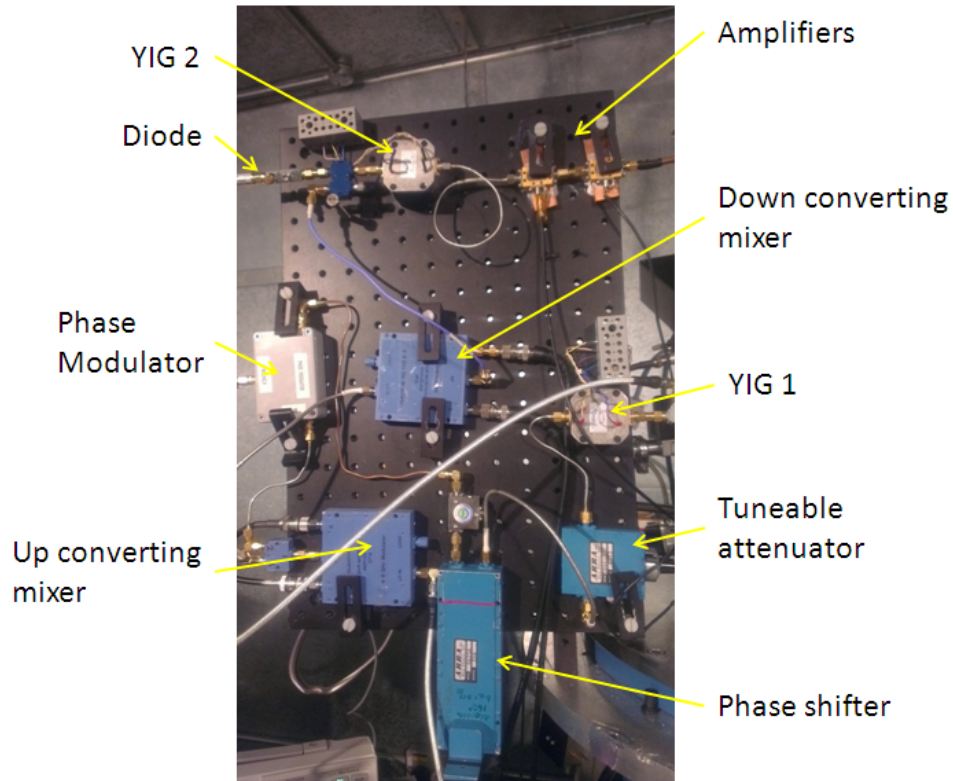


Figure 6.4: A photo of the microwave setup mounted on an optical breadboard which is clamped to the cryostat for vibration isolation. Shown is an up converting single side-band mixer, phase modulator, phase shifter, tuneable attenuator and YIG filter on the microwave input. On the top are two room temperature amplifiers, a second tuneable YIG filter, power splitter and the diode on the microwave outline.

The output signal from the cryostat undergoes amplification from 4 amplifiers before passing through a second YIG filter and another tuneable attenuator. These are used to reduce the levels of wideband noise from the amplifier chain. An Atlantec ATD-040080 tunnel diode detector is used to rectify the phase modulated signal and generate the Pound error signal. The diode output voltage is fed into a Stanford Research Systems SR844 RF lock-in amplifier, which is also receiving a reference signal from the Novatech 409B. The

lock-in provides narrow-band detection of the small diode voltage, which is fed into a Stanford research systems SIM960 PID controller within a SIM900 mainframe. An Agilent DSO7014A oscilloscope reads both the lock in output and PID output to form the Pound error signal. Viewing the error signal allows the error signal gradient to be optimised, which is essential when operating at low microwave drive. The PID output then drives the VCO to complete the Pound setup.

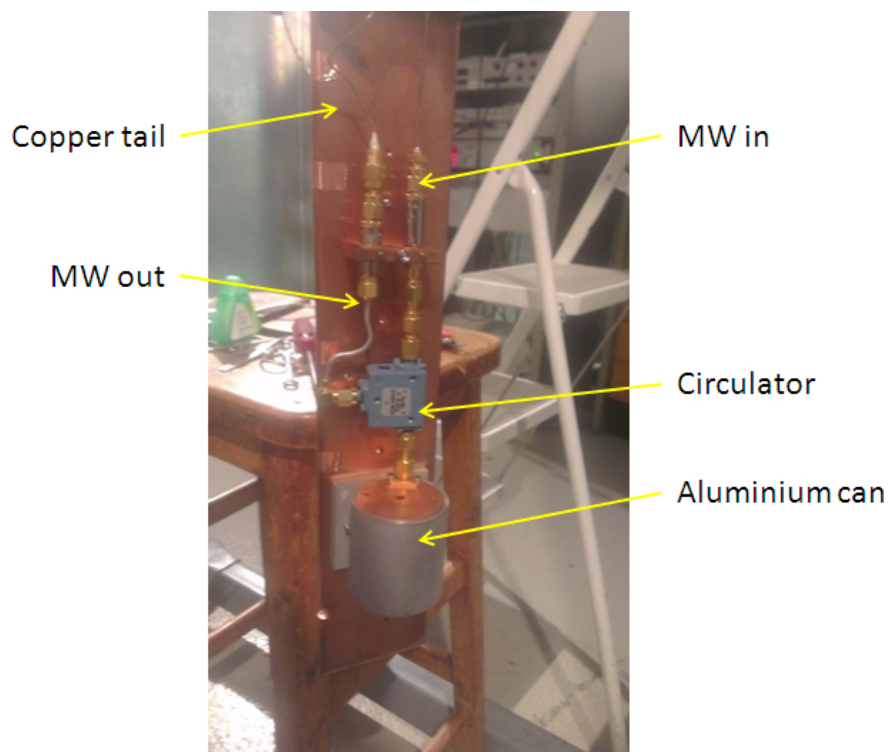


Figure 6.5: A photo of the dilution refrigerator tail with an aluminium can sample holder used for the dielectric resonator. The photo shows the two microwave lines, with a circulator mounted on the input port to the aluminium can.

An Agilent 3523A frequency counter is used to read the IF frequency. Further analysis is then performed based on this frequency measurement. Alternatively the PID voltage can be sampled with a National Instruments DAQpad-6015 analogue to digital converter. The frequency counter is preferred as it can perform measurements with no dead time over any sampling period, by contrast the DAQpad only performs an instantaneous measurement at the sampling interval. This is problematic as a large dead-time can exist between individual

measurements. Analysis of a stream of instantaneous measurements with dead time is not trivial and makes it difficult to draw accurate conclusions from the data.

## 6.2 Cryogenic setup

The cryogenic setup consists of a dilution refrigerator for obtaining temperatures as low as 50 mK. The operation of a dilution refrigerator can be found in the book by White and Meeson [121]. Figure 6.2 details the general cryogenic setup. An aluminium sample box is used to house the superconducting resonator. There are also copper enclosures which may be substituted for the aluminium sample box, this is mainly to allow for small magnetic fields to be applied to the sample. Such copper enclosures have not been used heavily in this thesis and so the aluminium sample box is considered as the default measurement setup. Figure 6.5 is applicable for the measurements of the dielectric resonator. The rest of the cryogenic setup shown in figure 6.6 is the same for all measurements.

Figure 6.6 shows the microwave in-line undergoing 3 stages of attenuation which total to 50 dB. This attenuation cools the incoming black body radiation of the microwave signal and consists of XMA attenuators. Each subsequent attenuation stage is placed at a lower temperature to thermalise the coaxial lines. The input coax consists of copper-beryllium from 300 K to 4 K, stainless steel from 4 K to 1 K, brass from 1 K to the mixing chamber, and copper from the mixing chamber to the sample. These materials minimise the heat load of the coax while optimising the microwave transmission. The final performance is near that of superconducting NbTi coax, but is more robust due to soldered rather than crimped connections.

Copper rods thermally anchor the sample to a copper cold finger, which itself is clamped to the mixing chamber. The microwave signal passes through 3.5 GHz high pass filters before and after the sample box. The output signal passes through a circulator before being amplified by a cryogenic low noise amplifier with a noise temperature,  $T_N=5$  K and gain of 28 dB. After the amplifier, there is a 3 dB attenuator at 4 K for thermalising the coaxial line before it leaves the refrigerator. Thermally the sample looks out to the aluminium box which acts as a 50 mK black body, this looks out to the radiation shield which acts as a 200 mK black body. This reduces the number of 4 K photons (from the inside of the IVC)

that are able to interfere with the sample. Magnetic shielding of the sample begins with a double layer of mu-metal outside the cryostat. Then a superconducting lead cylinder surrounds the IVC and finally the aluminium sample box is also superconducting. This “freezes” the now reduced magnetic field.

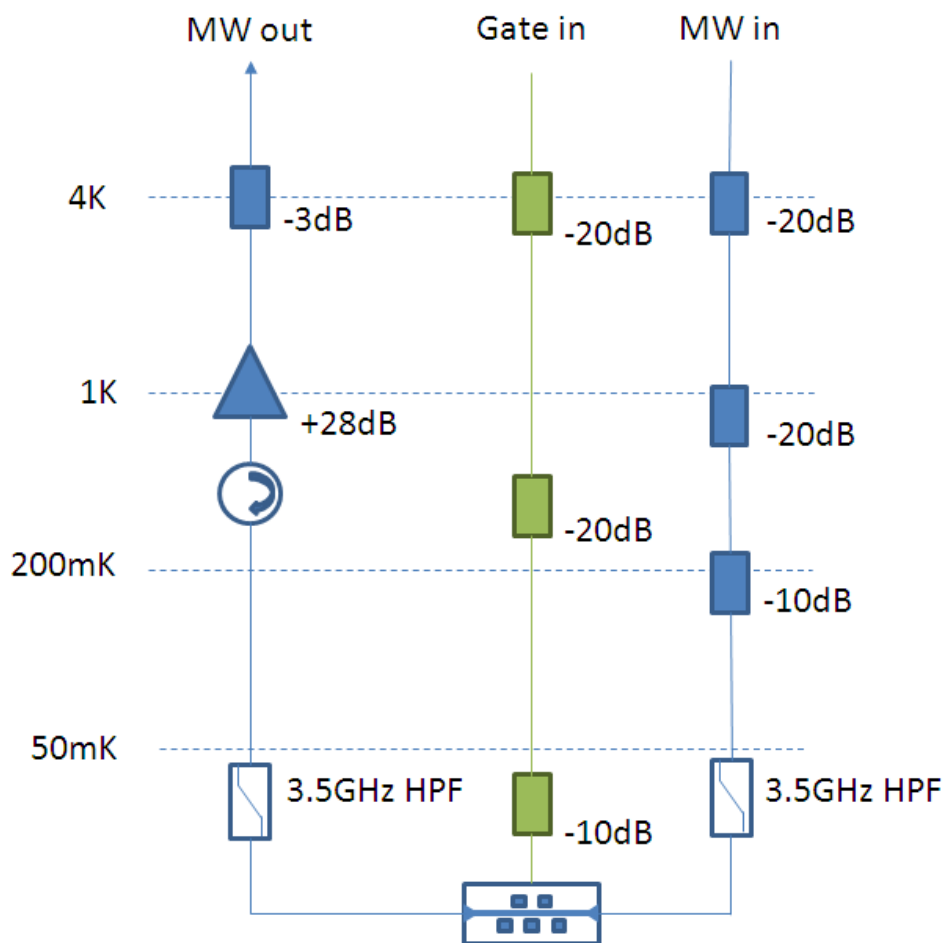


Figure 6.6: A Schematic of the cryogenic setup, showing three lines, which reach the sample at the mixing chamber. The microwave in-line consists of high frequency coax with 50 dB of attenuation and a 3.5 GHz high pass filter. The microwave out-line consists of high frequency coax with a 3 dB attenuator, a 3.5 GHz high pass filter, cryogenic amplifier and circulator. Shown in green is the gate line which consists of low frequency coax and contains 50 dB attenuation. This line is suitable for applying a low frequency voltage bias to gate elements on some samples.

# Chapter 7: Characterizing the loop

This section covers the experiments which characterised the loop itself. This involved a dielectric resonator which was used to determine the system noise floor. This chapter expands on the Reviews of Scientific Instruments paper by Lindström et al [122].

## 7.1 The resonator

The dielectric resonator was made from high purity sapphire. This is formed into an  $r = 8$  mm puck stood atop an 8 mm column. The resonator was clamped to a copper plate which formed the lid of a 30 mm wide aluminium can. The copper plate had an SMA bulkhead connector on the outside where the central conductor formed a small loop inside the can. This setup is shown in figure 6.5, where the microwave setup includes a circulator on the mixing chamber. The resonator was then interrogated by measuring the reflected response using the circulator.

Coupling to the resonator was controlled by the size of the loop within the central conductor and how far into the can it extended. Although a dielectric resonator can operate at room temperature, this results in a coupling limited quality factor after cooling. Therefore, the resonator was setup to be very under coupled at room temperature, then as the temperature decreases the conductivity of the aluminium increases resulting a better coupling when cold.

The magnitude response of the dielectric resonator at 100 mK is shown in figure 7.1. This resonance exhibits a quality factor of  $\approx 100000$  and the resonance dip is  $\sim 3.1$  dB, which corresponds to near critical coupling.

## 7.2 Jitter studies and determining the system noise floor

A dielectric resonator was chosen to characterise the Pound loop for a few reasons.

- Dielectric resonators are a well studied system that can produce a  $\sim$ GHz resonance with high quality factors.
- Dielectric resonators are ultra stable and are an alternative approach to a frequency standard [113]

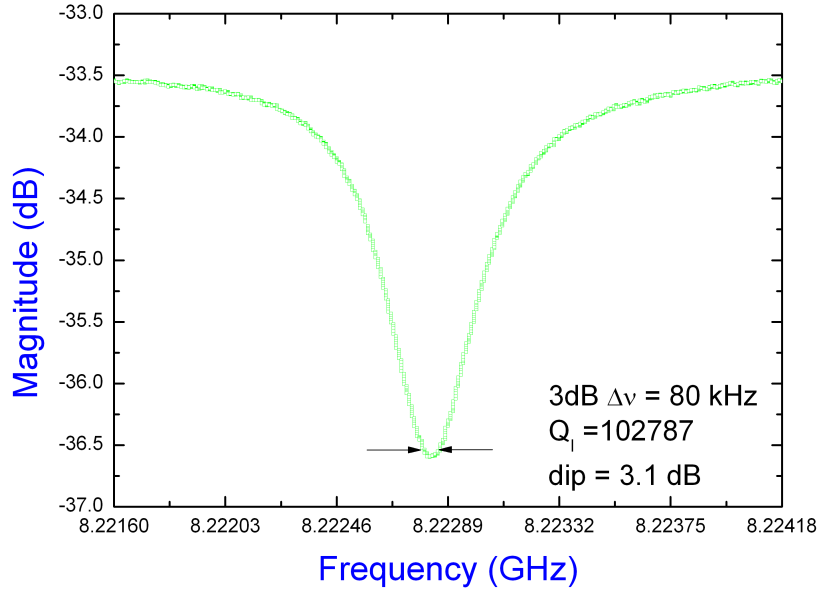


Figure 7.1: A plot showing the measured magnitude response of the dielectric resonator at 100 mK. The resonance dips by  $\sim 3.1$  dB which corresponds to near critical coupling with a quality factor of  $\approx 10^5$ .

- Dielectric resonators noise processes are well understood and commonly do not exhibit  $1/f$  type noise [123]

These reasons made the dielectric resonator both a suitable alternative to use within the dilution fridge with only small modifications required and a good candidate to examine the noise floor of the system. This is due to the electronics, amplifiers and mixers all being well known for exhibiting noise at low frequencies. If the Pound setup attempts to stabilise a perfect noise free system, it will become limited by its own noise processes. Hence, if the dielectric resonator displays no  $1/f$  noise then it is suitable for estimating the  $1/f$  noise floor of the loop.

Figure 7.2 shows the intrinsic jitter of the dielectric resonator in terms of fractional frequency analysed using the Allan variance. Although it is more conventional to use the Allan deviation (square root of the variance) to characterise the fractional frequency jitter, it is preferable to use the Allan variance to extract h parameters as explained in table 4. This figure shows frequency resolution is limited at short time scales by a white

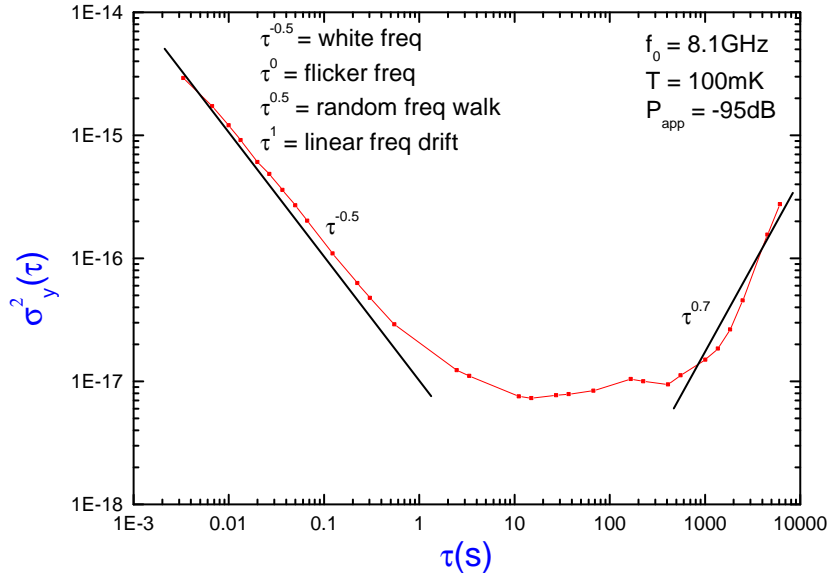


Figure 7.2: A plot showing the calculated fractional frequency stability of the dielectric resonator with an applied power of -95 dBm at 100 mK. Power law noise processes are displayed, and this trace shows white frequency noise, flicker frequency noise and a linear frequency drift.

frequency process. Here the resolution improves as the measurement time is increased, this implies the noise process is frequency independent. In the long time limit a rapid drift is shown, this is due to either temperature instability or vibration of the dilution fridge. A temperature instability produces a frequency instability in the resonator, while vibrations result in a time varying coupling to the resonator. Of more interest is the noise floor which occurs between 10 and 300 seconds, here the dominant noise process is flicker frequency noise. For the reasons outlined above this is expected to be the noise floor of the mixer/amplifier chain and is important for future measurements.

By repeating the stability analysis for many microwave powers, power dependence of the flicker noise floor can be examined as shown in figure 7.3. The plot highlights a very weak power dependence which is expected of amplifiers [58]. It also verifies the assumption that stability measurements of the dielectric resonator become limited by jitter originating within the loop. The second y-axis contains the calculated phase noise which corresponds to the measured noise floor. The first thing to notice with this phase noise is that it is

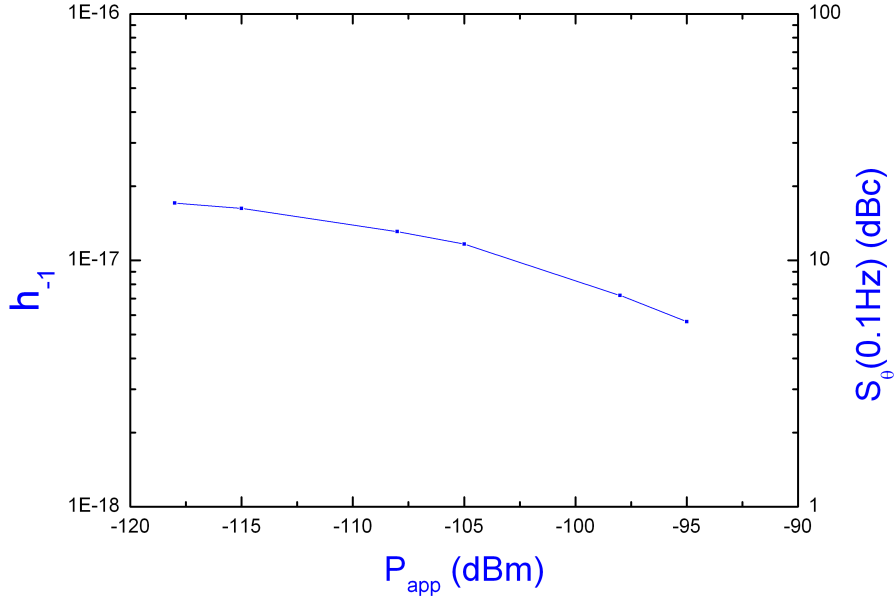


Figure 7.3: A plot showing the measured  $h_{-1}$  parameter for varying input microwave powers, this describes the flicker noise floor by  $S_y = h_{-1}/f$ . This value is determined by repeating the stability analysis shown in figure 7.2 for varying microwave powers, then extracting the h parameters as explained in table 4. The right y-axis shows the calculated phase noise based upon the h parameter.

very high, in fact  $\sim 100$  dBc higher than the values reported in table 6. However, this is not surprising as those measurements were “white” rather than flicker limited. The reason for this is that the microwave power is much higher, this means there is no need for amplification, which would drastically increase the phase noise. In fact the typical best values of amplifier phase noise at low offset frequencies are typically -20 dBc [58]. When comparing to this value the phase noise shown in figure 7.3 the difference is likely to be attributable to the difference in applied power. This highlights that caution is required when examining literature which show measurements at ultra low microwave powers with a phase noise comparable to, or apparently better than, the frequency reference.

### 7.3 Optimizing the loop

In general, a Pound type of feedback is used where the signals strength is very high, and often there is no need for any amplification. The excellent signal to noise ratio makes

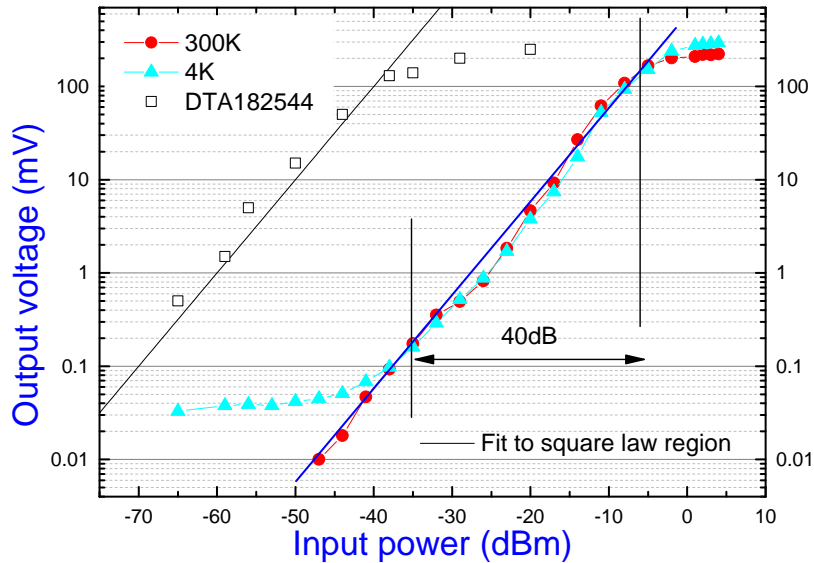


Figure 7.4: A plot showing the measured diode sensitivity. The diode output voltage was measured when driven by a phase modulated carrier for many powers. The black line shows the square law region, where the diode is rectifying the input signal. Shown in red (blue) are room temperature (4 K) measurements performed on the Atlantec ATD-040080 tunnel diode detector. For comparison data from the data sheet of a Herotek DTA182544 tunnel diode with integral pre amplifier is shown.

the requirements on the diode and lock-in amplifier very low. Here, the setup consists of 4 amplifiers due to the very low microwave powers being used. Due to the wide-band nature of the amplifier and the equally wide-band sensitivity of the diode some checks are required to ensure the diode is driven optimally.

Initially the signal output of the diode needs to be measured for various input microwave drives. For this measurement, the phase modulated carrier signal is applied to the diode itself. However, to represent the experiment the phase modulator needs to be biased such that the first side bands contain more power than the carrier. This then accurately reflects the real reflected signal where the carrier has a reduced amplitude due to the resonance dip. The weakly coupled port of a 10 dB coupler was used to feed a spectrum analyser, this then measured the microwave power. The output voltage of the Atlantec ATD-040080 diode was measured at both room temperature and at 4 K, as shown in figure 7.4. A

minimum detection power of  $\sim -53$  dBm is found, which agrees with the specifications.

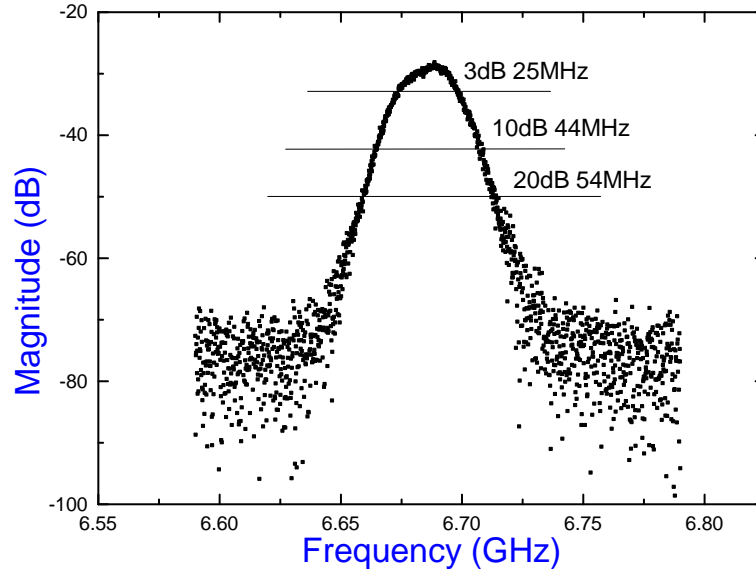


Figure 7.5: A plot showing the measured transmission through the YIG filter. The filter is used to very heavily attenuate any signals outside of a  $\sim 100$  MHz pass band.

In general, measurements are performed at  $-25$  dBm at the diode, which as figure 7.4 shows is well below the diode saturation power. Although a higher power could be used, the use of a lower value increases the effective dynamic range of the experiment. This is due to all measurements being performed with the same applied power at the diode, which is achieved by the use of a tunable attenuator. However, since the gain of the loop is fixed for a given amplifier chain, the minimum detectable power relates to minimal attenuation before the diode and an input power low enough to see the diode driven at  $-25$  dBm.

Importantly, one cannot simply add another amplifier to increase the dynamic range as this will change the flicker noise floor of the amplifier chain. The reason for this is that the flicker noise is additive [58], so it becomes worse with each additional amplifier. By comparison, the white frequency noise obeys the Friis formula, which means additional amplifiers add negligible white noise. As such if the amplifier chain was changed, then the

characterisation of the system noise floor would need to be repeated.

To improve the stability at low microwave drives, a YIG tunable bandpass filters is used. This is due to the diode being sensitive to a wide band of frequencies. When operating at low microwave powers, the attenuation before the diode is minimal, this can lead to the diode being saturated by wide band noise rather than a strong input signal. As a result, the diode cannot be driven optimally, leading to much reduced loop performance. To counter this YIG tunable bandpass filters are used to reduce the amplified wideband noise. Figure 7.5 shows the transmission through such a filter. Thus, the diode is only able to see a  $\sim 100$  MHz band about the carrier, rather than a 4 GHz band due to the amplifiers. Using a YIG allows the diode to be driven closer to its optimal performance over a wide range of microwave powers into the cryostat. Later measurements will span the power range of  $\sim -135$  to  $-90$  dBm, allowing the few photon regime to be reached in some samples. The earlier Pound schematic shown in figure 6.1 is that of the fully optimised loop following the improvements from the YIG filters.

# Chapter 8: Identifying noise processes in superconducting resonators

This section overviews measurements performed on superconducting resonators. The goal of these measurements is to examine the Pound technique's suitability to measure the intrinsic jitter of superconducting resonators. As covered in the Literature review, the measurements are to examine the noise processes present in superconducting resonators, and verify whether the flicker noise process exists. It builds upon the description of the loop behaviour and a calibration of the system noise floor in the previous section. The noise contributions of superconducting resonators are measured under varying drive conditions. The noise processes are expected to be due to the presence of TLFs in the dielectric. As such, the relevant parameters are the microwave drive, temperature, and the density of TLFs. The density of TLFs is varied by use of an additional dielectric layer on some of the resonators.

## 8.1 Description of the samples

Figure 8.1 shows three photographs demonstrating the PCB (Printed Circuit Board) and chip layout used for the majority of this project. The PCB sits inside the aluminium sample box shown in figures 6.2 and 6.3. This PCB has been metallised with gold and patterned into ground planes with a  $50 \Omega$  transmission line. Midwest microwave launchers are used to connect the transmission line to an SMA adapter. The holes within the ground-plane are used to suppress standing modes on the PCB, these could otherwise interfere with the resonators, and provide parallel conduction paths which lead to asymmetry in the resonance.

A typical sample chip is also shown in figure 8.1, the chip is 5 mm x 10 mm and also consists of a  $50 \Omega$ ,  $25 \mu\text{m}$  wide transmission line. The Transmission line broadens to  $\sim 300 \mu\text{m}$  for the so called contact triangle, this allow for bond wires to connect the chip to the PCB transmission line. Additionally the chip's ground-plane is heavily bonded to PCB ground. Within the ground-plane, lumped element resonators are placed surrounding the

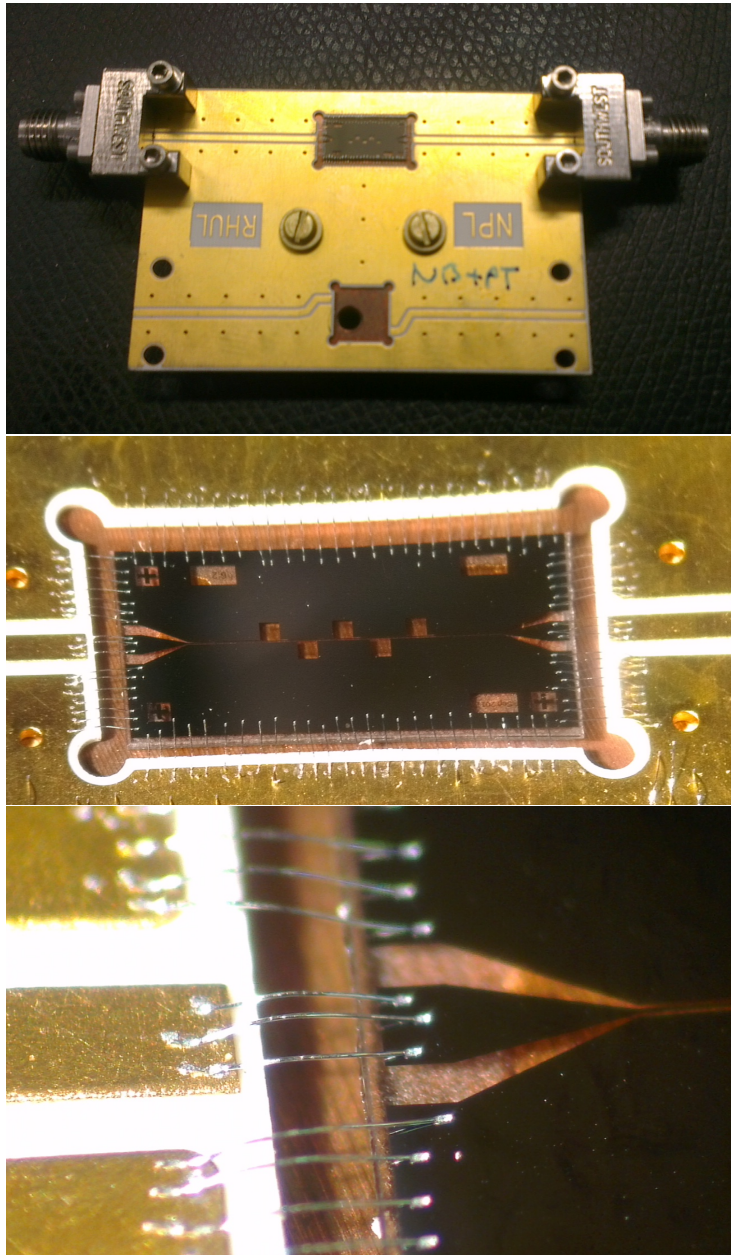


Figure 8.1: Top, a photo of the PCB (Printed Circuit Board) used for the majority of measurements. PCB is metallised with gold and formed into two coplanar transmission lines with an impedance of  $50 \Omega$  between 4-8 GHz. Middle, a photo of the general chip geometry used for the majority of measurements. Chip is 5 mm x 10 mm also consisting of a coplanar transmission line. Bottom, a photo zooming in on the contact triangle of the chip's transmission line, this region is used for accepting bond wires from the PCB.

transmission line. The holes for these resonators are  $300 \mu\text{m} \times 300 \mu\text{m}$  and are typically placed between  $10\text{-}30 \mu\text{m}$  from the transmission line.

Generally, five resonators exist on a chip, their typical appearance is shown in figure 8.2. This consists of a  $4\ \mu\text{m}$  wide inductive meander close to the transmission line and an inter-digitated capacitor. The inductive meander is kept at a constant size to keep the coupling relatively constant for all resonators on the same chip. This coupling can then be varied by changing the distance between the transmission line and the inductive meander. The resonant frequency was varied by changing the size of the inter-digitated capacitor. Resonant frequencies were chosen to be within the 4-8 GHz pass band of the microwave setup.

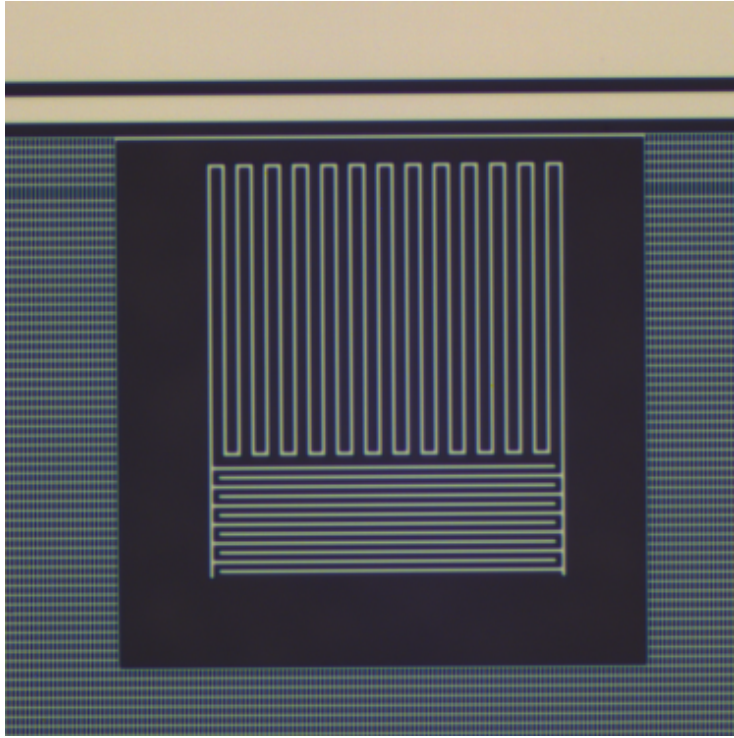


Figure 8.2: An optical picture of a lumped element resonator. Picture highlights the typical geometry consisting of an inductive meander (close to the transmission line) and an inter-digitated capacitor. In this picture the surrounding ground plane contains holes to trap magnetic flux, this feature is not present on all resonators.

The samples measured in this section consist of a sputter-deposited niobium layer on r-plane sapphire. These samples were patterned from Nb films deposited by Star Cryoelectronics. These were patterned using the recipe located in Appendix B. Other samples

come from NTT Basic Research labs and include the addition of a dielectric layer on top of the resonators. Figure 8.7 shows the appearance of the dielectric coating. The additional dielectric is either HfO or Al<sub>2</sub>O<sub>3</sub> and is deposited by atomic layer deposition (ALD). The location of the dielectric layer is focused on the inter-digitated capacitors where the electric field is maximal. Here, any TLFs within the dielectric will couple strongest to the resonator. The effect of TLFs in varying locations is studied by comparing the effect of the substrate-superconductor interface and the superconductor-surface interface which has an additional 50 nm of deposited dielectric.

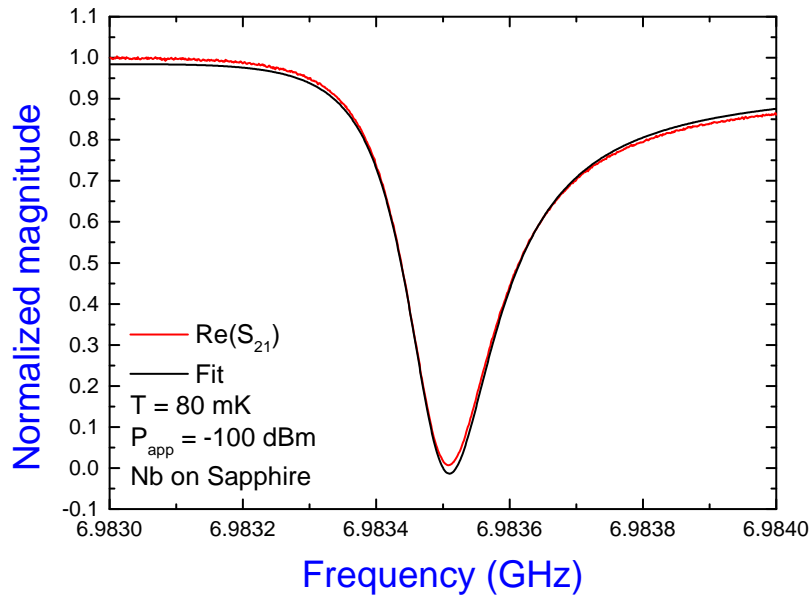


Figure 8.3: A plot showing the measured magnitude response of the 6,98 GHz Nb on sapphire resonator, data is fit to equation 4.10 and the parameters can be found in table 3.

The initial characterisation of a sample involves checking the microwave through-put. Since all samples are coupled to a common feedline, there should be high transmission across the range 4-8 GHz, where the transmission band is limited by the cryogenic amplifier bandwidth and the presence of the 3.5 GHz high pass filters at the copper cold stage. A vector network analyser (VNA) is used to measure the microwave transmission.

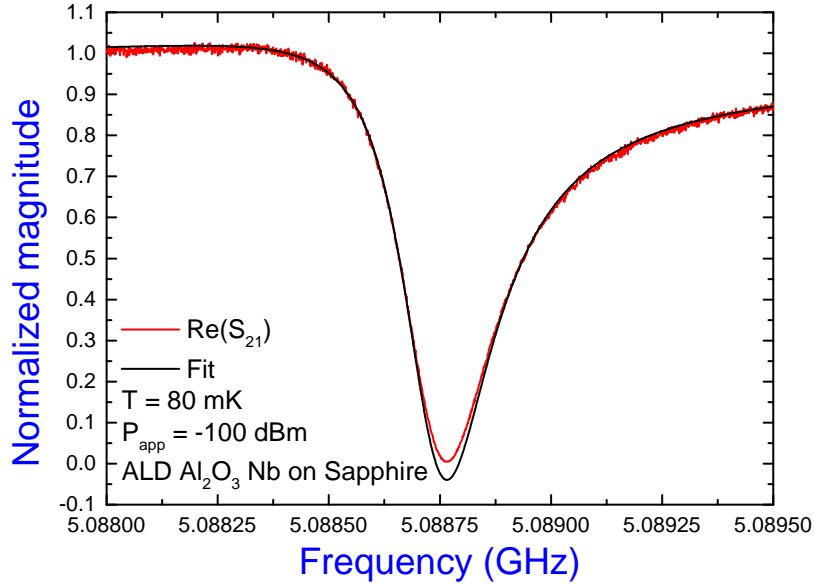


Figure 8.4: A plot showing the measured magnitude response of the 5.08 GHz ALD  $\text{Al}_2\text{O}_3$  Nb on sapphire resonator, measurement taken using complete amplifier chain with a total gain of 100 dB and noise temperature of  $\sim 7$  K. Data is fit to equation 4.10 and the parameters can be found in table 3.

The VNA is used to find the frequency of each resonator, and then measure their magnitude and phase response. This data can be fit to equation 4.10 to extract parameters such as the various quality factors, coupling parameters and the resonance frequency. Figures 8.3 and 8.4 show both the magnitude response of a resonator and the fit to equation 4.10. This provides the values of  $Q_i = 23.1 \times 10^4$ ,  $Q_L = 3 \times 10^4$  and  $g = 21.5 - 5.3j$  for the 5.08 GHz resonator and  $Q_i = 34.8 \times 10^4$ ,  $Q_L = 3.5 \times 10^4$  and  $g = 13.1 - 3.6j$  for the 6.98 GHz resonator. The parameters for all the resonators in this thesis are shown in table 3.

## 8.2 Loss and Noise analysis of superconducting resonators

The first measurement to perform after the initial characterisation is to determine the dielectric loss tangent of each resonator. This is performed by tracking the change in the centre frequency with temperature over the range of 50-800 mK. We gain several useful pieces of information from this measurement. Firstly we can verify the quality of the Nb film by checking it's surface  $T_c$  resembles the bulk  $T_c$ . Observation of a saturated Mattis-

Bardeen frequency shift around 800 mK confirms that the Nb film has good surface quality. Secondly, the dielectric loss tangent is then a measure of interface quality, and from this we can determine the sensitivity of the resonator to temperature fluctuations.

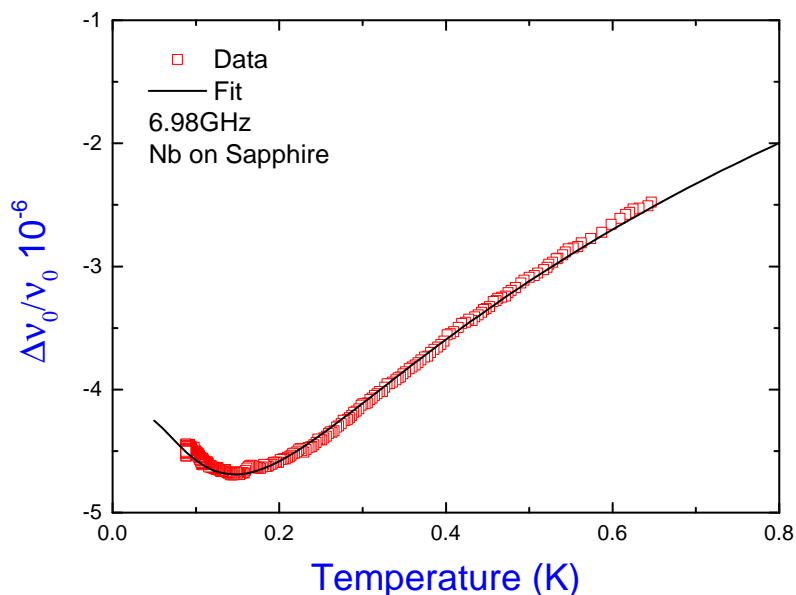


Figure 8.5: A plot showing the dielectric loss measured in the 6.98 GHz Nb on sapphire resonator, measurement taken by tracking the centre frequency of the resonator while varying the temperature of the mixing chamber. Data is fit to equation 2.6 and the parameters can be found in table 3.

From the measurement of frequency shift with temperature, equation 2.6 is used to extract the  $F \tan \delta$  value. For the 6.98 GHz bare Nb resonator shown in figure 8.5, this is  $F \tan \delta = 2.0 \times 10^{-6}$ . Which is comparable to previous low dielectric loss Nb on sapphire resonators of this geometry [37]. Importantly the geometry being the same means the filling factor,  $F$ , is the same allowing for valid comparisons.

Having shown the interface quality to be as good as previous samples, we next look into the effect of an additional dielectric layer atop the inter-digitated capacitor. Figure 8.6 shows the frequency vs temperature measurement which reveals  $F \tan \delta = 26 \times 10^{-6}$ , which is more than a 10x increase in the dielectric loss tangent compared to the bare resonator.

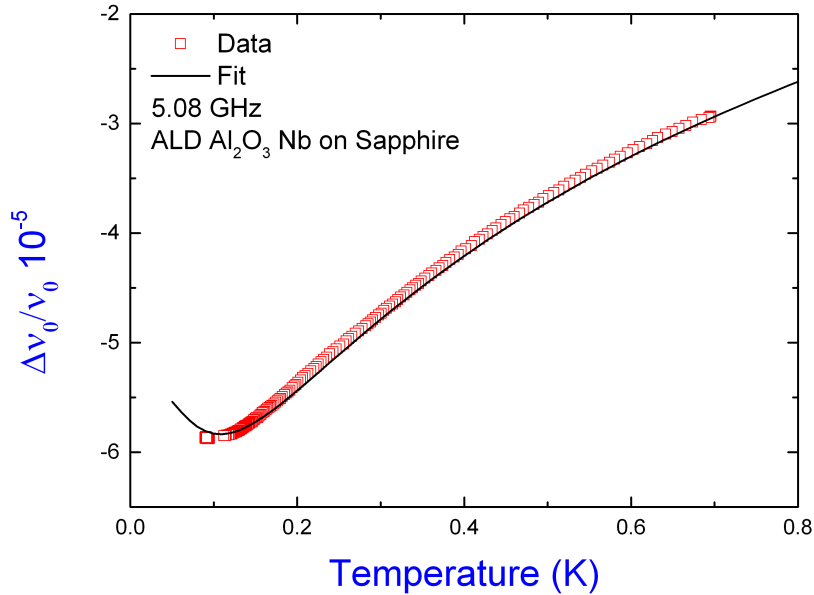


Figure 8.6: A plot showing the dielectric loss measured in the 5.08 GHz ALD  $Al_2O_3$  Nb on sapphire resonator, measurement taken by tracking the centre frequency of the resonator while varying the temperature of the mixing chamber. Data is fit to equation 2.6 and the parameters can be found in table 3.

At first, such an observation is perhaps not surprising as the presence of more dielectric material could produce a reduced interface quality. However, this is assuming the top dielectric interface both contributes comparably to the superconductor-substrate interface, and contributes greater than the existing superconductor-oxide surface. Certainly for non-oxidizing superconductors or after some annealing treatment the second assumption is not surprising. However, the first assumption would likely vary with deposition technique and treatment of the substrate surface.

The result of repeating these measurements of the dielectric loss tangent across many samples can be seen in figure 8.7. Here, we see that the dielectric loss tangent exhibits a uniform frequency dependence, preventing any design where a device can operate at some preferential frequency (in a glass the density of TLS states is assumed to be uniform with frequency). Additionally, the presence of an added dielectric layer is always seen to increase the level of dielectric loss by a factor of 5–10. Circled within figure 8.7 are the two

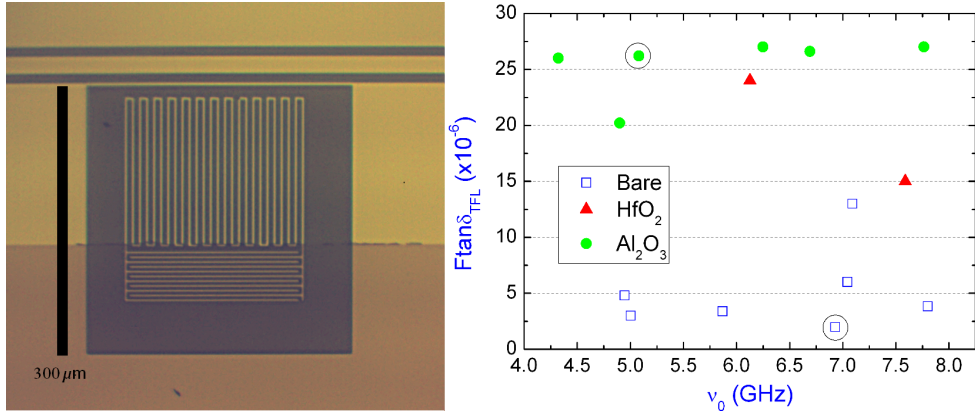


Figure 8.7: Left, an optical photo of a lumped element resonator with an additional  $\text{Al}_2\text{O}_3$  dielectric layer deposited by ALD. Right, a chart of the  $F \tan \delta$  value extracted for many resonators. Chart highlights a uniform frequency dependence, with the additional dielectric layer always leading to an increased level of dielectric loss.

resonators shown previously. These resonators are now measured using the Pound setup.

Each resonator was locked using the Pound setup and deviations of the resonance were tracked by a DAQ sampling the PID output voltage. The DAQ was sampling at a rate of 300 Hz so as to make the measurement dead-time small compared to the measurement interval. In subsequent measurements, a zero-dead time frequency counter was used to alleviate this problem. A non-negligible measurement dead-time can lead to decreased confidence of processes with short time constants (high frequency noise) fortunately, the high frequency noise is generally systematic in origin. As such it is not the focus of this thesis.

Once locked, the DAQ sampled the PID voltage for approximately 1.5 hours, this maintains a high statistical confidence for all timescales. For this duration, the temperature of the sample was determined by measuring two  $\text{RuO}_2$  thermometers where one is located at the mixing chamber, while the other is located adjacent to the sample box on the copper cold finger. Additionally the microwave drive was measured by a spectrum analyser via 10 dB coupler on the microwave in line on top of the fridge. Prior measurement of the heavily attenuated microwave in-line and the sample box insertion loss allows the microwave power reaching each resonator to be known to within a few dB.

The sampled voltage is analysed by both Allan analysis in figure 8.8 and spectral

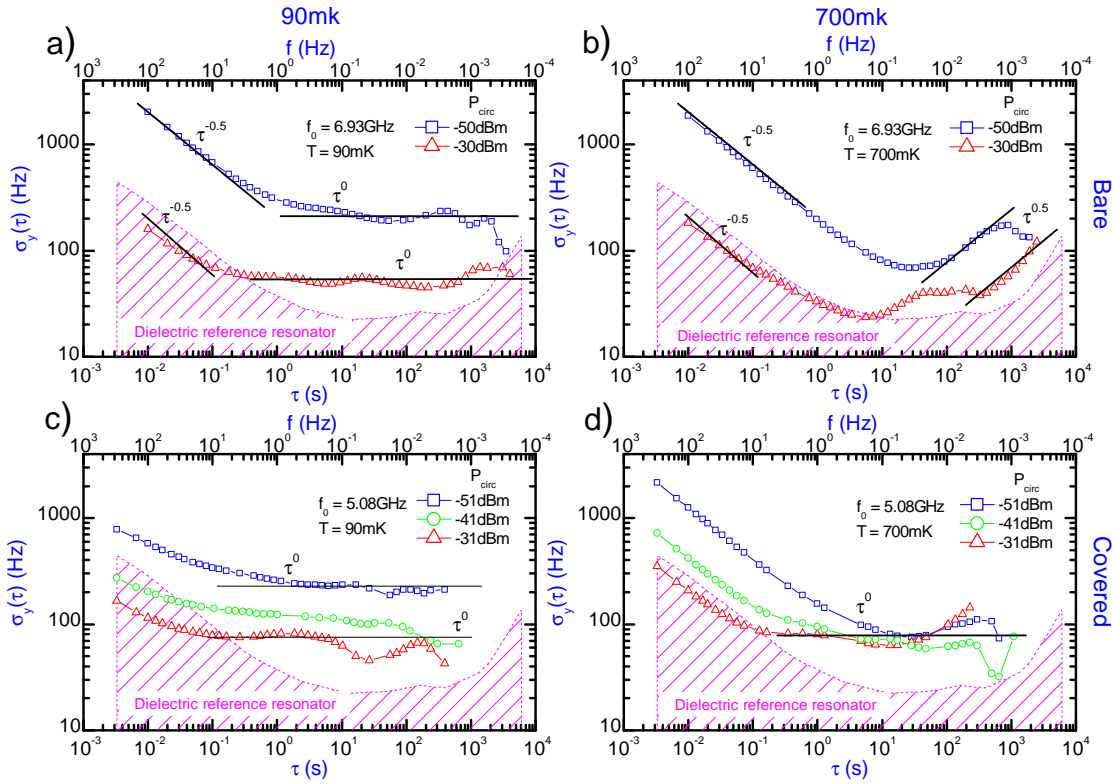


Figure 8.8: A plot showing the measured Allan deviation of superconducting resonators for analysing noise processes. Shown in pink is a calibration measurement on the dielectric resonator, this determines the systematic noise floor. Shown in red are measurements with a high applied microwave drive of -85 dBm, green corresponds to -95 dBm and blue corresponds to -105 dBm

analysis in figure 8.9. Shown in pink is a calibration measurement of the systematic noise contribution, measured by use of a dielectric resonator (in fact the data is that of figure 7.2). Here the flicker noise floor is shown by the  $\tau^0$  slope in the pink Allan analysis. This describes the systematic flicker noise due primarily to the amplifier chain and mixer. As shown in the previous section this flicker noise floor shows little power dependence, and therefore is valid for the subsequent measurements performed on the superconducting resonators.

Beginning with the high microwave drive, measurements on a bare resonator (shown in red within the top left of plots in figures 8.8 and 8.9) show a white frequency noise process described by  $\tau^{-0.5}$  ( $f^0$ ) at short times (high frequencies) using the Allan deviation

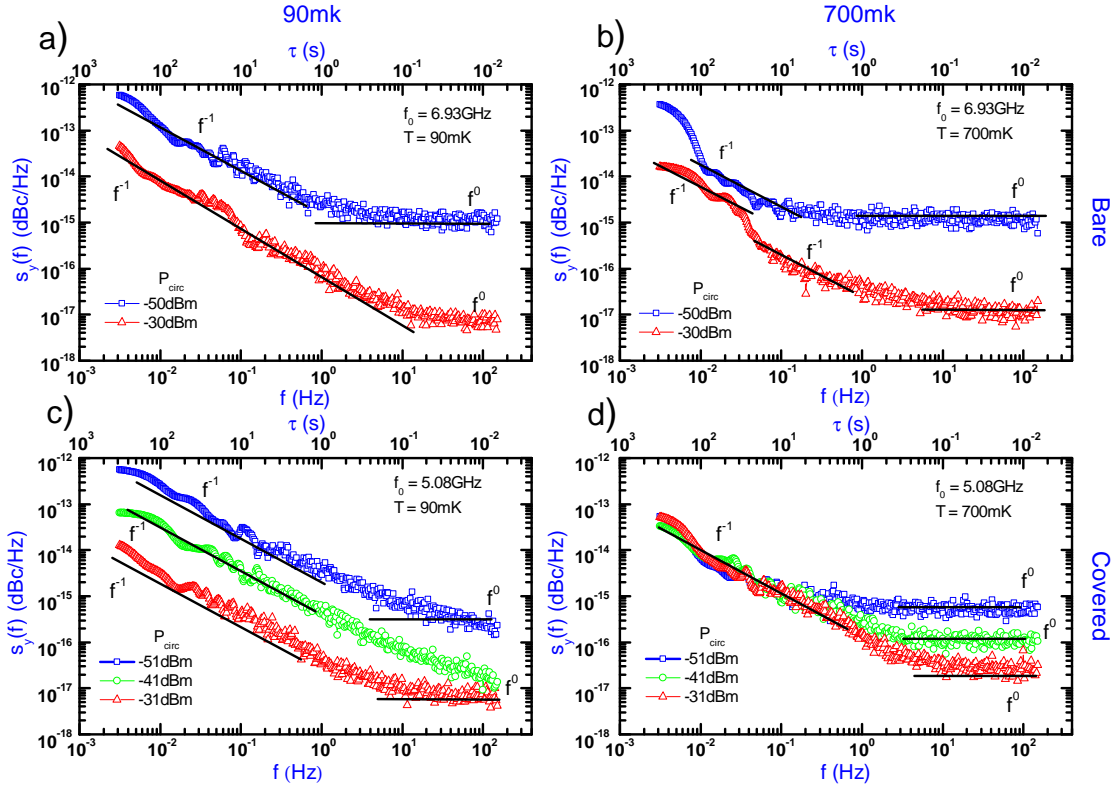


Figure 8.9: A plot showing the measured spectrum of frequency fluctuations in superconducting resonators. For clarity, the systematic noise floor has been removed from these traces. Shown in red are measurements with a high applied microwave drive of -85 dBm, green corresponds to -95 dBm and blue corresponds to -105 dBm

(spectrum of frequency fluctuations). This results in the resolution improving as the measurement time is increased. However, from 0.1 s a  $\tau^0$  flicker frequency noise process begins to dominate for all remaining time scales. Importantly when compared to the calibration measurement of the system noise floor we find the white frequency processes overlap. However, the superconducting resonator exhibits a flicker frequency noise in excess of the flicker noise floor.

The behaviour of the flicker process can be studied by varying the microwave drive. The microwave drive in the blue trace is 20 dB lower. Here, the white frequency noise process at short times has increased, suggesting the resolution is limited by a reduced signal-to-noise ratio. However, the flicker noise level is shown to have also increased,

despite figure 7.3 showing that the flicker noise floor is not dependent on the drive level. A direct verification of this is shown by repeating the measurement while changing the mixing chamber temperature as shown in the top right plots of figures 8.8 and 8.9.

At an elevated temperature, the white frequency noise level is shown to be unchanged at both microwave drives. However, the timescale over which this remains the dominant noise process has increased by an order of magnitude. Since the measurement is sensitive to the additive effect of all noise processes; this suggests the action of increasing the temperature, has led to a reduction of the flicker frequency noise level. As such the white frequency noise process remains dominant for a longer duration. Instead, at long times an emergent random frequency walk noise process shown by the  $\tau^{0.5}$  slope. It is suspected that the random walk process could be due to flux motion across the superconducting film.

Performing this measurement on the covered resonator is shown in the lower plots of figures 8.8 and 8.9. Here, the behaviour is the same, revealing a microwave drive and temperature dependent flicker frequency noise process. In fact the absence of any other noise process makes the elevated temperature measurement more illustrative of the temperature dependence since the flicker frequency noise level appears to have saturated and no longer shows any dependence on the microwave drive.

### 8.3 Discussion

The measurements of the dielectric loss tangent demonstrate a behaviour that can be parametrised by a bath of two level fluctuators using the theory of microwave absorption in glasses. Evidence for the existence of many TLFs makes the observation of flicker frequency noise unsurprising. This is due to random fluctuations within a two level system, which are well established for producing a superposition of Lorentzian spectra, such a superposition gives rise to the observed  $S = 1/f$  dependence. The properties of flicker noise in various charge sensitive devices has been a very active topic of research and is summarised earlier in table 5. However, this table contains no information on superconducting resonators. This is because the flicker process had not been observed in superconducting resonators until this work. Instead, table 7 highlighted that the observed noise in superconducting resonators was previously found to follow a  $S_y \propto 1/f^{0.5}$  slope.

This is the first measurement to find the flicker process to exist in superconducting resonators. The flicker frequency noise process is found to be dependent on both the microwave drive and the temperature. Here, the noise level increases with decreasing microwave drive and decreases with increasing temperature. In addition, the temperature dependence is sufficiently strong as to dampen the dependence of the microwave drive, this was seen most clearly in the bottom right plot of figures 8.8 and 8.9.

It is interesting to compare the observed noise level between the bare and covered resonator. The dielectric loss tangent of the covered resonator was  $\sim 10x$  higher than the bare resonator, suggesting either an increased number or strength of TLFs. Which could perhaps be expected to give rise to an increased flicker frequency level. Instead, the results find there to be little difference between the two resonators, which perhaps suggests there is only a weak dependence on the distribution of TLFs.

Further probing the microwave drive and temperature dependence of the flicker process in superconducting resonators is of great interest, especially to QIP applications. In these measurements, the temperature dependence could not be accurately examined. This is due to the large effect of frequency drifts occurring because of a comparatively large dielectric loss tangent. In order to accurately study a slow noise process, the temperature based frequency shifts must be lower than the flicker level over the duration of the measurement. The dielectric loss tangent and in particular the figures 8.6 and 8.5 allow the frequency shift for a modest temperature shift to be determined. As such, accurately measuring the temperature dependence would require a dielectric loss tangent of  $< F \tan \delta = 2 \times 10^{-6}$  such that the frequency shift due to a  $\pm 10$  mK temperature shift is  $< 100$  Hz. An accurate determination of the microwave drive dependence would be of further interest when approaching average resonator energies within the few photon regime. Realising these points will require further improvements in the Pound setup<sup>11</sup>, and the sample fabrication.

---

<sup>11</sup>The data in this chapter was taken using the measurement schematic shown in figure 6.1 but without the tunable attenuators, the YIG filters and the frequency counter. In addition the microwave generator itself acted as the VCO with the data acquisition performed by the DAQ.

# Chapter 9: Noise measurements of Superconducting resonators in varying temperature

This section focuses on improving the noise measurements of the previous section. The measurement method follows that outlined before; the resonator is characterised, the dielectric loss tangent is extracted, and then the resonator is locked for a few hours to probe the intrinsic fluctuations. This section improves on the last by performing a much finer study of the noise behaviour with microwave drive<sup>12</sup>. Additionally more temperature steps are examined. A subset of these results are featured within the proceedings of the International Superconductive Electronics Conference 2013 (ISEC) [124].

## 9.1 Description of the samples

The samples used in this section again consist of a sputter deposited niobium layer on r-plane sapphire. However, the geometry is a fractal resonator as described by the thesis of de Graaf [125]. Such a geometry is designed to be resilient to applied magnetic fields [79], and allow for an internal voltage bias [126], both of which can be necessary for coupling to TLS when Zeeman tuning is required. Structurally the fractal design is essentially a distributed resonator but with a much smaller width of the central conductor. The sample came from Chalmers University of Technology with each resonator coupled to a grounded Cooper pair box. By grounding the Cooper pair box, they remain inactive allowing the behaviour of the bare resonator to be explored.

The initial characterisation mirrors that of the previous section where a vector network analyser is used to trace the resonance curve. The magnitude and phase response can then be fit to equation 4.10 to extract the resonator parameters. Finding  $Q_i = 7.3 \times 10^4$ ,

---

<sup>12</sup>The measurement setup now begins to more closely resemble the schematic shown in figure 6.1. Since the last measurement but without the tunable attenuators have been added and the low frequency VCO has been added, this allows the readout to be performed by the frequency counter rather than the DAQ.

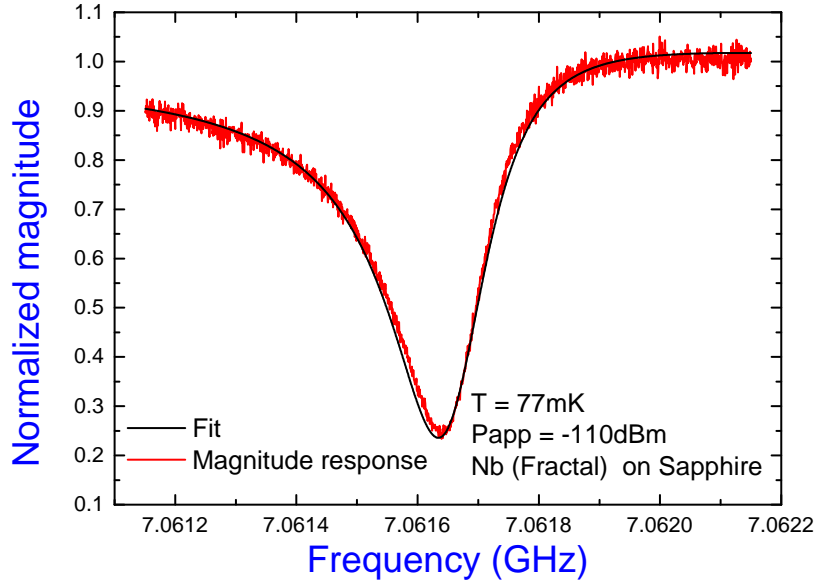


Figure 9.1: Plot of the measured magnitude response of the 7.06 GHz Nb on sapphire fractal resonator, measurement taken using complete amplifier chain with a total gain of 100 dB and noise temperature of  $\sim 7$  K. Data is fit to equation 4.10 and the parameters can be found in table 3.

$Q_L = 6 \times 10^4$  and  $g = 1.6 + 0.6j$ , this along with the parameters for all resonators used in this thesis can be found in table 3. Figure 9.1 shows the magnitude response of the 7.06 GHz fractal resonator.

## 9.2 Loss and Noise analysis of superconducting fractal resonators

The first measurement after initial characterisation is to determine the dielectric loss tangent. Changes in the centre frequency are tracked with temperature over the range 100-600 mK. the frequency shift is shown in figure 9.2 and can be fit to equation 2.6 to extract the dielectric loss tangent. However, for this resonator the different geometry means that the  $F$  (in the  $F \tan \delta$ ) is no longer the same as the lumped element resonators in the rest of the thesis, therefore directly comparing this loss tangent to those in the previous section is not trivial. The extracted value for the fractal resonator is  $F \tan \delta = 12 \times 10^{-6}$  which is lower than the value obtained for the covered resonator in the previous section but larger than the bare lumped element resonator of the previous section. This suggests the  $F$  is

larger for the fractal geometry, which is consistent with the fractal resonator having a larger interacting volume of TLFs. The second piece of information that is gained from figure 9.2 is that there is no deviation from the TLF behaviour described by the theory of microwave absorption in glasses. This suggests a fully saturated Mattis-Bardeen frequency shift, which only occurs far below  $T_c$  ( $T < T_c$ ) which suggests for this film the lower bound for  $T_c$  is  $\sim 7.5$  K.

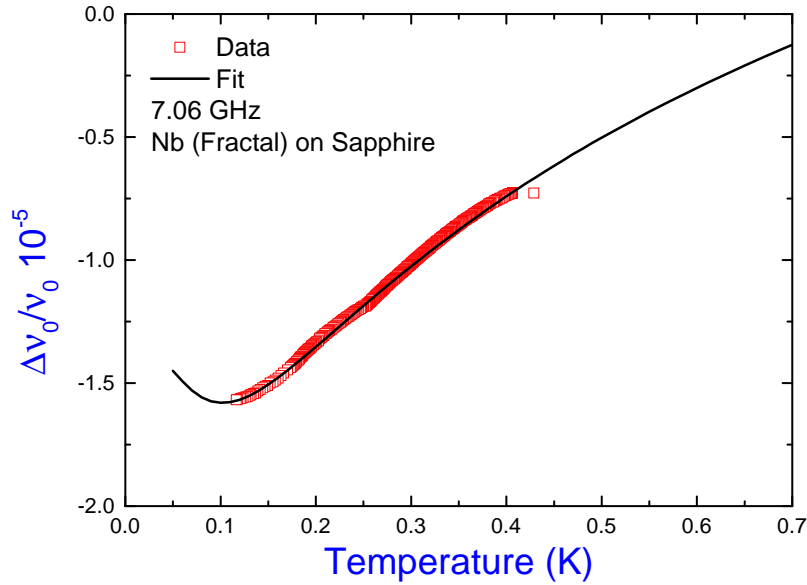


Figure 9.2: A plot showing the measured dielectric loss in the 7.06 GHz Nb on sapphire fractal resonator, measurement taken by measuring the centre frequency of the resonator while varying the temperature of the mixing chamber. Data is fit to equation 2.6 and the parameters can be found in table 3.

Next the intrinsic frequency fluctuations of the resonator is measured by readout of the Pound error signal over a timescale of several hours. The resulting time series was analysed by both Allan statistics and spectral analysis where both were shown to be equivalent. This measurement is repeated but for many different microwave drives, an example of the resulting Allan plot is shown in figure 9.3. Labelled on this figure are the two dominant noise processes observed, the  $\sigma_y^2 = 0.5h_0\tau^{-1}$  ( $S_y = h_0$ ) white frequency noise region and

the  $\sigma_y^2 = 2\ln(2)h_{-1}$  ( $S_y = h_{-1}/f$ ) flicker frequency noise region. The white frequency region was attributed to frequency resolution being limited by system noise, which is signal-to-noise dependent but not temperature dependent. The flicker noise region is more interesting, this was shown to be in excess of the systematic flicker level and so originates within the resonator. The flicker noise of the sample was shown to decrease with increasing temperature, and to decrease with increasing microwave drive. Where the dependence on temperature is dominant, such that while a dependence on microwave drive is seen at low temperatures, it is diminished at elevated temperatures. Figure 9.3 highlights the flicker noise level increasing with decreasing microwave drive.

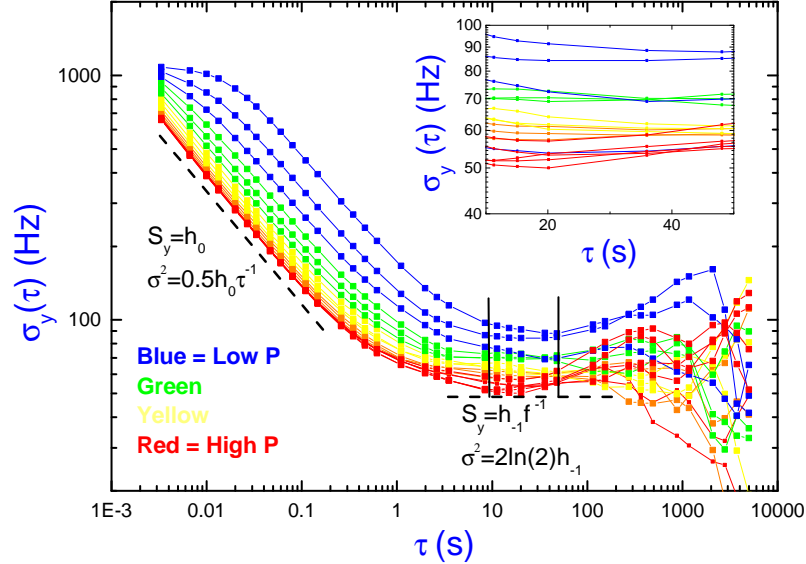


Figure 9.3: A plot showing the noise jitter of the 7.06 GHz Nb on sapphire fractal resonator analysed by Allan statistics. Measurements are taken with varying microwave drive within the range -96 to -110 dBm, where red corresponds to the high microwave drive and blue to the low microwave drive. The insert zooms on the Flicker region where the value of  $h_{-1}$  and hence the magnitude of  $1/f$  noise can be extracted.

To explore the behaviour of the  $1/f$  level with microwave drive, the energy stored within a resonator  $W_s$ , is introduced.  $W_s = 2Q_L S_{21}^{min} P_{app} / 2\pi\nu_0$  where  $Q_L$  is the loaded quality factor,  $P_{app}$  is the applied microwave power in watts,  $S_{21}^{min}$  is the depth of the

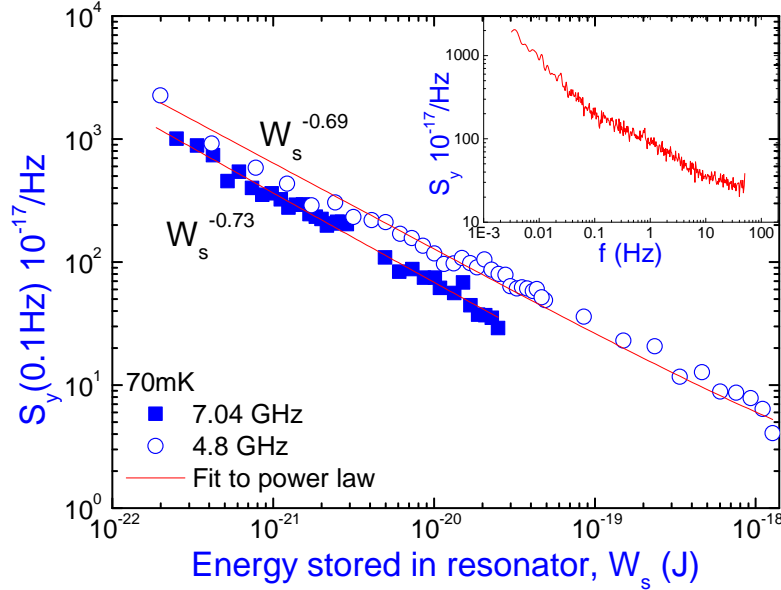


Figure 9.4: A plot showing the measured spectral noise at 0.1 Hz for the 7.06 GHz Nb on Sapphire fractal resonator under varying microwave drive. Two different fractal resonators are shown to obey a similar dependence where  $S_y(0.1 \text{ Hz}) \propto W_s^{-0.7}$ . At 0.1 Hz, the dominant noise process is 1/f and hence this describes the behaviour of 1/f noise with microwave drive. Inset shows the whole spectrum of frequency fluctuations, highlighting a flicker corner frequency around 100 Hz.

resonance dip and  $\nu_0$  is the resonant frequency. This unit allows for easier comparisons with other resonators and can also be easily translated into the average number of photons within the resonator by the division of  $h\nu_0$ . From the Allan statistics, the 1/f level can be calculated by extracting the horizontal line corresponding to  $h_{-1}$ . From this the region of the spectrum of frequency fluctuations  $S_y$  dominated by flicker noise can be calculated simply by  $S_y(f) = h_{-1}/f$ , hence  $S_y(0.1 \text{ Hz}) = h_{-1}/0.1$ . The spectrum at 0.1 Hz is used for ease of comparison with devices featured throughout the literature.

Figure 9.4 shows the behaviour of 1/f noise for two resonators measured by studying the spectrum at 0.1 Hz. The plot highlights that both resonators obey a similar dependence of  $S_y(0.1 \text{ Hz}) \propto W_s^{-0.7}$  at 70 mK. Here, even at the highest energy within the resonator the 1/f level remains above the system flicker noise floor.

To examine the role of temperature; which was previously found to increase the 1/f level when the temperature decreased, and also leads to a saturation of the microwave drive

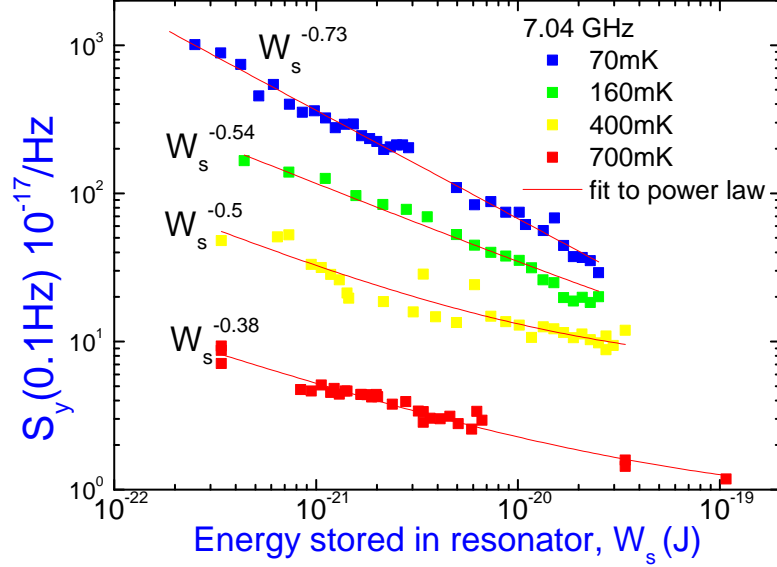


Figure 9.5: A plot showing the measured spectral noise at 0.1 Hz for the 7.06 GHz Nb on Sapphire fractal resonator under varying microwave drive at various temperatures. The magnitude of 1/f noise is shown to obey a power law varying with the energy in the resonator as  $S_y(0.1 \text{ Hz}) \propto \sim W_s^{-b(T)}$ . The behaviour is also shown to be temperature dependent.

dependence. The measurement shown in figure 9.4 was repeated for several temperatures between 70-700 mK. This is now shown in figure 9.5. Here, for the same energy in the resonator (ie. same microwave drive) the 1/f level is seen to decrease with increasing temperature, consistent with previous observations.

### 9.3 Discussion

The measurements within this section have built on the initial observations of the previous section. These were that superconducting resonators exhibit an excess flicker noise, which is larger than the systematic noise floor due to the amplifier/mixer chain. Furthermore the flicker noise found within superconducting resonators is found to be dependent on both the microwave drive and temperature. A behaviour that scales as  $S_y(0.1 \text{ Hz}) \propto A(T)W_s^{b(T)}$  is found, where  $A(T)$  indicates a temperature dependent behaviour on the noise magnitude such that increasing temperature leads to a decreased noise magnitude. The microwave drive dependence is summarised by  $W_s^{b(T)}$ , where  $W_s$  is

the energy within the resonator, and  $b(T)$  is a temperature dependent parameter describing the strength of the microwave drive dependence, such that the dependence gets weaker with increasing temperature.

It is interesting that despite the very different resonator geometry, the observed behaviour agrees with the previous observations. This supports a TLF based explanation since only the TLF density and the filling factor  $F$  would be expected to be different between the samples measured so far. As covered within the literature review, a two level system is capable of producing a Lorentzian spectrum, the superposition of many such spectra produces the  $1/f$  spectrum.

Table 5 overviews the behaviour of flicker noise observed in many superconducting devices. It should be stressed that the typical behaviour is that of an *increasing* noise magnitude with increasing temperature, therefore these results are in contrast to that typical trend. In general, it is assumed that all the systems explored within table 5 cannot have resonant interaction with the TLFs. It is because of this that the number of interacting TLFs scales approximately as  $k_B T$ , so for a DC system the noise magnitude increases with temperature as more TLFs interact with the sample [101].

Qualitatively the ability to have resonant interactions can be understood as follows. The natural timescale to consider is the ringing time of the resonator  $\tau_{res}$  where  $2Q_L/\nu_0 = 1/f_L = \tau_{res}$ . This is the average lifetime of a photon within the resonator. The resonator is coupled to an approximately fixed number of TLFs, therefore within the ringing time of the resonator there is an approximately fixed number of times that all TLFs could be excited. At low temperatures, there are no thermal excitation of the TLFs, which means excitation is only possible by the absorption of resonant photons. This results in a high probability of photon absorption and so a strong behaviour with microwave drive (where a photon can be caught and released multiple times). Increasing temperature leads to thermal excitation of the TLFs, reducing the maximum number of times that photon absorption can contribute to the excitation of TLFs. This leads to a reduced probability of photon absorption, resulting in a weaker dependence on microwave drive. As such, measurements at different temperatures are probing the ratio of TLF excitations due to photon absorption rather than thermal excitation.

Further measurements at more temperatures are required to examine this interesting behaviour, and to develop a better model to describe it. Also, measurements probing lower microwave drives towards the single photon energies would be of interest to QIP applications. Measurements at more temperatures will require a much lower dielectric loss tangent. This is due to slow thermal drifts masking the low frequency component of the spectrum. In figure 9.5, measurements are performed at 4 temperatures being 70 mK, 160 mK, 400 mK and 700 mK. The data for three of these temperatures is very clean due to either high thermal stability at fridge base temperature (70 mK), or due to TLF saturation (160 mK and 700 mK). The remaining 400 mK data set contains more spread due to thermal fluctuations. This can be explained by looking at figure 9.2 where a 150 mK Temperature shift produces a fractional frequency shift of  $5 \times 10^{-6}$  equivalent to  $\sim 35$  kHz. A  $\pm 10$  mK temperature fluctuation will produce a  $\sim 2$  kHz frequency fluctuation. Importantly this is much larger than the flicker noise level which was shown in figure 8.8.

Although some considerable progress has been made to achieve the targets outlined at the end of the last section, the targets remain for further study.

# Chapter 10: Examining the $1/T^\beta$ dependence of $1/f$ noise in superconducting resonators

This section focuses on experiments to explicitly determine the nature of the inverse  $T$  dependence of  $1/f$  noise which has been observed in previous chapters. Epitaxially grown samples are used to attain an ultra low dielectric loss tangent to allow the temperature dependence of  $1/f$  noise to be experimentally mapped out. The exact dependence is of particular interest to determine whether the noise originates from a spin or charge based fluctuation. The results discussed here are an early understanding of those featured on the ArXiv [127] and are modelled on a soon to be published theory by L. Faoro and L. Ioffe. Experimentally the setup has now been improved to include YIG filters and a better second amplifier, it therefore is the final schematic shown in figure 6.1.

## 10.1 Description of the samples

The samples used in this section consist of an epitaxially deposited niobium layer on  $r$ -plane sapphire. These films were obtained from the Institute of Microelectronics Technology and High Purity Materials, of the Russian Academy of Sciences [128]. The films were patterned at Royal Holloway into the familiar lumped element geometry. After this they were baked further to anneal the Nb. Two samples were fabricated, one simply consisting of epitaxially grown Nb (referred to as epi-Nb) and another which had an additional Pt capping layer deposited in-situ (referred to as epi-Nb+Pt). The Pt capping layer is  $\sim 5$  nm thick and should reduce the intrinsic surface oxide of the Nb layer.

Again, for the initial characterisation a vector network analyser was used to trace the resonance curve. The magnitude and phase response can then be fit to equation 4.10 to extract the resonator parameters. This provides the values of  $Q_i = 24.1 \times 10^4$ ,  $Q_L = 7 \times 10^4$  and  $g = 6.6 + 0.2j$  for the 5.55 GHz resonator and  $Q_i = 34.8 \times 10^4$ ,  $Q_L = 7.8 \times 10^4$  and

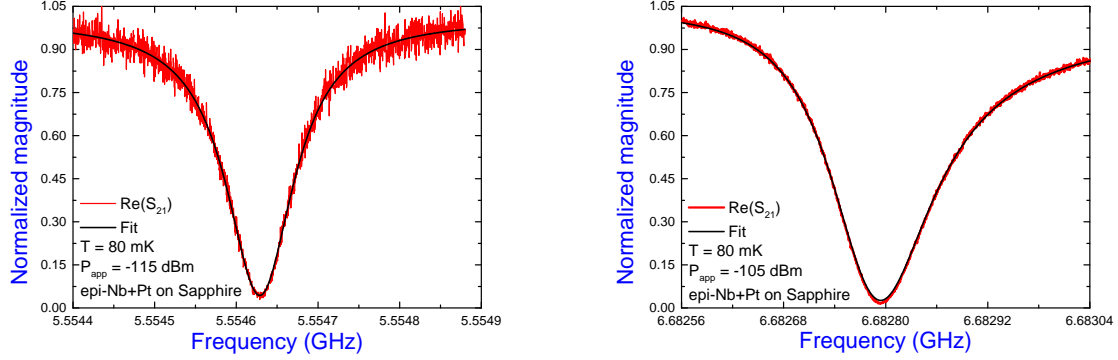


Figure 10.1: A plot showing the measured magnitude response of the 5.55 GHz and 6.68 GHz epi-Nb+Pt on Sapphire LE resonators, measurement taken using complete amplifier chain with a total gain of 100 dB and noise temperature of  $\sim 7$  K. Data is fit to equation 4.10 and the parameters can be found in table 3.

$g = 13.1 - 2.1j$  for the 6.68 GHz resonator. The parameters for all the resonators in this thesis are shown in table 3. Figure 10.1 shows the magnitude response of the 5.55 GHz and 6.68 GHz LE resonators.

## 10.2 Extracting loss tangents from epitaxially grown resonators with ultra low dielectric loss

Earlier sections have outlined the development of the Pound technique for readout of Hz-level changes in the resonators. The loop has also been optimised for readout at low microwave drive, where measurements were performed with fewer than  $\sim 100$  photons within the resonator, this is required to make the noise measurements relevant for QIP applications. These steps have also been necessary to enable the measurement of ultra low dielectric loss tangents, where the total frequency shift between 0.1–1 K is less than 10 kHz. In general the samples measured throughout this thesis have a  $T_c$  sufficiently high, that measurements below 1 K are not affected by Mattis-Bardeen mechanisms. In the event of a lower  $T_c$  the Mattis Bardeen frequency shift acts against the TLF frequency shift. When this occurs a high sensitivity is required to measure the now reduced frequency shift. This is because when an overlap occurs, the two effects will counter one another - that is unless one (likely the Mattis-Bardeen) dominates.

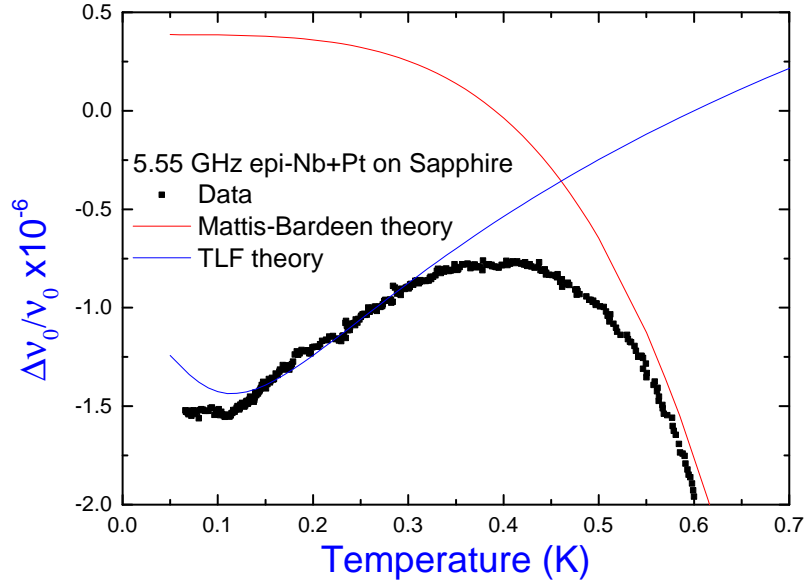


Figure 10.2: A plot showing the measured dielectric loss in the 5.55 GHz epi-Nb+Pt on Sapphire LE resonator. The resonator exhibits an overlap of the Mattis-Bardeen and TLF regions. Approximate fits to the Mattis-Bardeen frequency shift is shown in red and an approximate fit to the TLF region is shown in blue using equation 2.6 and the parameters can be found in table 3.

Figure 10.2 shows the measured frequency shift with temperature for the 5.55 GHz epi-Nb+Pt resonator. The plot shows an overlap of the Mattis-Bardeen (shown in red) and TLF (shown in blue) behaviours. The presence of this overlap indicates the film exhibits a reduced  $T_c$  (found to be around 5 K from the Mattis-Bardeen fit). It was believed that the surface *Pt* was responsible for the reduced  $T_c$ , however the epi-NB resonators also showed a reduced  $T_c$ , meaning the Nb itself is likely the problem. This overlap complicates the process of extracting the dielectric loss tangent. The blue fit within figure 10.2 is actually the pseudo-loss tangent in that the frequency shift is being damped by the overlapping Mattis-Bardeen region. To extract the real loss tangent, one needs to fit the background Mattis-Bardeen effect and then subtract the larger TLF-induced frequency shift.

Figure 10.3 shows a measurement of the dielectric loss tangent of the 6.68 GHz epi-Nb+Pt resonator. Again, an overlap of the Mattis-Bardeen and TLF regions is observed consistent with the 5.55 GHz resonator. Within this plot the green curve is a fit the

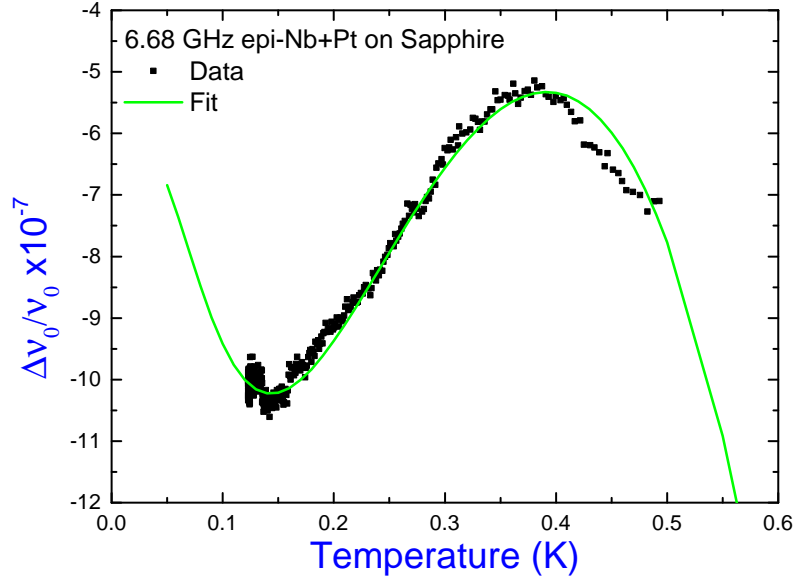


Figure 10.3: A plot showing the measured dielectric loss in the 6.68 GHz epi-Nb+Pt on Sapphire LE resonator. The resonator exhibits an overlap of the Mattis-Bardeen and TLF regions. Shown in green is a compensated fit of the TLF based frequency shift using equation 2.6 against a background Mattis-Bardeen based frequency shift, the parameters can be found in table 3.

TLF-induced frequency shift against the Mattis-Bardeen background. This constitutes the real dielectric loss tangent, finding  $F \tan \delta = 1.1 \times 10^{-6}$  for the 6.68 GHz resonator and  $F \tan \delta = 1.3 \times 10^{-6}$  for the 5.55 GHz resonator. Importantly these values correspond to frequency shifts of  $< 5$  kHz between 0.1-0.5 K. It follows that a  $\pm 10$  mK temperature shift relates to a  $\sim 200$  Hz frequency shift. Importantly, this is below the observed flicker jitter for microwave drives below -100 dBm (shown in figure 8.8). As such, these samples are suitable for accurately mapping the temperature dependence of the flicker frequency noise.

### 10.3 Mapping the temperature dependence of 1/f noise in epitaxial superconducting resonators

The previous sections have highlighted the use of a Pound error signal to extract the intrinsic frequency fluctuations of the resonator over long periods of time. It was shown that the measured time series can then be analysed by Allan statistics to check for temperature induced frequency drifts. Following this, the Allan statistics can find the timescales over

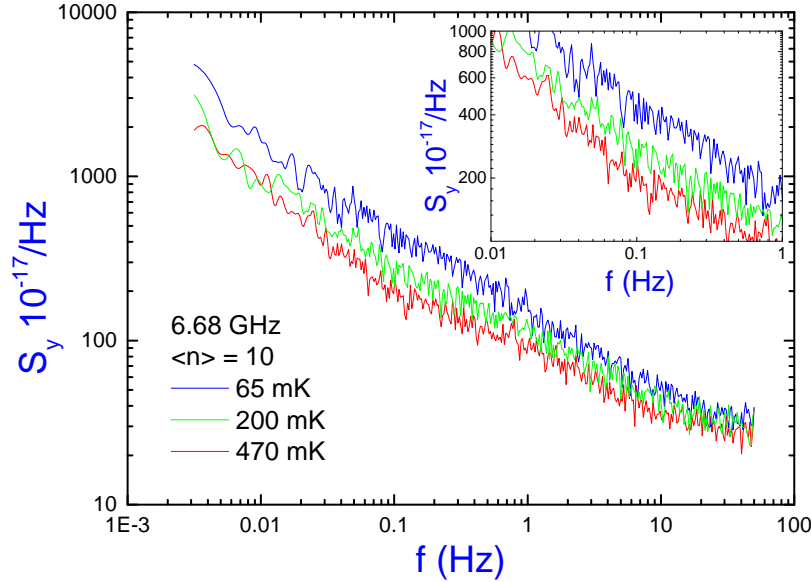


Figure 10.4: A plot showing the measured spectrum of frequency fluctuations for the 6.68 GHz epi-Nb+Pt resonator. Plot highlights that  $1/f$  noise dominates up to 50 Hz where white frequency noise begins to become apparent. Inset shows a zoom in about 0.1 Hz. This highlights that as the temperature is increased, the spectral noise at 0.1 Hz (flicker level) is found to decrease.

which the flicker process dominates the frequency jitter. The flicker level can then be found from the extracted  $h_{-1}$  value and from this the spectral noise at a given Fourier frequency can be calculated. Figure 10.4 shows the flicker region to exhibit no ringing, which validates the assumption of that  $S_y \propto h_{-1}/f$ . The chosen frequency has been 0.1 Hz due to the prevalence in literature (see table 5). However, the behaviour of the flicker process should be the same for any chosen Fourier frequency where the flicker process dominates.

The literature review, and especially table 5, have summarised the general behaviour of  $1/f$  noise in a variety of superconducting devices. The general trend is that the noise level increases with temperature although some saturation is observed below  $\sim 200$  mK. As shown in the previous two sections, superconducting resonators do not follow this trend.

Recent results on SQUIDs have found the noise  $1/f$  level to increase with decreasing temperature [103]. Prior to this, the inductance in SQUIDs has been found to increase with decreasing temperature [129]. A result that was further clarified as  $1/T$  [130]. This

1/T dependence is related to a Curie-like inductance contribution from surface spins [131]. Importantly, cross-correlation measurements showed a high correlation between measured susceptibility and the flux noise  $S_\phi$ , which led to a conclusion that surface spins could explain the observed 1/f noise. More recently an observed increase in flux noise with decreasing temperature was seen as evidence for a spin glass transition around 1 mK [132]. Spin glass transitions produce a 1/T dependence of inductance contributions when approaching the glass transition temperature from above.

All evidence for a 1/f noise that increases with decreasing temperature is explained by spin contributions leading to flux noise. It is therefore of huge interest whether noise in the resonator is *in fact* due to spin contributions coupling, as opposed to charge fluctuations, which is generally assumed to be the case. As such, the intention for this section is to perform a measurement where  $S_y \propto \frac{1}{T^b}$ , and to determine the value of  $b$ .

Figure 10.5 shows a more detailed study of the spectrum of frequency fluctuations at 0.1 Hz vs. microwave drive and temperature. The  $x$  axis is rescaled into the average number of photons within the resonator, this is calculated by  $\langle n \rangle = W_s/h\nu_0$ , so the number of photons in the resonator scales linearly with applied microwave drive. At high microwave drive, the measured 1/f level saturates to the previously determined systematic flicker noise floor. When the microwave drive is decreased the resonator 1/f level rises from the systematic level. As before the strength of the microwave drive dependence is shown to be temperature dependent such that it is strongest at the lowest temperature. Additionally, the 1/f level for a constant microwave drive is decreased when temperature is increased. Although these effects have been slowly observed in previous sections, the behaviour here is much clearer.

The next measurement is to accurately map the temperature dependence for a constant applied microwave drive. Therefore, Figure 10.5 is useful to determine the appropriate microwave drive to operate at. Interestingly the fairly rapid saturation with both temperature and microwave drive suggests that the behaviour is probably only measurable for microwave drives corresponding to less than 100 photons. This implies that the high microwave drive (that is typically used for KIDs) leads to a saturation of the resonator 1/f noise. Instead, the systematic noise floor becomes the ultimate limitation. This leaves QIP

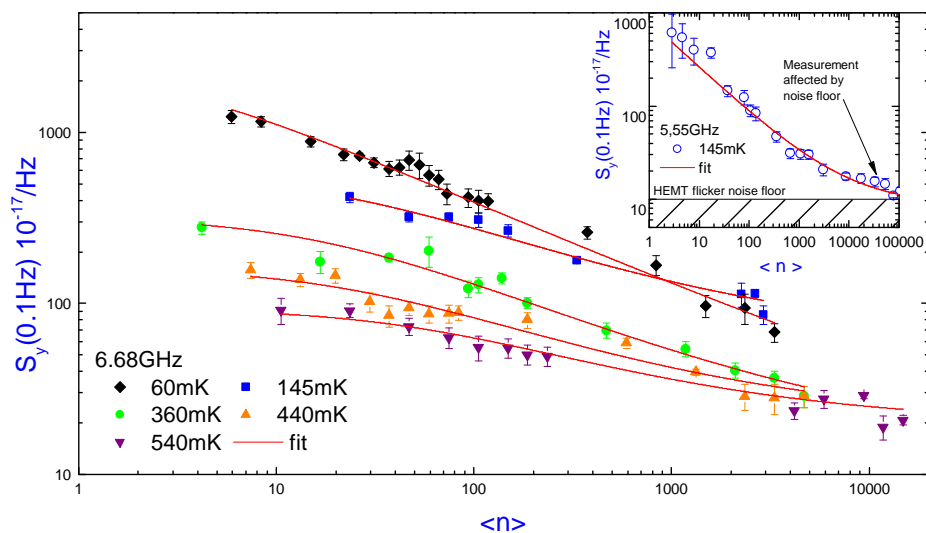


Figure 10.5: A plot showing the measured spectrum of frequency fluctuations at 0.1 Hz vs microwave drive for the 6.68 GHz epi-Nb+Pt resonator. The microwave drive has been rescaled into the average number of photons within the resonator  $\langle n \rangle$ . Both the  $1/f$  level and the strength of microwave drive dependence are shown to vary with temperature. Inset explicitly highlights saturation to the systematic flicker noise floor in the high microwave drive limit. As the microwave drive is decreased, the  $1/f$  level is seen to rise out from the systematic  $1/f$  flicker noise floor.

applications and parametric amplifiers as the research areas affected by this measurement.

Figure 10.6 shows the spectrum of frequency fluctuations at 0.1 Hz vs. temperature for both the 5.55 GHz and 6.68 GHz epi-Nb+Pt resonators. Each point has an error bar which has been calculated from the Allan statistics, where the flicker region is described by the line  $\sigma_y = h_{-1}$ , this line is fit to the appropriate points of the Allan deviation between the timescales of  $\tau=1$  s and 100 s. The standard deviation of this line (of the  $h_{-1}$  value) is a measure of the averaged drift or ringing over 100 s. If the drift was too large, the data was removed, and that temperature point retaken. The resulting standard deviation was then converted into the correct units and used for the data points error bars. Each data set for a resonator was fit to the equation  $S_y(0.1 \text{ Hz}) = A(W)/T^b + C$  to extract the value of  $b$ . Within this equation, the term  $A(W)$  is found to vary with the microwave drive and the term  $C$  is the systematic flicker noise floor. This systematic flicker noise floor is additive, unlike its white noise which obeys the Friis formula.

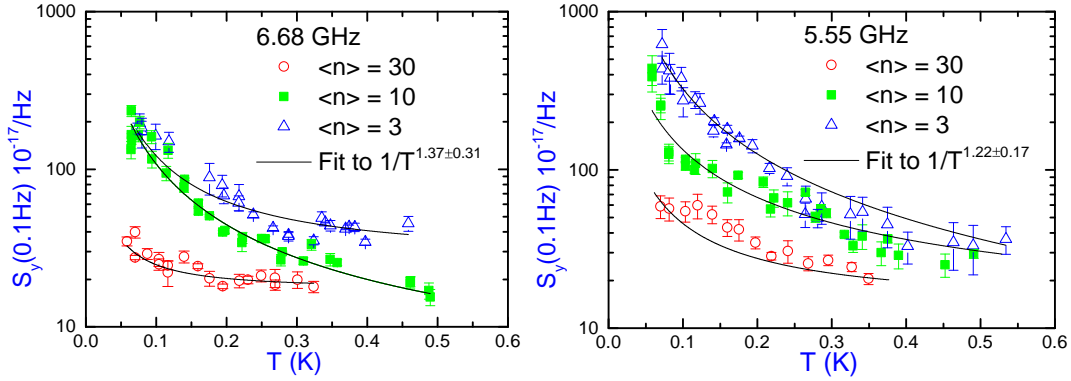


Figure 10.6: A plot showing the measured spectrum of frequency fluctuations at 0.1 Hz vs. temperature for the 5.55 GHz and 6.68 GHz epi-Nb+Pt resonators. Plot explicitly highlights saturation to the systematic flicker noise floor in the high temperature limit. Fits to the function  $S_y(0.1 \text{ Hz}) = A(W)/T^b + C$  are shown for each resonator where the parameter  $b$  is shared for all measurements on a given resonator.

## 10.4 Discussion

Within figure 10.6, the value of  $b$  is found to be  $1.22 \pm 0.17$  for the 5.55 GHz resonator and  $1.37 \pm 0.31$  for the 6.68 GHz resonator. While close the error does not allow for unity, which rules out a simple  $1/T$  dependence. This result and its implications will now be discussed.

The observed increasing flicker level with decreasing temperature had previously only been observed within systems sensitive to flux noise. This flux noise had been related to inductance noise through cross correlation measurements. Importantly, the inductance is due to surface spins, which obey a Curie type behaviour. In this model, the surface spin contribution to the inductance can be estimated by  $L'_{spin} = \mu_0^2 \mu^2 \sigma_s (l/r) / 3k_B T$ . To check its applicability to the resonator we can use appropriate values of surface spin density  $\sigma_s = 10^{-16} \text{ m}^{-2}$  [131],  $\mu = \mu_B$ ,  $T = 60 \text{ mK}$ , the length  $l = 1000 \text{ } \mu\text{m}$  and width  $r = 4 \text{ } \mu\text{m}$ . These values lead to  $L'_{spin} = 5 \times 10^{-16} \text{ H}$  for a typical resonator. For comparison, the noise magnitude at 60 mK in the low power regime is  $S_y(0.1 \text{ Hz}) = 3 \times 10^{-15}$ . The spectra equate to  $\sigma_y = \sqrt{2} \times 10^{-7}$ , which for a 6 GHz resonator is approximately a 450 Hz jitter. Producing such a jitter by inductance fluctuations would require  $\delta L = 5 \times 10^{-16}$ . This is approximately equal to the surface spin contribution to the inductance when using appropriate parameters

and a reasonable estimate of the surface spin density<sup>13</sup>.

This analysis shows it is perfectly feasible that the origin of 1/f noise in superconducting resonators is in fact surface spins. There are two experiments which could discriminate whether surface spins are the cause; either perform measurements in an applied magnetic field, or, experimentally verify the exact temperature dependence and whether it deviates from 1/T. Due to a lack of comparative studies in the literature of the 1/f noise of other devices in applied magnetic fields at mK temperatures, it was chosen to perform the fine measurement of temperature dependence. In this case the observed non unity value of  $b$  would suggest that surface spins are not the underlying cause of 1/f noise in superconducting resonators.

Instead a further examination of TLF theory is required. Specifically models describing interacting TLFs need to be examined. Recently Faoro and Ioffe introduced a model of interacting TLFs to explain the weaker than expected saturation of quality factors with microwave drive in superconducting resonators [69]. At its simplest, the model proposes two populations of TLFs, one *fast* population which is coherent with the resonator. The second population acts to slowly modulate the line splitting of the *fast* TLFs. Evidence for this idea can be found from recent measurements of  $T_1$  and  $T_2$  times of superconducting qubits [133], which found  $T_2 \propto \frac{1}{T^{1.24}}$ . Conventional TLF theory only allows for relaxation via phonons which produces  $T_2 \propto \coth(E/2k_B T)$  where  $E$  is the TLF line splitting energy. The coth dependence would scale as 1/T in the low temperature limit.

To explain this disagreement with conventional TLF theory it is proposed that the distribution for TLF energy asymmetry should be non unity (where it is unity for conventional theory). Instead a parameter  $\mu$  is introduced to indicate the energy distribution is non stationary (meaning the TLFs are interacting). The phonon relaxation path for TLFs is now dwarfed by a new relaxation mechanism due to spectral diffusion. This leads to a  $T_2 \propto \frac{1}{T^{1+\mu}}$  dependence, where a value of  $\mu=0.12$  was recently found in superconducting qubits. This model, which will be published by Faoro et al. soon describes the contribution

---

<sup>13</sup>However it should be noted that this analysis calculates the mean contribution of surface spins to the inductance. This is not a calculation of the fluctuation caused by these surface spins. Therefore for these to account for the noise would require fluctuations to be comparable in size to the mean contribution. This is one of the main reasons why the effect is not attributed to surface spins.

of spectral diffusion to resonator jitter by

$$S_y(f) = \langle \alpha \rangle P_0 \frac{T}{\Gamma_2^2} \frac{1}{\sqrt{1 + \Omega^2/\Gamma_1\Gamma_2}} \frac{\int_{V_h} |E|^4 dV}{(\int_V |E|^2 dV)^2} \frac{1}{f} \quad (10.1)$$

Here, the  $\langle \alpha \rangle P_0$  and the integral terms represent a Filling factor and dielectric loss within the resonator [107]. Essentially, this simplifies to

$$S_y(f) \propto \frac{1}{T^{1+2\mu}} \frac{1}{\sqrt{1 + \Omega^2/\Gamma_1\Gamma_2}} \frac{1}{f} \quad (10.2)$$

Clearly highlighting a  $1/f$  spectrum as expected. Importantly, this model has three important features

- The  $T/\Gamma_2^2$  term simplifies to give  $S_y \propto \frac{1}{T^{1+2\mu}}$  where a value of  $\mu=0.1-0.2$  would explain the results of figure 10.6
- $S_y \propto \frac{1}{\sqrt{1+\Omega^2/\Gamma_1\Gamma_2}}$  the terms within the  $\sqrt{\phantom{x}}$  are usually reformed into  $\sqrt{1 + (E_c/E)^2}$  [40], which represents the saturation of TLFs by absorption of resonant photons. Having shown  $\Gamma_2 = 1/T_2$  to be temperature dependent, this results in the critical energy  $E_c$  also being temperature dependent, and hence  $E_c$  decreases as the temperature is increased. This produces weaker microwave drive dependence when the temperature is raised, and explains the results in figure 10.5.
- The microwave drive dependence in 10.5 as the interesting property that the noise level saturates in the limit of low microwave drive, but the level of saturation is temperature dependent. This can be accounted for by fitting figure 10.5 to the equation  $S_y = \frac{A}{\sqrt{T^{2(1+2\mu)} + BW}}$ . Where  $T$  is the temperature,  $W$  the microwave drive and  $A$  and  $B$  are constants. In this case  $A = 4 \times 10^{-16}$  for all data sets, while  $B = 2.5 \times 10^{-4}$  when above 200 mK and  $B = 3.5 \times 10^{-3}$  when below 200 mK.

Therefore, a model involving interacting TLFs is able to account for all the observed effects, but most importantly the derived value of  $\mu$  is in strong agreement with that of superconducting qubits [133].

# Chapter 11: Conclusions

This section, will briefly overview the work within this thesis. Highlighting which areas have been successful, and which other areas need more work. Finally some perspective of where this work is in relation to the field will be given, and from this some outlook on possible directions of the field will be given.

## 11.1 The Pound loop

In essence this thesis covers two things, firstly the use of a frequency readout technique based on Pound locking which is new to this field, and secondly the nature of slow fluctuations within superconducting resonators. Despite being new to the field, Pound based detection was in fact a very well established technique over 50 years ago [52]. The Pound based setup was studied and used for three reasons:

- The technique is used within frequency metrology to realise unparalleled frequency resolution
- The use of feedback would enable to study of processes over extended periods of time, while being able to resolve drifts
- Due to its use with dielectric resonators, the setup is simple to realise with easily available microwave equipment.

Within the earlier sections the theory of Pound loop was examined, detailing how the error signal is derived, and how the setup is realised. A dielectric resonator was then used to examine the stability limits of the loop itself. These steps ensured the suitability of the technique for studying slow fluctuations in superconducting resonators, which was the topic of the experimental sections of the thesis.

Essentially, the loop is a very sensitive readout of changes to a resonator, where for the topic of the thesis, these changes were intrinsic to the resonator and due to TLFs. However, these are not the only changes that can be detected. As detailed in the introduction, superconducting resonators generally have two applications, either, kinetic inductance detectors, or as elements in QIP. The Pound setup should be applicable for both of these

applications, since they rely on frequency shifts in the resonator.

## 11.2 Noise studies in superconducting resonators

The work within this thesis has extended the studied time scale of noise in superconducting resonators from 30 s to 10,000 s. As such while many previous studies had looked at the noise between 300 Hz and 1 kHz, this thesis instead looked deeply into the noise at lower frequencies. In doing so, a  $1/f$  noise process was found, consistent with other charge sensitive devices, and the nature of this  $1/f$  noise became the other main focus of this project. What was found can simply be summarised as

- $1/f$  noise level increases with decreasing temperature
- $1/f$  noise level increases with decreasing microwave drive
- The microwave dependence is also temperature dependent and reduces with increasing temperature

The main driving point for this work (and why noise studies were followed rather than the CPB work mentioned in the last section) was that this dependence is in contrast to that typically observed in charge sensitive devices, where  $1/f$  noise is found to increase with increasing temperature. A few questions arise from this:

- If the resonator exhibits a noise that decreases with increased  $T$ , should kinetic inductance detectors be operated at elevated temperatures, e.g. 200 mK?
- If the resonator and a charge sensitive device (e.g. Qubit) have contrasting noise dependences with temperature, which is dominant?

For the first point there is a caveat that the temperatures still be far below the  $T_c$ , as the sensitivity is known to reduce drastically with increasing temperature [49], however this was only measured for Al ( $T_c = 1.2$  K) where the temperatures involved were not below the  $T_c/10$  limit.

The second point has several implications which all depend on which system (resonator or device) produces the dominant noise contribution. For a qubit, the observation that  $T_1$  and  $T_2$  drop rapidly with increasing temperature [133] implies a low temperature is

always needed. However, the dependence saturates below 100 mK, leaving the possibility that a slightly elevated temperature e.g. 80 mK instead of 20 mK could be optimal. But, parametric amplifiers can also see resonators combined with devices. In these cases, the requirement for maximising  $T_1$  and  $T_2$  is not present, and hence one could operate at elevated temperatures. Measurements determining whether the resonator or the device dominates should be of huge interest to the development of parametric amplifiers. Certainly in the case of travelling wave parametric amplifiers [118], the system is essentially a resonator and one would expect the noise to behave the same.

A further point to be explored is that fabrication techniques may produce ways of engineering a reduced sensitivity to noise originating within the resonator. In this case, while the explicit origin of TLFs may not be known yet, further work may reveal more pieces of the puzzle. Certainly, this thesis has produced strong evidence for a model of interacting TLFs. Such a model produces advances away from the conventional theory which have existed for around 40 years.

### 11.3 Loose ends

Throughout this thesis the Pound technique has been implemented and improved for one purpose. This has been to study the noise processes which affect superconducting resonators. Although the phase space for noise measurements is large, this is not the only interesting property to measure with superconducting resonators. As covered in the introduction, the two main uses of superconducting resonators are as kinetic inductance detectors and in the solid state approaches to quantum information processing. The Pound technique should be suitable for measuring both of these applications of superconducting resonators. Due to the time constraints, and the decision to make noise measurements the focus of the project, the study of these applications was brief. However, the suitability of the Pound technique to measure these applications is covered below. It should be noted that the underlying mechanisms for these applications is not covered here as these were not the focus of the thesis. For a description of the KID see references [1, 7, 15] and for a description of QIP applications see references [2, 10, 134].

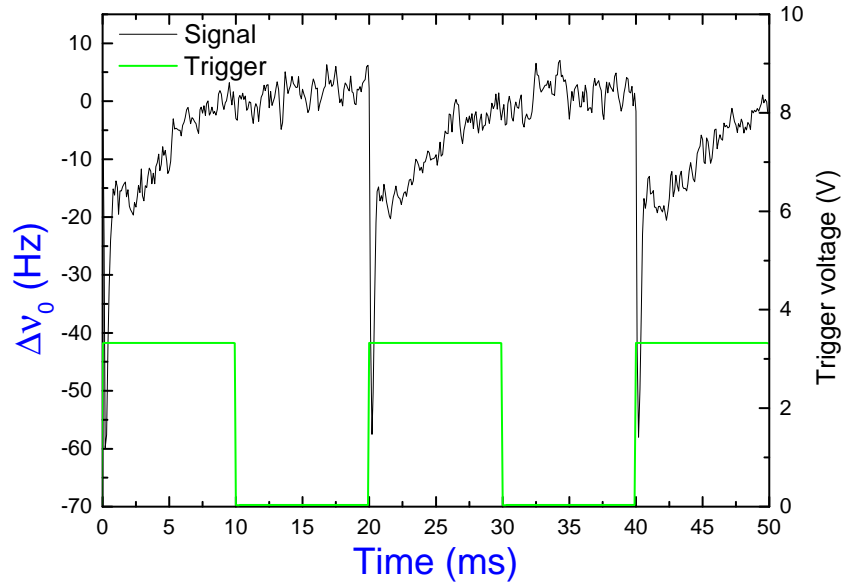


Figure 11.1: A plot showing the measured resonator response to strong irradiation at 635 nm. The trigger pulse is shown in green, where the laser diode switches on at the rising edge. The resonator response is shown in black.

### Using the Pound for kinetic inductance detectors

An optical fibre was installed within the dilution fridge to allow the sample to be irradiated at optical frequencies. A 635 nm pigtailed laser diode was used to produce the light, where the laser diode was biased to significantly below the lasing threshold. A triggering pulse, of varying duration between 8  $\mu\text{s}$  and 20  $\mu\text{s}$ , with a rise time of 90 ns was used to make the laser diode emit a short pulse of light. Between each pulse was a delay of 20 ms to ensure the resonator had fully relaxed between pulses. An oscilloscope can then be used to determine the frequency shift of the resonator by measuring the voltage output of the detector diode. This is shown in figure 11.1, the figure demonstrates a repeatable frequency shift upon the trigger rise. An advantage of the oscilloscope readout is that the modulation parameter is known, this means the conversion from voltage to frequency is simple, and hence figure 11.2 is scaled in Hz.

The frequency shift in figure 11.1, shows a long relaxation time, this corresponded to physical heating of the sample and matched measurements of the thermometer. By

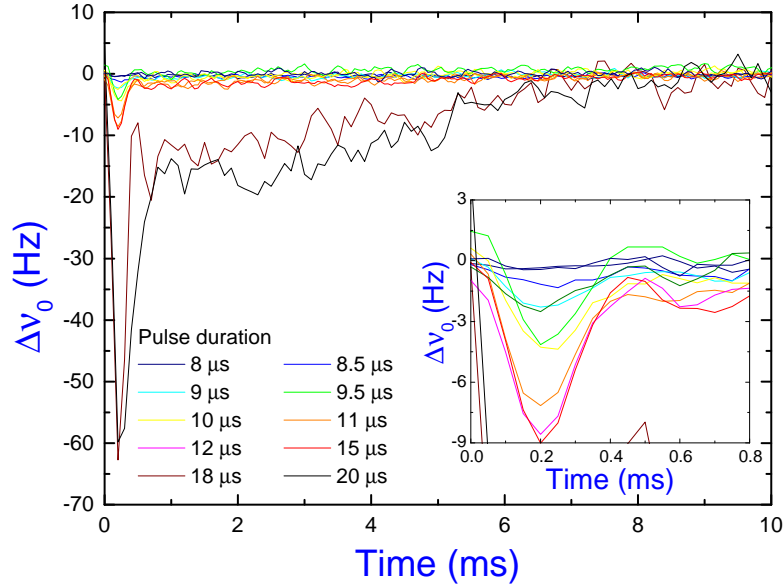


Figure 11.2: A plot showing the measured resonator response to varying irradiation at 635 nm. The width of the triggering pulse is varied to tune the number of incoming optical photons. Inset zooms on the response to the shortest pulse widths.

reducing the pulse width, the number of optical photons reaching the sample could be reduced. A repeated measurement showing the varying frequency response in changing pulse width is shown in figure 11.2. Here some caution is needed before evaluating the small size of the frequency shifts. To eliminate the effects of heating, the oncoming photon flux is reduced such that the probability of a photon being absorbed is close to zero. As such over the course of 128 measurements only a small number ( $<10\%$ ) absorbed a photon, resulting in a dampening out of the total measured frequency shift. It should be noted that this measurement was performed on the epi-Nb+Pt sample, which is not optimised for kinetic inductance operation. This means the kinetic inductance ratio is very small, making the resulting frequency shift very small, a fully optimised film such as that used in ref [135], would produce much larger frequency shifts and consequently need less averaging. A further observation is that the off pulse jitter magnitude is in the low 10s of Hz and hence is in agreement with the typical flicker limited jitter as shown in figure 8.8.

The original motivation for this experiment was to investigate the bandwidth of the

frequency loop. The intention of the laser pulse was to rapidly (much faster than the bandwidth) kick the resonator. Then the rise time of the feedback could be measured. This was found to be around 4.5 kHz and was limited by the integration of the PID controller. Importantly this was much higher than the sampling rate of 100 Hz which was used for all noise measurements. This ensured the feedback mechanism did not interfere with the analysis of the noise measurements.

### Coupling to a controlled two level system

The fractal sample from Chalmers which featured in section 9 also had a sister sample which contained Cooper pair boxes coupled to some of the resonators. A heavily attenuated gate line was installed into the fridge to gate the CPB via the ground plane. This allowed the occupation of the CPB island to be controlled, where the capacitive coupling to the resonator varies with the island occupation, resulting in a frequency shift.

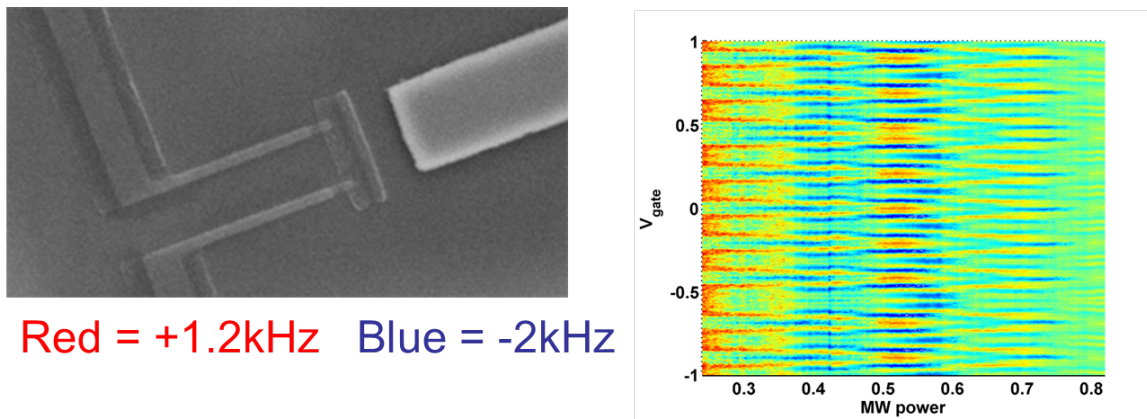


Figure 11.3: Left, an electron microscope image of the CPB. Right, a 2D plot of the measured resonator response to a coupled CPB under varying DC gate voltage and microwave drive

The frequency shift can be easily detected by use of an oscilloscope. More interestingly the system shows interesting behaviour when the microwave drive is increased. Figure 11.3 details this effect within the 2D plot, where the colour relates to the frequency offset. At high drive, the qubit energy level splitting is exceeded and the system reveals evidence for photon assisted quasiparticle tunnelling, which have been studied extensively using a Pound setup at Chalmers [136] [134]. Further study of this system was not possible

due to global helium shortages, and instead efforts were made to consolidate the noise measurements which form the bulk of the thesis. However, the suitability of the Pound based technique for both detector and QIP applications have been demonstrated.

## 11.4 Outlook

While many elements of the Pound setup and this project have been examined in considerable detail there are many elements which remain to be uncovered. The setup has proven both versatile and powerful, but this has been with only modest equipment. There is much room for improvement with the use of a state of the art synthesizer, amplifier chain and detector diode. 3 state of the art amplifiers can now realise the 100 dB of gain which is attained with 4 amplifiers in this work, however losing one amplifier would significantly reduce the systematic flicker noise floor. Figure 7.4 demonstrated the huge signal increase by using a state of the art detector diode. Such an improvement would allow for operation at lower powers, beneficial for QIP [134] or, allow for operation with less integration, and hence a faster feedback response, beneficial for scanning applications [137].

Further improvements are also possible within device fabrication. Improved measurements of the resonators response to optical radiation would be very interesting if the resonator was optimised as a kinetic inductance detector. In this regard, the setup is incredibly versatile as obtaining such a sample through collaboration would enable this measurement. Another aspect for further scope is the use of epitaxially grown Nb. These films have shown huge promise with comparatively little optimisation in the fabrication. Extensive studies of fabrication parameters for these, and other epitaxially grown films should lead to noticeable improvements in sample quality, as was found in TiN [138] [139].

Additionally the implementation of devices coupled to resonators should further expand the parameter space for noise measurements. At present only Josephson junction embedded resonators have been studied in some detail [110]. However, this was by no means an exhaustive study any many more parameters can be studied in this device. Furthermore more complicated devices such various types of qubit [134] would provide the capacity for the further study of much interesting physics. This can include a detailed probe of the relative noise contributions from the device or the resonator. Where the goal

of the measurement should be at first to determine the contributions of each. Then under various drive parameters, measurements could explore whether saddle point behaviour exists. Demonstrating the noise is minimised under particular drive conditions should be beneficial for many applications of these devices.

Perhaps more important is the new information of the nature of TLFs that has come from this thesis. Many properties of superconducting resonators were able to be described well enough by essentially the basic TLF theory originally derived in the 70s. This considered the bath of TLFs as non interacting, this is despite little justification that they should not interact. In recent years the results which could not be explained by the standard model have increased. This includes both the temperature dependence of the  $T_1$  &  $T_2$  in qubits and the weaker than expected power dependence of  $Q_i$  in high quality resonators. The noise measurements within this thesis agree strongly with the qubit measurements and are well described by a model of interacting TLFs described by Faoro et al. [69]. It is here that an improved understanding of the nature of TLFs should enable theory to guide future experiments.

To summarise, the Pound technique has enabled the study of much interesting physics, but, there remains a large potential for the technique to be improved. This should allow for many more interesting experiments and much more physics to be found.

# Appendix A: Fabrication

This section overviews the fabrication methods used for this work. Although in general Nb thin films were used, the recipes are equally applicable for Al, Ta and TiN films. It is assumed the wafer has already been diced into correctly sized chips. Note times may differ slightly depending on temperature and age of resist.

- Initial clean
  1. Room temperature acetone
  2. Room temperature isopropanol
  3. Rinse in de-ionized water
  4. Nitrogen blow dry
- Photoresist and development
  5. S1813 photoresist spin at 4000 rpm (produces 1.1  $\mu\text{m}$  resist height)
  6. Bake on hot plate at 100° C for 10 minutes
  7. Beading exposure, 2x 30 second exposure in UV
  8. Develop in MF-319 for 25 seconds
  9. Rinse in de-ionized water
  10. Nitrogen blow dry
  11. Pattern exposure, 12 second exposure in UV
  12. Develop in MF-319 for 10 seconds
  13. Rinse in de-ionized water
  14. Check in microscope and redevelop if needed
- RIE and resist removal
  15. Etch recipe *Resist strip* for 20 seconds
  16. Etch recipe *Nb etch* for 8 minutes (sufficient for 200 nm of Nb)
  17. Etch recipe *Resist strip* for 30 seconds
  18. Rinse in 1165 at 50° for 5 minutes

19. Rinse in room temperature isopropanol
20. Rinse in de-ionized water
21. Nitrogen blow dry

If any 1165 remains (which appears as a grease-like residue) repeat the isopropanol rinse. The use of heated 1165 is required to remove the resist strands which appear in figure 0.1. These resist strands appear throughout the sample after the main Nb etch. Their presence can be reduced by extending the final resist strip steps although caution is needed ensure resist remains atop the metal (this is to protect the metal from the excess oxidation from the oxygen plasma of the resist strip recipe). Both the resist strands and excess oxidation of the metal surface are detrimental to the sample quality, resulting in reduced quality factors and increased loss tangents. The right scan of figure 0.2 underwent all fabrication steps and results in the highest fabrication quality.

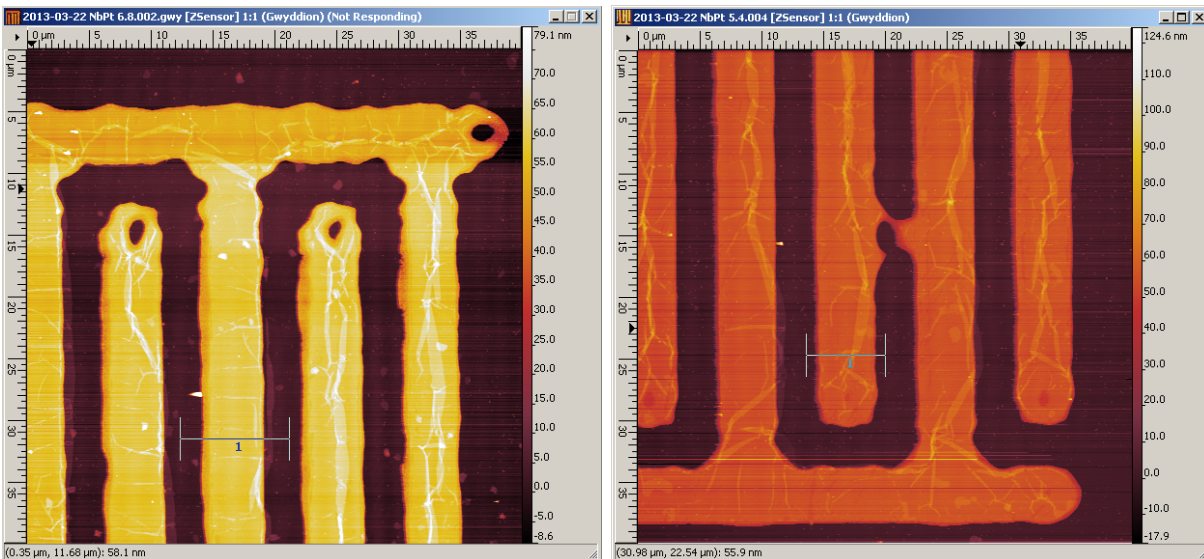


Figure 0.1: Comparison of samples fabricated with and without additional bead removal steps. Left, AFM scan of a sample fabricated without the bead removal process (steps 7 and 8). This leads to a poor contact between the mask and the resist due to resist stacking in the corners of the chip. The poor contact leads to excess reflection around the capacitive fingers producing over-exposure. The over-development manifests as the hole at the end of the capacitive finger. Right, AFM scan of a sample fabricated with the bead removal process (steps 7 and 8). The enhanced mask-resist contact allows for less reflection and hence no over-exposure.

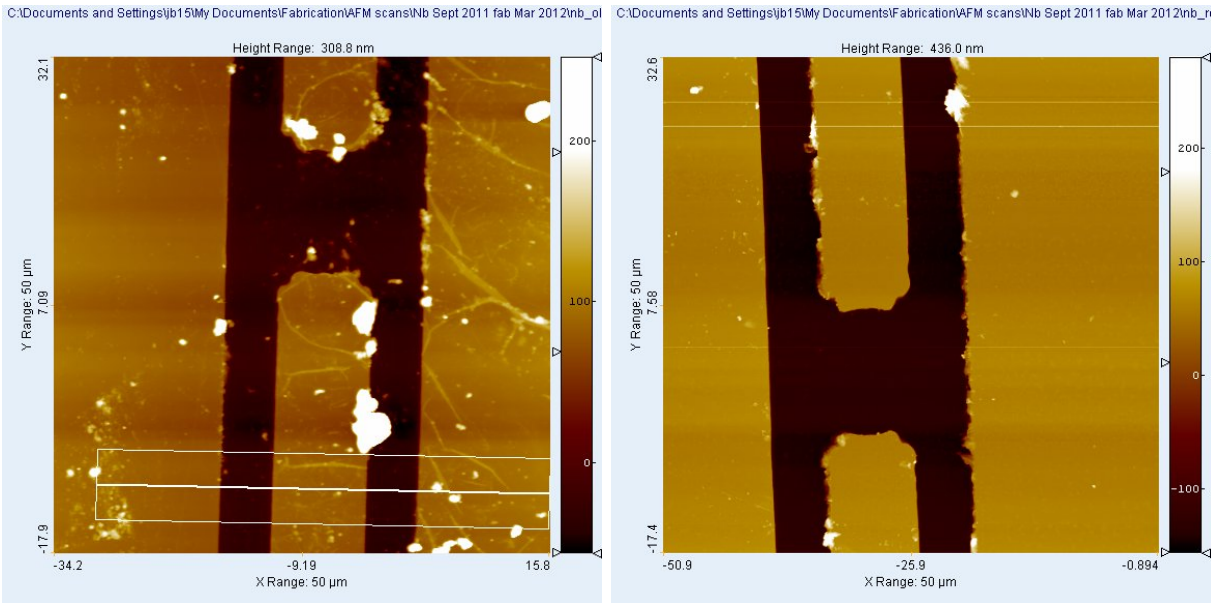


Figure 0.2: Comparison of samples fabricated with and without additional resist strip steps. This step removes resist stacks caused by defects in the mask or under-development. Without this step, samples exhibit more defects and build up of material at the edges. This is problematic as the edges contain a high current density and hence problems here contribute greater to the quality of the resonator. Left, AFM scan of a sample fabricated without the bead removal process (step 15). Right, AFM scan of a sample fabricated with the bead removal process (step 15).

# Appendix B: Research output

## Publications

- Burnett, J., Faoro, L., Wisby, I., Gurtovoi, V. L., Chernykh, A. V., Mikhailov, G. M., Tulin, V. A., Shaikhaidarov, R., Antonov, V., Meeson, P. J., Tzalenchuk, A. Ya. & Lindstrom, T. (2013). Evidence for interacting two-level systems from the  $1/f$  noise of a superconducting resonator. arXiv preprint arXiv:1311.1655.
- Burnett, J., Lindstrm, T., Oxborrow, M., Harada, Y., Sekine, Y., Meeson, P., & Tzalenchuk, A. Y. Slow noise processes in superconducting resonators. *Physical Review B*, 87(14), 140501. (2013)
- Lindstrom, T., Burnett, J., Oxborrow, M., & Tzalenchuk, A. Y. Pound-locking for characterization of superconducting microresonators. *Review of Scientific Instruments*, 82(10), 104706-104706. (2011)

## Conference Proceedings

- Burnett, J., Lindstrm, T., Wisby, I., de Graaf, S., Adamyan, A., Kubatkin, S., Meeson, P. & Tzalenchuk, A. Y. Identifying noise processes in superconducting resonators, *Superconductive Electronics Conference (ISEC)*, 2013 IEEE 14th International, pp. 1-3, 2003

## Talks

- Characterising superconducting resonators lumped element resonators by pound locking.  
4th Microresonator workshop, Grenoble, 2011

## Posters

- Identifying noise processes in superconducting resonators.  
ISEC-14, Cambridge, 2013
- Studies of dielectric loss and noise in superconducting resonators.  
CMD-24/CMMP12, Edinburgh, 2012
- High precision readout of superconducting resonators by Pound-locking.  
CMMP-11, Manchester, 2011
- Pound-Drever-Hall readout of superconducting lumped element resonators.  
International Workshop on Mesoscopic Superconductivity & Vortex Imaging, Bath, 2011

# Bibliography

- [1] Day, P. K., LeDuc, H. G., Mazin, B. A., Vayonakis, A. & Zmuidzinas, J. A broadband superconducting detector suitable for use in large arrays. *Nature* **425**, 817–821 (2003).
- [2] Wallraff, A. *et al.* Strong coupling of a single photon to a superconducting qubit using circuit quantum electrodynamics. *Nature* **431**, 162–167 (2004).
- [3] Boixo, S. *et al.* Evidence for quantum annealing with more than one hundred qubits. *Nature Physics* **10**, 218–224 (2014).
- [4] Mazin, B. *et al.* Arcons: A 2024 pixel optical through near-ir cryogenic imaging spectrophotometer. *arXiv preprint arXiv:1306.4674* (2013).
- [5] Caldeira, A. & Leggett, A. Influence of dissipation on quantum tunneling in macroscopic systems. *Physical Review Letters* **46**, 211 (1981).
- [6] Simmonds, R. *et al.* Decoherence in josephson phase qubits from junction resonators. *Physical review letters* **93**, 077003 (2004).
- [7] Zmuidzinas, J. Superconducting microresonators: Physics and applications. *Annu. Rev. Condens. Matter Phys.* **3**, 169–214 (2012).
- [8] Barends, R. *et al.* Reduced frequency noise in superconducting resonators. *Applied Physics Letters* **97**, 033507–033507 (2010).
- [9] Leduc, H. G. *et al.* Titanium nitride films for ultrasensitive microresonator detectors. *Applied Physics Letters* **97**, 102509–102509 (2010).
- [10] Sillanpää, M. A., Park, J. I. & Simmonds, R. W. Coherent quantum state storage and transfer between two phase qubits via a resonant cavity. *Nature* **449**, 438–442 (2007).
- [11] Castellanos-Beltran, M. & Lehnert, K. Widely tunable parametric amplifier based on a superconducting quantum interference device array resonator. *Applied Physics Letters* **91**, 083509–083509 (2007).
- [12] Tholén, E. A. *et al.* Nonlinearities and parametric amplification in superconducting coplanar waveguide resonators. *Applied physics letters* **90**, 253509–253509 (2007).

- [13] Wang, H. *et al.* Improving the coherence time of superconducting coplanar resonators. *Applied Physics Letters* **95**, 233508–233508 (2009).
- [14] O’Connell, A. D. *et al.* Microwave dielectric loss at single photon energies and millikelvin temperatures. *Applied Physics Letters* **92**, 112903–112903 (2008).
- [15] Mazin, B. *Microwave kinetic inductance detectors*. Ph.D. thesis, California Institute of Technology (2004).
- [16] Tancredi, G. *Superconducting Tunable Resonator*. Ph.D. thesis, Royal Holloway University of London (2009).
- [17] Barends, R. *Photon-detecting superconducting resonators*. Ph.D. thesis, Delft University of Technology, The Netherlands (2009).
- [18] Gao, J. *The physics of superconducting microwave resonators*. Ph.D. thesis, California Institute of Technology (2008).
- [19] Healey, J. *Experiments to develop high Q and tunable superconducting coplanar resonators*. Ph.D. thesis, Birmingham University (2010).
- [20] Von Schickfus, M. & Hunklinger, S. Saturation of the dielectric absorption of vitreous silica at low temperatures. *Physics Letters A* **64**, 144–146 (1977).
- [21] Strom, U., Von Schickfus, M. & Hunklinger, S. Low-temperature anomalies in the microwave dielectric properties of  $\alpha$ -beta-alumina. *Physical Review Letters* **41**, 910–913 (1978).
- [22] Phillips, W. Tunneling states in amorphous solids. *Journal of Low Temperature Physics* **7**, 351–360 (1972).
- [23] Phillips, W. Two-level states in glasses. *Reports on Progress in Physics* **50**, 1657 (1987).
- [24] Kogan, S. *Electronic noise and fluctuations in solids* (Cambridge University Press, 2008).
- [25] Shnirman, A., Schön, G., Martin, I. & Makhlin, Y. Low-and high-frequency noise from coherent two-level systems. *Physical review letters* **94**, 127002 (2005).
- [26] Schrieffer, J., Makhlin, Y., Shnirman, A. & Schön, G. Decoherence from ensembles of two-level fluctuators. *New Journal of Physics* **8**, 1 (2006).
- [27] Patel, U. *et al.* Coherent josephson phase qubit with a single crystal silicon capacitor. *Applied Physics Letters* **102**, 012602–012602 (2013).

- [28] Steffen, M. *et al.* State tomography of capacitively shunted phase qubits with high fidelity. *Physical review letters* **97**, 050502 (2006).
- [29] Drever, R. W. P., Hall, J. L., Kowalski, F. V., Hough, J. & Ford, G. M. Laser phase and frequency stabilization using an optical resonator. *APPLIED PHYSICS B* **31**, 97–105 (1983).
- [30] Hook, J. & Hall, H. *Solid state physics*. The Manchester physics series (Wiley, 1991).
- [31] Bardeen, J., Cooper, L. N. & Schrieffer, J. R. Theory of superconductivity. *Physical Review* **108**, 1175 (1957).
- [32] Bogoliubov, N. On the theory of superfluidity. *J. phys.(UssR)* **11**, 4–2 (1947).
- [33] Anderson, P. W., Halperin, B. & Varma, C. M. Anomalous low-temperature thermal properties of glasses and spin glasses. *Philosophical Magazine* **25**, 1–9 (1972).
- [34] Enss, C. & Hunklinger, S. *Low-Temperature Physics*. SpringerLink: Springer e-Books (Springer, 2005).
- [35] Miranda, F. A., Gordon, W. L., Heinen, V. O., Ebihara, B. T. & Bhasin, K. B. Measurements of complex permittivity of microwave substrates in the 20 to 300 k temperature range from 26. 5 to 40. 0 ghz. Tech. Rep., National Aeronautics and Space Administration, Cleveland, OH (USA). Lewis Research Center (1989).
- [36] Krupka, J. *et al.* Measurements of permittivity, dielectric loss tangent, and resistivity of float-zone silicon at microwave frequencies. *Microwave Theory and Techniques, IEEE Transactions on* **54**, 3995–4001 (2006).
- [37] Lindström, T., Healey, J., Colclough, M., Muirhead, C. & Tzalenchuk, A. Y. Properties of superconducting planar resonators at millikelvin temperatures. *Physical Review B* **80**, 132501 (2009).
- [38] Khalil, M. S., Wellstood, F. & Osborn, K. D. Loss dependence on geometry and applied power in superconducting coplanar resonators. *Applied Superconductivity, IEEE Transactions on* **21**, 879–882 (2011).
- [39] Vissers, M. R. *et al.* Low loss superconducting titanium nitride coplanar waveguide resonators. *Applied Physics Letters* **97**, 232509–232509 (2010).
- [40] Pappas, D. P., Vissers, M. R., Wisbey, D. S., Kline, J. S. & Gao, J. Two level system loss in superconducting microwave resonators. *Applied Superconductivity, IEEE Transactions on* **21**, 871–874 (2011).

- [41] Sage, J. M., Bolkhovskiy, V., Oliver, W. D., Turek, B. & Welander, P. B. Study of loss in superconducting coplanar waveguide resonators. *Journal of Applied Physics* **109**, 063915–063915 (2011).
- [42] Barends, R. *et al.* Niobium and tantalum high q resonators for photon detectors. *Applied Superconductivity, IEEE Transactions on* **17**, 263–266 (2007).
- [43] Barends, R. *et al.* Contribution of dielectrics to frequency and noise of nbtin superconducting resonators. *Applied Physics Letters* **92**, 223502–223502 (2008).
- [44] Burnett, J. *et al.* Slow noise processes in superconducting resonators. *Physical Review B* **87**, 140501 (2013).
- [45] Gao, J. *et al.* Experimental evidence for a surface distribution of two-level systems in superconducting lithographed microwave resonators. *Applied Physics Letters* **92**, 152505–152505 (2008).
- [46] Mattis, D. & Bardeen, J. Theory of the anomalous skin effect in normal and superconducting metals. *Physical Review* **111**, 412 (1958).
- [47] Pozar, D. *Microwave Engineering* (Wiley, 2004).
- [48] Lancaster, J. *Passive Microwave Device Applications of High-Temperature Superconductors* (Cambridge University Press, 2006).
- [49] Doyle, S. *Lumped Element Kinetic Inductance Detectors*. Ph.D. thesis, Cardiff University, Cardiff, Wales (2008).
- [50] Calvo, M. *Development of Kinetic Inductance Detectors for the study of the Cosmic Microwave Background Polarization*. Ph.D. thesis, Sapienza University of Rome (2008).
- [51] Gao, J., Zmuidzinas, J., Mazin, B. A., LeDuc, H. G. & Day, P. K. Noise properties of superconducting coplanar waveguide microwave resonators. *Applied Physics Letters* **90**, 102507–102507 (2007).
- [52] Pound, R. V. Electronic frequency stabilization of microwave oscillators. *Review of Scientific Instruments* **17**, 490–505 (1946).
- [53] Bloembergen, N. Robert vivian pound 1919–2010. Tech. Rep., National Academy of Sciences (2013).
- [54] Pound, R. & Rebka Jr, G. Gravitational red-shift in nuclear resonance. *Phys. Rev. Letters* **3**, 1 (1959).

- [55] Black, E. D. An introduction to pound–drever–hall laser frequency stabilization. *American Journal of Physics* **69**, 79 (2001).
- [56] Hornibrook, J., Mitchell, E., Lewis, C. & Reilly, D. Parasitic losses in nb superconducting resonators. *Physics Procedia* **36**, 187–192 (2012).
- [57] Khalil, M., Stoutimore, M., Wellstood, F. & Osborn, K. An analysis method for asymmetric resonator transmission applied to superconducting devices. *Journal of Applied Physics* **111**, 054510–054510 (2012).
- [58] Rubiola, E. *Phase Noise and Frequency Stability in Oscillators*. The Cambridge RF and Microwave Engineering Series (Cambridge University Press, 2010).
- [59] Allan, D. W. Statistics of atomic frequency standards. *Proceedings of the IEEE* **54**, 221–230 (1966).
- [60] Howe, D. A., Allan, D. & Barnes, J. Properties of signal sources and measurement methods. In *Thirty Fifth Annual Frequency Control Symposium. 1981*, 669–716 (IEEE, 1981).
- [61] Riley, W. J. *Handbook of frequency stability analysis* (US Department of Commerce, National Institute of Standards and Technology, 2008).
- [62] NIST. frequency metrology pages <http://tf.nist.gov/phase/properties/four.htm>. Tech. Rep. (2013).
- [63] De Visser, P. *et al.* Number fluctuations of sparse quasiparticles in a superconductor. *Physical Review Letters* **106**, 167004 (2011).
- [64] De Visser, P. *et al.* Generation-recombination noise: the fundamental sensitivity limit for kinetic inductance detectors. *Journal of Low Temperature Physics* **167**, 335–340 (2012).
- [65] Gao, J. R., Zmuidzinas, J., Mazin, B. a., LeDuc, H. G. & Day, P. K. Noise properties of superconducting coplanar waveguide microwave resonators. *Applied Physics Letters* **90**, 102507 (2007).
- [66] Ariyoshi, S. *et al.* Nbn-based microwave kinetic inductance detector with a rewind spiral resonator for broadband terahertz detection. *Applied Physics Express* **6**, 064103 (2013).
- [67] Baselmans, J. *et al.* Development of high-q superconducting resonators for use as kinetic inductance detectors. *Advances in Space Research* **40**, 708–713 (2007).

- [68] Sandberg, M. *et al.* Etch induced microwave losses in titanium nitride superconducting resonators. *Applied Physics Letters* **100**, 262605–262605 (2012).
- [69] Faoro, L. & Ioffe, L. B. Internal loss of superconducting resonators induced by interacting two-level systems. *Physical review letters* **109**, 157005 (2012).
- [70] Macha, P. Losses in coplanar waveguide resonators at millikelvin temperatures. *Applied Physics Letters* **96**, 062503 (2010).
- [71] Barends, R. *et al.* Minimal resonator loss for circuit quantum electrodynamics. *Applied Physics Letters* **97**, 023508–023508 (2010).
- [72] Wenner, J. *et al.* Surface loss simulations of superconducting coplanar waveguide resonators. *Applied Physics Letters* **99**, 113513–113513 (2011).
- [73] Palacios-Laloy, A. *et al.* Tunable resonators for quantum circuits. *Journal of Low Temperature Physics* **151**, 1034–1042 (2008).
- [74] Kubo, Y. *et al.* Strong coupling of a spin ensemble to a superconducting resonator. *Phys. Rev. Lett* **105**, 140502 (2010).
- [75] Song, C., DeFeo, M., Yu, K. & Plourde, B. Reducing microwave loss in superconducting resonators due to trapped vortices. *Applied Physics Letters* **95**, 232501–232501 (2009).
- [76] Bothner, D., Gaber, T., Kemmler, M., Koelle, D. & Kleiner, R. Improving the performance of superconducting microwave resonators in magnetic fields. *Applied Physics Letters* **98**, 102504–102504 (2011).
- [77] Bothner, D. *et al.* Reducing vortex losses in superconducting microwave resonators with microsphere patterned antidot arrays. *Applied Physics Letters* **100**, 012601–012601 (2012).
- [78] Bothner, D. *et al.* Magnetic hysteresis effects in superconducting coplanar microwave resonators. *Physical Review B* **86**, 014517 (2012).
- [79] Graaf, S. d., Danilov, A., Adamyan, A., Bauch, T. & Kubatkin, S. Magnetic field resilient superconducting fractal resonators for coupling to free spins. *Journal of Applied Physics* **112**, 123905–123905 (2012).
- [80] Sandberg, M. *et al.* Tuning the field in a microwave resonator faster than the photon lifetime. *Applied Physics Letters* **92**, 203501–203501 (2008).
- [81] Kubo, Y. *et al.* Storage and retrieval of a microwave field in a spin ensemble. *Physical Review A* **85**, 012333 (2012).

- [82] Wilson, C. *et al.* Observation of the dynamical casimir effect in a superconducting circuit. *Nature* **479**, 376–379 (2011).
- [83] Koch, R. H. *et al.* Flicker (1/f) noise in tunnel junction dc squids. *Journal of low temperature physics* **51**, 207–224 (1983).
- [84] Foglietti, V. *et al.* Low-frequency noise in low 1/f noise dc squid’s. *Applied physics letters* **49**, 1393–1395 (1986).
- [85] Wellstood, F., Urbina, C. & Clarke, J. Excess noise in dc squids from 4.2 k to 0.022 k. *Magnetics, IEEE Transactions on* **23**, 1662–1665 (1987).
- [86] Wellstood, F. C., Urbina, C. & Clarke, J. Low-frequency noise in dc superconducting quantum interference devices below 1 k. *Applied physics letters* **50**, 772–774 (1987).
- [87] Drung, D., Beyer, J., Storm, J., Peters, M. & Schurig, T. Investigation of low-frequency excess flux noise in dc squids at mk temperatures. *Applied Superconductivity, IEEE Transactions on* **21**, 340–344 (2011).
- [88] Zorin, A. *et al.* Background charge noise in metallic single-electron tunneling devices. *Physical Review B* **53**, 13682 (1996).
- [89] Astafiev, O., Pashkin, Y. A., Nakamura, Y., Yamamoto, T. & Tsai, J. Quantum noise in the josephson charge qubit. *Physical Review Letters* **93**, 267007 (2004).
- [90] Ithier, G. *et al.* Decoherence in a superconducting quantum bit circuit. *Physical Review B* **72**, 134519 (2005).
- [91] Schreier, J. *et al.* Suppressing charge noise decoherence in superconducting charge qubits. *Physical Review B* **77**, 180502 (2008).
- [92] Dutta, P. & Horn, P. Low-frequency fluctuations in solids: 1/f noise. *Reviews of Modern physics* **53** (1981).
- [93] Weissman, M. *et al.* 1/ f noise and other slow, nonexponential kinetics in condensed matter. *Reviews of modern physics* **60**, 537–571 (1988).
- [94] Kirton, M. & Uren, M. Noise in solid-state microstructures: A new perspective on individual defects, interface states and low-frequency (1/f) noise. *Advances in Physics* **38**, 367–468 (1989).
- [95] Hooge, F. 1/f noise sources. *Electron Devices, IEEE Transactions on* **41**, 1926–1935 (1994).

- [96] Kenyon, M., Lobb, C. & Wellstood, F. Temperature dependence of low-frequency noise in al-al<sub>2</sub>o<sub>3</sub>-al single-electron transistors. *Journal of Applied Physics* **88**, 6536–6540 (2000).
- [97] Wellstood, F., Urbina, C. & Clarke, J. Flicker (1/f) noise in the critical current of josephson junctions at 0.09–4.2. *Applied physics letters* **85**, 5296–5298 (2004).
- [98] Astafiev, O., Pashkin, Y. A., Nakamura, Y., Yamamoto, T. & Tsai, J. Temperature square dependence of the low frequency 1/f charge noise in the josephson junction qubits. *Physical review letters* **96**, 137001 (2006).
- [99] Li, T. *et al.* Low-frequency charge noise in suspended aluminum single-electron transistors. *Applied Physics Letters* **91**, 033107–033107 (2007).
- [100] Yan, F. *et al.* Spectroscopy of low-frequency noise and its temperature dependence in a superconducting qubit. *Physical Review B* **85**, 174521 (2012).
- [101] Gustafsson, M. V., Pourkabirian, A., Johansson, G., Clarke, J. & Delsing, P. Thermal properties of charge noise sources. *Physical Review B* **88**, 245410 (2013).
- [102] Bialczak, R. C. *et al.* 1/f flux noise in josephson phase qubits. *Physical review letters* **99**, 187006 (2007).
- [103] Anton, S. *et al.* Magnetic flux noise in dc squids: Temperature and geometry dependence. *Physical Review Letters* **110**, 147002 (2013).
- [104] Rozhko, S. *et al.* Study of low frequency noise performance of nanobridge-based squids in external magnetic fields (2013).
- [105] Nugroho, C., Orlyanchik, V. & Van Harlingen, D. Low frequency resistance and critical current fluctuations in al-based josephson junctions. *Applied Physics Letters* **102**, 142602–142602 (2013).
- [106] Kumar, S. *et al.* Temperature dependence of the frequency and noise of superconducting coplanar waveguide resonators. *Applied Physics Letters* **92**, 123503–123503 (2008).
- [107] Gao, J. *et al.* A semiempirical model for two-level system noise in superconducting microresonators. *Applied Physics Letters* **92**, – (2008).
- [108] Barends, R. *et al.* Quasiparticle relaxation in optically excited high-q superconducting resonators. *Physical review letters* **100**, 257002 (2008).

- [109] Barends, R. *et al.* Noise in nbtin, al, and ta superconducting resonators on silicon and sapphire substrates. *Applied Superconductivity, IEEE Transactions on* **19**, 936–939 (2009).
- [110] Murch, K., Weber, S., Levenson-Falk, E., Vijay, R. & Siddiqi, I. 1/f noise of josephson-junction-embedded microwave resonators at single photon energies and millikelvin temperatures. *Applied Physics Letters* **100**, 142601–142601 (2012).
- [111] SRS. Stanford research systems prs10 - rubidium frequency standard with low phase noise: data sheet, found at <http://www.thinksrs.com/products/prs10.htm>, accessed june 2013. Tech. Rep. (2013).
- [112] Szymaniec, K., Park, S. E., Marra, G. & Chałupczak, W. First accuracy evaluation of the npl-csf2 primary frequency standard. *Metrologia* **47**, 363 (2010).
- [113] Marra, G., Henderson, D. & Oxborrow, M. Frequency stability and phase noise of a pair of x-band cryogenic sapphire oscillators. *Measurement Science and Technology* **18**, 1224 (2007).
- [114] Pospieszalski, M. W. Extremely low-noise amplification with cryogenic fets and hfets: 1970-2004. *Microwave Magazine, IEEE* **6**, 62–75 (2005).
- [115] Smith, A., Sandell, R., Burch, J. & Silver, A. Low noise microwave parametric amplifier. *Magnetics, IEEE Transactions on* **21**, 1022–1028 (1985).
- [116] Castellanos-Beltran, M., Irwin, K., Hilton, G., Vale, L. & Lehnert, K. Amplification and squeezing of quantum noise with a tunable josephson metamaterial. *Nature Physics* **4**, 929–931 (2008).
- [117] Vijay, R., Devoret, M. & Siddiqi, I. Invited review article: The josephson bifurcation amplifier. *Review of Scientific Instruments* **80**, 111101–111101 (2009).
- [118] Eom, B. H., Day, P. K., LeDuc, H. G. & Zmuidzinas, J. A wideband, low-noise superconducting amplifier with high dynamic range. *Nature Physics* (2012).
- [119] Oxborrow, M., Breeze, J. D. & Alford, N. M. Room-temperature solid-state maser. *Nature* **488**, 353–356 (2012).
- [120] Low noise factory, 4-8 ghz cryogenic amplifier product page, <http://www.lownoisefactory.com/products/exband1/lnc-4-8-ghz/>. Tech. Rep. (2013).
- [121] White, G. & Meeson, P. *Experimental Techniques in Low-Temperature Physics: Fourth Edition*. Monographs on the Physics and Chemistry of Materials (OUP Oxford, 2002).

- [122] Lindstrom, T., Burnett, J., Oxborrow, M. & Tzalenchuk, A. Y. Pound-locking for characterization of superconducting microresonators. *Review of Scientific Instruments* **82**, 104706–104706 (2011).
- [123] Creedon, D. L., Tobar, M. E., Ivanov, E. N. & Hartnett, J. G. High-resolution flicker-noise-free frequency measurements of weak microwave signals. *Microwave Theory and Techniques, IEEE Transactions on* **59**, 1651–1657 (2011).
- [124] Burnett, J. *et al.* Pc2: Identifying noise processes in superconducting resonators. In *Superconductive Electronics Conference (ISEC), 2013 IEEE 14th International*, 1–3 (2013).
- [125] de Graaf, S. E. *Fractal superconducting resonators for the interrogation of two-level systems*. Ph.D. thesis, Chalmers University of Technology (2014).
- [126] de Graaf, S., Davidovikj, D., Adamyan, A., Kubatkin, S. & Danilov, A. Galvanically split superconducting microwave resonators for introducing internal voltage bias. *Applied Physics Letters* **104**, 052601 (2014).
- [127] Burnett, J. *et al.* Evidence for interacting two-level systems from the 1/f noise of a superconducting resonator. *arXiv preprint arXiv:1311.1655* (2013).
- [128] Mikhailov, G., Malikov, I., Chernykh, A. & Petrashov, V. The effect of growth temperature on electrical conductivity and on the structure of thin refractory metal films, grown by laser ablation deposition. *Thin solid films* **293**, 315–319 (1997).
- [129] Sendelbach, S. *et al.* Magnetism in squids at millikelvin temperatures. *Physical review letters* **100**, 227006 (2008).
- [130] Sendelbach, S., Hover, D., Mück, M. & McDermott, R. Complex inductance, excess noise, and surface magnetism in dc squids. *Physical review letters* **103**, 117001 (2009).
- [131] Faoro, L. & Ioffe, L. B. Microscopic origin of low-frequency flux noise in josephson circuits. *Physical review letters* **100**, 227005 (2008).
- [132] Lanting, T. *et al.* Evidence for temperature-dependent spin diffusion as a mechanism of intrinsic flux noise in squids. *Physical Review B* **89**, 014503 (2014).
- [133] Lisenfeld, J. *et al.* Measuring the temperature dependence of individual two-level systems by direct coherent control. *Physical review letters* **105**, 230504 (2010).
- [134] de Graaf, S. E. *et al.* Charge qubit coupled to an intense microwave electromagnetic field in a superconducting nb device: Evidence for photon-assisted quasiparticle tunneling. *Physical review letters* **111**, 137002 (2013).

- [135] Gao, J. *et al.* A titanium-nitride near-infrared kinetic inductance photon-counting detector and its anomalous electrodynamics. *Applied Physics Letters* **101**, 142602–142602 (2012).
- [136] Leppäkangas, J. *et al.* Effects of quasiparticle tunnelling in a circuit-qed realization of a strongly driven two-level system. *Journal of Physics B: Atomic, Molecular and Optical Physics* **46**, 224019 (2013).
- [137] de Graaf, S. E., Danilov, A., Adamyan, A. & Kubatkin, S. A near-field scanning microwave microscope based on a superconducting resonator for low power measurements. *Review of Scientific Instruments* **84**, 023706–023706 (2013).
- [138] Vissers, M. *et al.* Reduction of microwave loss in titanium nitride cpw resonators. *Bulletin of the American Physical Society* **57** (2012).
- [139] Ohya, S. *et al.* Room temperature deposition of sputtered tin films for superconducting coplanar waveguide resonators. *Superconductor Science and Technology* **27**, 015009 (2014).